Numerical-experimental analysis of thermal shock damage in refractory materials

Citation for published version (APA):
Damhof, F. (2010). *Numerical-experimental analysis of thermal shock damage in refractory materials*. [Phd Thesis 4 Research NOT TU/e / Graduation NOT TU/e), Mechanical Engineering]. Corus Technology. https://doi.org/10.6100/IR675493

DOI:
10.6100/IR675493

Document status and date:
Published: 01/01/2010

Document Version:
Publisher's PDF, also known as Version of Record (includes final page, issue and volume numbers)

Please check the document version of this publication:

• A submitted manuscript is the version of the article upon submission and before peer-review. There can be important differences between the submitted version and the official published version of record. People interested in the research are advised to contact the author for the final version of the publication, or visit the DOI to the publisher's website.
• The final author version and the galley proof are versions of the publication after peer review.
• The final published version features the final layout of the paper including the volume, issue and page numbers.

Link to publication

General rights
Copyright and moral rights for the publications made accessible in the public portal are retained by the authors and/or other copyright owners and it is a condition of accessing publications that users recognise and abide by the legal requirements associated with these rights.

- Users may download and print one copy of any publication from the public portal for the purpose of private study or research.
- You may not further distribute the material or use it for any profit-making activity or commercial gain
- You may freely distribute the URL identifying the publication in the public portal.

If the publication is distributed under the terms of Article 25fa of the Dutch Copyright Act, indicated by the "Taverne" license above, please follow below link for the End User Agreement:

www.tue.nl/taverne

Take down policy
If you believe that this document breaches copyright please contact us at:

openaccess@tue.nl

providing details and we will investigate your claim.

Download date: 04. Oct. 2023

Numerical-experimental analysis of thermal shock damage in refractory materials

Frederik Damhof

corus

Cover design	Paul Verspaget
Front page	False color image of micro-cracks in corund refractory material, induced by water quenching and produced by optical microscopy and manual fracture tracing, made by Enno Zinngrebe, Corus Ceramics Research Centre
Back page	Thermal shock damage in inlet of steel degassing stallation
Copyright	Corus Technology B.V.
ISBN	978-90-805661-7-0

A catalogue record is available from the Eindhoven University of Technology Library.

Printed by the Universiteitsdrukkerij TU Eindhoven, Eindhoven, The Netherlands.

All rights reserved. No part of the material protected by this copyright may be reproduced in any form or by any means without written permission from the author.

Numerical-experimental analysis of thermal shock damage in refractory materials

PROEFSCHRIFT

ter verkrijging van de graad van doctor aan de
Technische Universiteit Eindhoven, op gezag van de
rector magnificus, prof.dr.ir. C.J. van Duijn, voor een
commissie aangewezen door het College voor
Promoties in het openbaar te verdedigen
op donderdag 3 juni 2010 om 16.00 uur

door

Frederik Damhof

geboren te Delfzijl

Dit proefschrift is goedgekeurd door de promotor:

prof.dr.ir. M.G.D. Geers

Copromotor:
dr.ir. W.A.M. Brekelmans

Contents Page

Summary ix

1. Introduction 1
1.1 Background 1
1.2 Objectives 6
1.3 Outline of the thesis 7
1.4 References 8

2. Non-local modelling of thermal shock damage in refractory materials 11
2.1 Introduction 11
2.2 Temperature-dependent mechanical behaviour 14
2.3 Constitutive model 15
2.3.1 Damage evolution 15
2.3.2 Equivalent strain 18
2.4 Finite element implementation 20
2.4.1 Weak forms and discretization of the governing equations 21
2.4.2 Linearization and incremental-iterative solution procedure 22
2.4.3 Computational solution issues 23
2.5 Non-local aspects of thermal shock damage 23
2.6 Thermal shock experiments 27
2.6.1 Set-up and experimental procedures 28
2.6.2 Results of the experiments and modelling 29
2.7 Conclusions 33
2.8 References 35
2.9 Linear system of equations 39

3. Experimental analysis of the evolution of thermal shock damage using transit time measurement of ultrasonic waves 43
3.1 Introduction 43
3.2 Materials 45
3.3 Damage characterization 47
3.4 Uniform damage experiments 49
3.4.1 Experimental set-up and procedures 49
3.4.2 Results 50
3.5 Thermal shock experiments with hot air followed by water quenching 51
3.5.1 Experimental set-up and procedures 51

3.5.2 Results 52
3.6 Thermal shock experiments with molten aluminium 54
3.6.1 Experimental set-up and procedures 55
3.6.2 Results with chamotte material 58
3.6.3 Results with corund material 59
3.7 Discussion 65
3.8 Conclusions 67
3.9 References 68

4. Non-local modelling of cyclic thermal shock damage including parameter estimation 75
4.1 Introduction 75
4.2 Damage experiments 77
4.2.1 Thermal damage 78
4.2.2 Thermal shock damage 79
4.3 Material model and solution procedure 80
4.3.1 Constitutive model 80
4.3.2 Parameter identification procedure 82
4.3.3 Geometry, boundary conditions and discretization 85
4.3.4 Calculation of transit time 86
4.4 Mixed numerical-experimental analysis 87
4.4.1 Model parameters, identification and validation 87
4.4.2 Parameter identifiability analyses 93
4.4.3 Damage evolution 97
4.5 Discussion 101
4.6 Conclusions 102
4.7 References 103

5. Predictive analysis of thermal shock damage in steelmaking installations 107
5.1 Introduction 107
5.2 Computational aspects 109
5.2.1 Constitutive damage model 109
5.2.2 Operator split strategy 111
5.3 Snorkel of a steel degassing installation 112
5.3.1 Introduction 112
5.3.2 Geometry, boundary conditions and discretization 113
5.3.3 Analysis results 119
5.4 Slag ring of a steel ladle 123
5.4.1 Introduction 123
5.4.2 Geometry, boundary conditions and discretization 125
5.4.3 Analysis results 129
5.5 Conclusions 134
5.6 References 135

5.7 Material properties of RHOB snorkel 138
5.8 Material properties of slag ring lining 140

6. Conclusions 141

Samenvatting 147

Acknowledgements 151

Curriculum vitae 153

Numerical-experimental analysis of thermal shock damage in refractory materials

Summary

Coarse grain refractory materials are used in installations for iron and steel-making operating at temperatures as high as 1800°C. A major cause leading to early failure of such installations is the wear of the refractory material due to fatal thermal stresses. These are caused for example by the pouring of liquid steel into a relatively cold ladle or the sudden opening of an operating furnace where the hot refractory material becomes exposed to cold air. Thermo-mechanical damage in the refractory lining reduces the lifetime and the availability of high-temperature installations, negatively affecting the cost-efficient production of steel. This calls for a predictive approach to thermal shock damage beforehand, in the design phase of installations as well as in post failure analyses.

Thermal shock damage in coarse grain refractory materials becomes initially manifest as clouds of diffuse micro-cracks and ultimately as macro-cracks depending on the number and severity of the thermal load cycles. The degradation is modelled accordingly using a continuum damage approach enriched with terms to account for fine scale damage and validated with data from representative thermal shock experiments. Location dependent acoustic measurements were used to characterize the damage. Unknown model parameters were identified in an inverse analysis involving an adaptation of the numerical model to enable the experimental-numerical comparison. An operator split strategy has been adopted to model thermal shock damage in complex high temperature installations subject to cyclic process conditions.

In order to model the transient thermo-mechanical damage and in particular thermal shock effects in coarse grain refractory materials a non-local damage framework was coupled with heat transport and mechanical balance equations. Non-uniform elasticity-based and uniform thermal damage were combined into a single variable for the total damage. The temperature-dependent elasticity-based damage is due to thermal expansion induced by temperature gradients and constrained internally within the material itself and externally by for example neighbouring bricks. Thermal damage is caused by temperature increases and is due to CTE mismatches at the micro-scale. The elasticity-based damage is controlled by a non-local equivalent strain. The governing non-locality equation is extended with terms to account for fine scale damage induced by thermal transients in addition to the contribution from long range elastic strain fields. The influence of non-locality including its (micro-structural strain gradient) extension was investigated in a parameter study. The phenomenological relevance of the damage framework was established by modelling thermal shock experiments in which chamotte refractory samples were brought into surface contact with molten aluminium followed by a down quench in ambient air.

In a literature review various set-ups were discussed to investigate thermal shock experimentally. The test method proposed in this thesis comprises the introduction of thermal shock in coarse grain refractory materials with reproducible and realistic heat transfer conditions representative for steel-making process conditions. Measurement of the transit time of ultrasonic longitudinal waves at various sample locations after a series of thermal shock experiments on corund samples revealed an impression of the distribution of the damage throughout the sample volume. The compatibility of acoustic and mechanical damage was confirmed in independent thermal shock experiments performed to mechanically validate the damage characterization method. Acoustic damage is defined here as the decrease of the dynamic Young's modulus with respect to that in the undamaged state. Mechanical damage is defined analogically as the decrease of Young's modulus obtained from mechanical tests, compared to that in the undamaged state. In a comparison of the damage measured after consecutive thermal shock experiments and quasi-stationary thermal experiments the interaction of elasticity-based and thermal damage could be observed. Moreover it appeared that progressing micro-cracks induced by thermal damage are obstructed by the prior elasticity-based damage.

To adequately model the damage evolution in refractory material subject to multiple consecutive thermal shock cycles, a rate dependent constitutive damage framework was proposed. Elasticity-based damage and thermal damage were combined in a multiplicative way to describe their experimentally observed interaction, including terms to describe the shielding of thermal damage by elasticity-based damage. The damage framework was implemented in a non-local thermo-mechanical finite element programme. Using the integrated form, the parameters of the evolution law for unshielded thermal damage could be identified from the results of the quasi-stationary thermal experiments. The other damage material parameters could be identified by the inverse modelling of the thermal shock cycling experiments using a Gauss-Newton minimization algorithm enriched with numerical damping and optimized through a parameter identifiability analysis. To enable the numerical-experimental comparison longitudinal wave propagation properties through damaged material were calculated using the numerical results exploiting the analogy between acoustic and mechanical damage. All model parameters could be determined with a reasonable accuracy. Particularly the non-local length scale was triggered by the information contained in the data set extracted from the transient experiments. A satisfactory experimental-numerical agreement of the results for the first and second thermal shock cycle was obtained. Modelling of the third thermal shock cycle to validate the optimized parameters revealed some deviations from the experiments at a more remote distance from the shock front. Here the transit times approach the undamaged experimental values and it appears that the model may not be accurate enough to capture these differences. Using parameter identifiability analyses the experimental set-up could be improved by enhancing the currently used acoustic measurement grid to the level where the inverse problem becomes well-posed. Modelling results obtained with the quantified parameters revealed furthermore that the elastic wave progresses nearly instantaneously into the sample. Temperature gradients affect the elasticity-based damage distribution only further away from the shock front. It appeared that thermal shock is a two-scale event where macroscopic and microscopic contributions are of the same order. Thermal damage contributes significantly to the total damage in spite of the shielding by elasticity-based damage.

The use of the developed and quantified damage framework in engineering applications was enabled by using a so-called operator split strategy. Non-local damage evolution is coupled incrementally with a thermo-mechanical finite element (FE) package used to analyze high temperature installations subject to cyclic process conditions. The non-locality is solved incrementally using a spatial FE discretization and a backward-Euler time integration scheme. The numerical solution strategy is demonstrated by studying thermal shock damage in the inlet of a steel degassing installation. The effect of a modification in the process conditions has been investigated. A second numerical example comprises the analysis of thermal shock damage in the refractory lining of a steel ladle.

1. Introduction

1.1 Background

Refractory materials are applied in the interiors of high temperature installations for example in baking furnaces for the production of ceramic table ware and in waste incinerators. Typical examples at the steelmaking facilities of Tata Steel are the blast furnace used for the production of raw iron operating at temperatures as high as 1800 °C, as well as the torpedo car, depicted in Fig. 1.1, used for the transport of the raw iron from the blast furnace to the steel plant. Yet another example is the interior of a blast oxygen furnace depicted in Fig. 1.2, used for the conversion of raw iron into various high quality steel grades. Refractory materials are not only subject to harsh thermal environments but also to the chemical interaction with the contained atmosphere such as steel slag in a ladle and molten aluminium in an electrolysis cell. A special class of refractories is formed by the technical ceramics. These finely grained high strength materials are commonly used as kiln furniture or high temperature tooling. The scope of this thesis, however, covers coarse grain refractory materials applied in steelmaking installations.

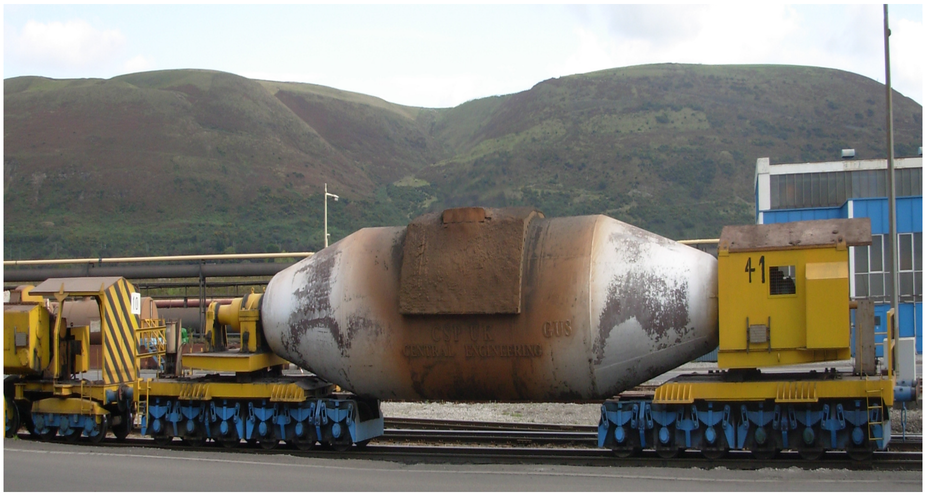

Fig. 1.1. Torpedo car used for the transport of raw iron from the blast furnace to the steel plant

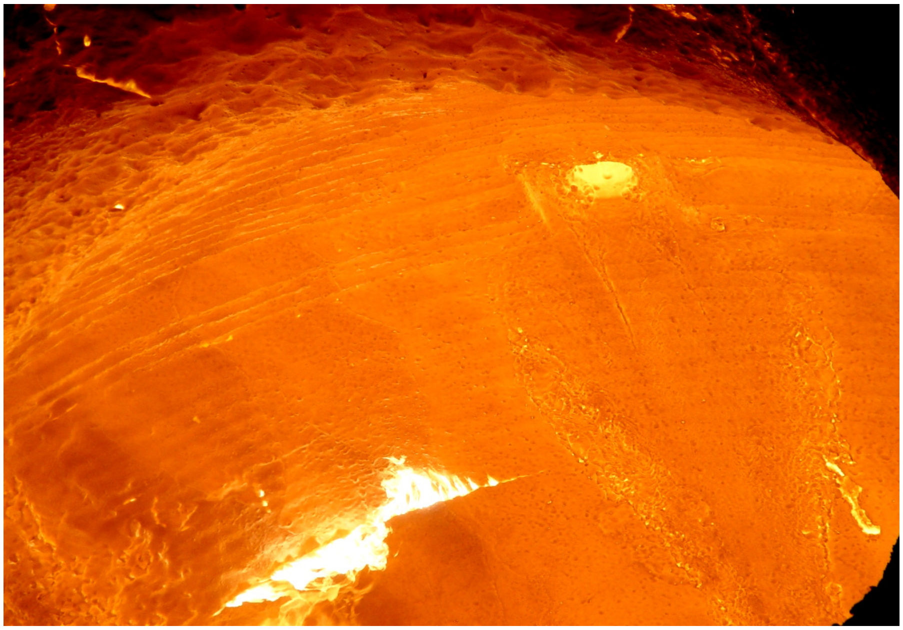

Fig. 1.2. Interior of a blast oxygen furnace used for the conversion of raw iron into steel

Raw materials used for the production of refractory materials applied in the steel industry are typically alumina (Al_2O_3), silica (SiO_2) and magnesia (MgO). The constituents used, the grain size distribution and the composition of grains in the matrix depend on the interaction with the contained atmosphere. Refractory products can be categorized into shaped refractory bricks and unshaped products such as castable concretes. After the selection of the raw materials and consecutive grinding the half-manufactured product is graded into the desired grain size distribution. During the subsequent mixing (wet and dry) binding agents and other additives are added. Subsequently the half-manufactured product is formed and pressed into the desired (brick) shape and attains its final properties during various thermal treatments. The structural integrity is obtained in the final sintering stage. After wet mixing the unshaped refractory products are casted on site into the desired shape, for example in a trough, in which the raw iron is flowing from the blast furnace to the torpedo car. The casted refractory lining receives its end properties in a careful drying process to avoid pressure built-up by evaporating water. An example of the resulting typical heterogeneous refractory micro-structure is depicted in Fig.1.3. Evidently, the macroscopic thermo-mechanical properties are determined by those of the various constituents and the coherence between them. At the macroscopic continuum scale heterogeneous temperature fields will cause constrained deformations and associated stresses, possibly additionally enforced by external (boundary) effects, e.g. due to neighbouring bricks. At the microscopic scale high temperatures (and fine scale temperature gradients) will cause complementary material loading due to local property mismatches.

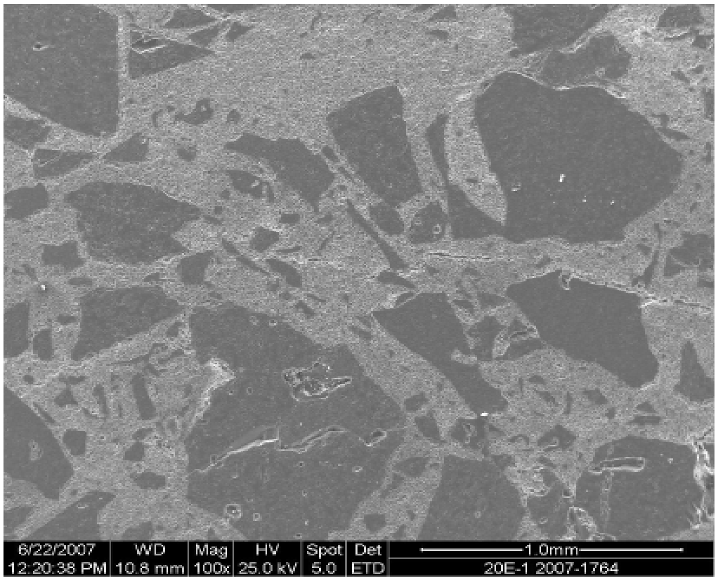

Fig. 1.3. SEM image (SEI) of a typical micro-structure of a heterogeneous, coarse grain refractory material

A principal cause of premature disfunctioning of steelmaking installations is the wear of the refractory lining due to fatal thermal loads. This occurs for example when liquid steel is poured into a relatively cold ladle or when an operating furnace is suddenly opened and the hot refractory material becomes exposed to cold air leading again to severe thermal stresses and the possible loss of the structural integrity of the material. The generation of such stresses is generally referred to as thermal shock. Fig. 1.4, for example, depicts a refractory lining of a hot air duct damaged by thermal shock which in general hampers the lifetime of high temperature installations and consequently affects their operational condition. The resulting loss of productivity may eventually lead to an increase in the steel production costs. This necessitates the prediction of thermal shock damage beforehand, in the design phase of installations as well as afterwards in post-failure analyses.

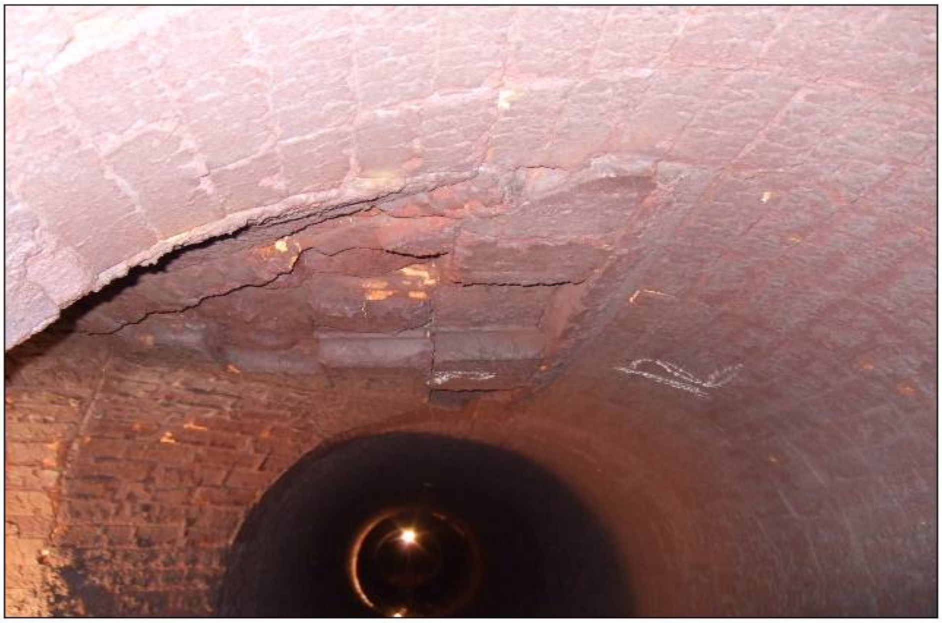

Fig. 1.4. Thermal shock damage in a hot air duct used for the firing of a blast furnace

In the past, the occurrence of thermal shock in refractory materials has been assessed simply by the comparison of material properties as for example tensile strength and thermal expansion coefficient. A slightly more advanced approach commonly used for purposive ranking of refractory materials is based on a combination of material properties as defined by Hasselman [1-3]. For example the resistance of a refractory material against thermal shock fracture initiation is represented by the first Hasselman parameter R defined as:

$$R = \frac{\sigma(1-\nu)}{\alpha_{th} E}$$

with σ the tensile strength, ν the Poisson's ratio, α_{th} the coefficient of thermal expansion and E denoting Young's modulus. The parameter R represents the maximum allowable temperature difference in a material subject to infinitely fast heating-up. Thermal shock resistance parameters have also been defined for other conditions of heating for example with a constant heat flux or constant heating rate. Evidently these parameters (refered to as additional Hasselman parameters R' and R'', respectively) do not take into account the complex geometry of high temperature installations and the imposed process conditions involving simultaneous mechanisms of heat transfer as for example forced convection and radiation.

Computer modelling of thermal shock in high temperature installations still relies heavily on the calculation of thermo-elastic stresses [4-8] and fracture mechanics [9-11]. Contributions in the field of damage mechanics have also been made [12-14] but are mostly limited to the modelling of parts of high temperature installations. Moreover they do not adequately take into account the heterogeneous granular micro-structure of refractory materials which is required for a realistic prediction of the thermo-mechanical degradation. Recently developed thermo-mechanical multi-scale models [15], [16] do incorporate the refractory micro-structure with all its features as for example grains of different size, porosity and a constitutive description of the coherence between the various constituents. These models are thus an excellent tool for purposive materials engineering. However, the straightforward identification of the many model parameters involved in the governing constitutive descriptions is difficult, whereas they are essential for the predictive modelling of thermal shock failure in high temperature installations.

Experimental assessments of thermal shock in refractory materials are readily available. In its most simple form this comes down to the quenching of heated samples in cold water. The resulting thermal shock damage is characterized a.o. by the determination of residual mechanical properties [17-20] or the weight loss after thermal spalling [21]. More accurate but expensive characterization methods include X-ray and ultrasonic tomography [22-24]. Fig. 1.5 shows a picture of a more enhanced set-up to test and compare the thermal shock resistance of refractory bricks. A batch of refractory bricks is stacked row-wise on the furnace and is alternatingly exposed to flame heating and forced cooling by ambient air. The thermal shock damage is characterized by acoustic measurements, only representative for the integral material degradation per test sample. In a more sophisticated approach the thermal boundary conditions imposed on a test sample need to be controllable and reproducible as opposed to for example the irregularly heated sample surface by a burner or the presence of boiling water around a test sample subject to water quenching. In order to adequately represent thermal shock failure under process conditions a sufficiently high thermal load needs to applied to a test sample.

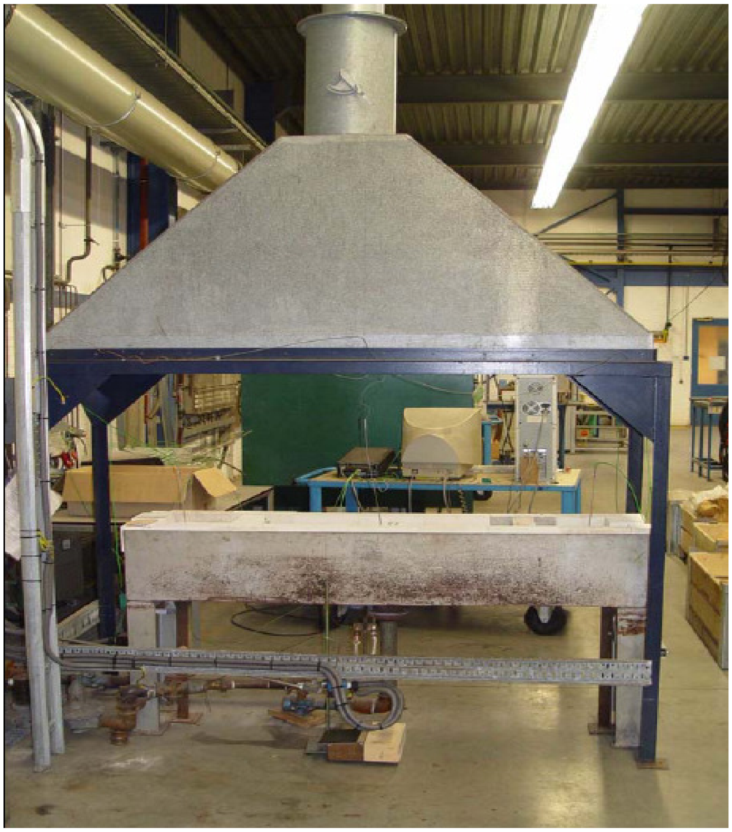

Fig. 1.5. Experimental set-up to test the thermal shock resistance of refractory bricks, alternatingly by flame heating and forced air cooling

1.2 Objectives

Thermo-mechanical damage and in particular thermal shock in a refractory lining of steelmaking installations compromises the productivity and the cost efficient production of steel. Numerical tools to predict thermal shock failure in engineering installations taking into account the distinct heterogeneous microstructure of refractory materials are currently not available. Proposed set-ups for the experimental assessment of thermal shock can only be used for the purposive ranking of refractory materials, but are usually not suitable to study thermal shock under cyclic process conditions and cannot be used for the identification of model parameters. Therefore, the following objectives are defined within the scope of the present research:

- The development of a constitutive model of the transient thermo-mechanical degradation of coarse grain refractory materials including terms to account for the fine scale degradation stemming from the distinct heterogeneous micro-structure. The constitutive framework will be implemented into a FE solution strategy.
- The realization of an experimental set-up to apply thermal shock to coarse grain refractory materials in a reproducible way with controlled, simulated process conditions. For the identification of model parameters it is furthermore required that the material degradation can be reproducibly quantified at multiple sample locations in a non-destructive way.
- The development of a numerical-experimental procedure for the identification of all model parameters including those controlling the fine scale degradation.
- The numerical platform is to be used to predict thermal shock damage in the refractory lining of high temperature installations. The effects of modifying the process conditions will be investigated, revealing possible proposals for improvement.

1.3 Outline of the thesis

In order to model the transient thermo-mechanical damage and in particular thermal shock in coarse grain refractory materials, a non-local constitutive damage framework is presented in paper 2 including terms to account for fine-scale damage induced by property mismatches at the micro-scale. Both-elasticity-based damage due to constrained non-uniform thermal expansion and thermal damage due to uniform thermal expansion are combined into a single variable for the damage. After implementation of the constitutive model into a thermo-mechanical finite element code, the influence of non-locality and fine-scale damage is investigated in a sensitivity analysis. The phenomenological relevance of the model is established by the numerical simulation of thermal experiments under process conditions. A literature review of various thermal shock test set-ups is presented in chapter 3. The experimental set-up conceived in the present research as well as the proposed acoustic damage characterization method and mechanical validation thereof are treated in detail. The evolution of damage in consecutive thermal shock cycles is investigated with the experimental set-up which comprises the surface contact of test samples with molten aluminium followed by a down quench in ambient air. The damage is characterized by the measurement of the transit time of ultrasonic longitudinal waves at various sample locations. The sensitivity of the sample material to a uniform temperature increase is investigated with quasi-stationary thermal experiments. Rate-dependent damage evolution laws are proposed in chapter 4 to describe the evolution of cyclic thermal shock damage. The enhanced damage framework accounts for the experimentally observed interaction between elasticity-based damage and thermal damage. The quantification of the governing evolution laws by making use of the quasi-stationary thermal tests and by inverse modelling of the consecutive thermal shock experiments is discussed including the extraction of longitudinal wave propagation characteristics from the numerical results to enable the comparison with the experiments. Subsequently, the validation of the identified parameter set is treated, indicating potential improvements to the thermal shock test set-up through a parameter identifiability analysis. The optimized model is used to investigate the damage evolution in three consecutive thermal shock cycles. In chapter 5, an incremental coupling between the quantified damage framework and a FE package is proposed to enable the modelling of thermal shock damage in thermally loaded structures subject to cyclic process conditions. The predictive capabilities of the thermo-mechanical damage framework is demonstrated with two numerical examples involving thermal shock damage in the inlet of a steel degassing installation and in the refractory lining of a steel ladle. The thesis closes with general conclusions and recommendations for further work.

1.4 References

[1] D.P.H. Hasselman, *Thermal stress resistance parameters for brittle refractory ceramics: a compendium,* Ceramic Bulletin, 1970, Vol. 49, pp. 1033-1037

[2] D.P.H. Hasselman, *Figures-of-merit for the thermal stress resistance of high-temperature brittle materials : a review,* Ceramurgia International, 1978, Vol. 4, pp. 147-150

[3] D.P.H. Hasselman, *Unified theory of thermal shock fracture initiation and crack propagation in brittle ceramics,* J. Am. Cer. Soc., 1969, Vol. 52, pp. 600-604

[4]. D. Rubesa, *Thermal stress fracture and spalling of well blocks in steel ladles – modeling and numerical simulation,* Veitsch-Radex Rundschau, 1999, Vol. 2, pp. 3-24

[5] J. Knauder, R. Rathner, *Thermo-mechanical analysis of basic refractories*, Radex-Rundschau, 1990, Heft 4

[6] J. Knauder, R. Rathner, *Improved design of a BOF-lining based on thermo-mechanical analysis,* Radex-Rundschau, 1990, Heft 1

[7] S. Yilmaz, *Thermomechanical modelling for refractory lining of a steel ladle lifted by crane,* Steel Research, 2003, Vol. 74(8), pp. 485-490

[8] R. Rathner, *Lining design and behavior of BOF's,* Radex-Rundschau, 1990, Heft 4

[9] J.P. Schneider, B. Coste, *Thermo-mechanical modeling of thermal shock in anodes,* Conf. Proceedings, Light Metals 1993, The Minerals, Metals & Materials Society, 1993

[10] D. Gruber, T. Auer, *FEM based thermo-mechanical investigations of RH-snorkels,* Proceedings of the Unified International Technical Conference on Refractories, Nov. 8-11 2005, The Am. Cer. Soc., Ed. J.D. Smith, 2005

[11] K. Andreev, H. Harmuth, D. Gruber, H. Presslinger, *Thermo-mechanical behaviour of the refractory lining of a BOF converter – a numerical study,* Proceedings of the Unified International Technical Conference on Refractories, Oct. 19-22 2003, Osaka, Japan, 2003

[12] X. Liang, W.L. Headrick, L.R. Dharani, S. Zhao, J. Wei, *Failure analysis of refractory cup under thermal loading and chemical attack using continuum damage mechanics,* Proceedings of the Unified International Technical Conference on Refractories, Nov. 8-11 2005, The Am. Cer. Soc., pp. 980-984, Ed. J.D. Smith, 2005

[13] B.M. Luccioni, M.I. Figueroa, R.F. Danesi, *Thermo-mechanic model for concrete exposed to elevated temperatures*, Engng Structures, 2003, Vol. 25, pp. 729-742

[14] X. Liang, W.L. Headrick, L. R. Dharani, S. Zhao, *Modeling of failure in a high temperature black liquor gassifier refractory lining,* Engng. Failure Analysis, 2007, Vol. 14, pp. 1233-1244

[15] I. Özdemir, W.A.M., Brekelmans, M.G.D. Geers, *Computational homogenization for heat conduction in heterogeneous solids,* Int. J. Num. Meth. Eng., 2008, Vol. 73(2), pp. 185-204

[16] I. Özdemir, W.A.M., Brekelmans, M.G.D. Geers, *FE^2 computational homogenization for the thermo-mechanical analysis of heterogeneous solids,* Comp. Meth. Appl. Mech. Eng., 2008, Vol. 198(3-4), pp. 602-613

[17] W.J. Wei, Y. P. Lin, *Mechanical and thermal shock properties of size graded MgO-PSZ refractory*, J. Eur. Cer. Soc., 2000, Vol. 20, pp. 1159–1167

[18] T. Volkov and R. Jancic, *Prediction of thermal shock behavior of alumina based refractories, fracture resistance parameters and water quench test,* In Proceedings of CIMTEC 2002, ed. P. Vincenzini and G. Aliprandi, 2003, pp. 109–116

[19] Y.C. Ko, W.H. Horng, C.H. Wang and L.C. Chieh Teng, *Fines content effects on the thermal shock resistance of Al2O3-Spinel Castables,* Chin.Steel Tech. Rep., 2001, Vol. 15, pp. 7–14

[20] C. Aksel, *The effect of mullite on the mechanical properties and thermal shock behaviour of alumina-mullite refractory materials,* Ceram. Int., 2003, Vol. 29, pp. 183–188

[21] H.G. Geck, H.J. Langhammer and A. Chakraborty, *Kammerofen zur betriebsnahen Prüfung der Temperaturwechselbeständigkeit feuerfester Steine*, Stahl und Eisen, 1973, Vol. 93(21), pp. 967–976

[22] E.N. Landis, E.N. Nagy, D.T. Keane and G. Nagy, *Technique to measure 3D work-of-fracture of concrete in compression*, J. Eng. Mech., 1999, June, pp. 599–605

[23] M. Daigle, D. Fratta and L.B. Wang, *Ultrasonic and X-ray tomographic imaging of highly contrasting inclusions in concrete specimens*, Proceedings of GeoFrontier 2005 Conference, 2005

[24] E.N. Landis, *Towards a physical damage variable for a heterogeneous quasi-brittle material*, Proceedings of 11th International Conference on Fracture, 2005, p. 1150

2. Non-local modelling of thermal shock damage in refractory materials

A non-local damage framework has been coupled with heat transport to model transient thermo-mechanical damage (in particular thermal shock) in refractory materials. The non-locality, to be dealt with to obtain an adequate problem formulation, is introduced by terms accounting for micro-structural strain gradients induced by transient temperature gradients. The parameters figuring in the evolution law for elasticity-based damage are temperature-dependent. Damage due to isotropic thermal expansion has been accounted for by proposing a new evolution law. A single variable for the total damage is obtained by combining both damage mechanisms. The influence of non-locality and transient temperature gradients within non-locality is investigated in numerical examples. The phenomenological relevance of the framework is verified by modeling of experiments, which simulate thermal shock under process conditions.

2.1 Introduction

Refractory materials are used in linings of installations for iron and steelmaking with operating temperatures as high as 1800 °C. Major cause leading to early failure of such installations is the wear of the refractory material due to fatal thermal stresses. This happens e.g. when molten metal is introduced into a relatively cold ladle. Another example is the sudden opening of an operating furnace where hot refractory material suddenly becomes exposed to cold air leading again to severe thermal stresses. The generation of such stresses is generally referred to as thermal shock.

In the past, various approaches have been used to model thermal shock in refractory materials. Parameters describing the effect of thermal shock in refractory materials were defined by Hasselman [1-3] and Lu and Fleck [4]. Also numerous analytical efforts have been undertaken to model thermal shock cracks in ceramic materials [5-11]. The application of the Finite Element Method permitted the study of evolution of thermal stresses and cracks by modeling parts of or even complete installations forming input to an improved re-design [12-18]. Despite the quasi-brittle character of refractory

Reproduced from: F. Damhof, W.A.M. Brekelmans, M.G.D. Geers, *Non-local modelling of thermal shock damage in refractory materials,* Engng. Fract. Mech., 2008, Vol. 75, pp. 4706-4720

materials early computer modeling was mostly based on Linear Elastic Fracture Mechanics. At a later stage quasi-brittleness was incorporated using Fictitious Crack models with fit-for-purpose constitutive laws [19], [20] extended with gradient terms to model size effects correctly [21]. Latest efforts entail consideration of the complex micro-structure of refractory material [22] and multi-scale models covering sizes from granular level up to full-size installations [23].

At thermal shock sensitive locations in installations coarse-grained refractory material is applied with grain sizes up to 5 mm. Such refractories show a diffuse (micro-) crack pattern upon exposure to thermal shock. Simonin et al. [24] report for a coarse-grained high-alumina refractory material both diffuse and localized thermal shock damage. Mismatch in thermal expansion of grains and matrix causes micro-cracks leading to diffuse thermal shock damage [25], [26] catalyzed by pre-existing micro-cracks stemming from the refractory production process. Boussuge [27], [28] confirmed that coarse-grained refractories develop a distributed damage preceding localization and proposes continuum damage mechanics [29] to model the material behaviour.

In the past various authors reported on modeling the thermo-mechanical behaviour of refractory materials based on damage mechanics. Headrick et al. [30] model combined thermo-mechanical and chemical damage in an alumina-silicate refractory lining of a gassifier. Separate damage variables are used for compressive and tensile failure. Prompt et al. [31] analyse the wear of a blast furnace duct. Based on the observed fracture pattern of micro- and macro-cracks due to high transient thermal gradients a continuum damage approach was adopted. A single damage variable was satisfactorily used to describe damage originating from a compressive stress state at the hot face and from a tensile stress state inside the refractory lining. Liang and Headrick [32] model filling of an alumina refractory cup using separate damage variables for compressive and tensile damage. The total damage is found via a multiplicative combination of the damage variables.

More advanced models are employed predicting damage in concrete exposed to elevated temperatures in a fire. Elasticity-based damage is combined with thermal damage (e.g. from micro-cracking due to isotropic thermal expansion). Total damage is obtained via a multiplicative combination of both damage descriptions. Gawin [35] et al. follow a scalar damage approach while the constitutive behaviour is distinct for compression and tension. Damage evolution parameters are assumed temperature-independent. Luccioni et al. [34] perform a similar exercise where thermal damage manifests itself through the deterioration of Young's modulus including an effect on Poisson’s ratio. Nentech et al. [33] use separate compressive and tensile damage variables combined with hardening plasticity. A third damage variable is used to account for thermal damage. It was proposed to incorporate an internal length scale (representing the dimensions of the material micro-structure) into the constitutive equations to preserve the well- posedness of the problem upon strain localization and to avoid mesh dependency in a finite element analysis. This can be realized by using e.g. a non-local equivalent strain measure as was shown by Stabler and Baker [36], [37] who model damage due to temperature gradients (elasticity-based damage) combined with thermal damage. The elasticity-based damage is activated by a non-local strain measure obtained via Gaussian weighting applied to the local equivalent strain field. Pearce et al. [38] also follow a non-local approach incorporating elasticity-based and thermal damage with temperature-dependent evolution parameters. The non-local strain measure is, however, obtained via an implicit gradient enhanced formulation as advocated by Peerlings et al. [39], [40] to preserve mathematical well-posedness. None of the approaches mentioned in this paragraph reflect on fine scale thermal shock damage originating from thermal expansion mismatches in the micro-structural constituents. Furthermore the transient evolution of non-local damage was not investigated and the incorporation of temperature dependency in the damage frameworks was found incomplete as to correctly describe the temperature-dependent mechanical behaviour of refractory material.

To represent transient temperature damage in granular coarse-grained refractory material it is proposed in this paper to model elasticity-based (thermal shock) damage isotropically. This is combined with a newly described evolution of thermal damage in an additive manner implying that both damage mechanisms act independently. This is jusitified by the fact that the elastic damage predominantly works macroscopically whereas the origin of thermal damage is of microscopic nature. The total damage thus represents a separation of macroscopic and microscopic scales. The driving variable for elasticity-based damage, the non-local equivalent strain, is obtained via a gradient enhanced implicit formulation. Coupling of this formulation with elastic equilibrium and transient heat transport leads to transient non-local damage evolution which has not been modelled before. Contrary to previous works on desintegration of concrete and refractories at elevated temperature, the elasticity-based damage evolution law uses temperature-dependent parameters. The modified Von Mises definition in [39], used to obtain the local equivalent strain, is enhanced in this paper by the incorporation of a temperature-dependent ratio of compressive and tensile strength. The existing non-locality equation is in this paper extended with a term accounting for fine scale transient thermal shock damage due to property mismatches at the micro-scale. A full Newton-Raphson scheme is used to implement the presented field equations in a Galerkin based finite element framework. In sensitivity analyses the influence of the contribution of said fine scale thermal shock damage as well as an increasing internal length scale is investigated. The phenomenological relevance of the modeling framework is established by comparing the data from thermal shock experiments with the numerical model thereof.

2.2 Temperature-dependent mechanical behaviour

The areas within high temperature installations prone to thermal shock are equipped with specifically tailored refractory materials. A typical example of the chemical composition of such a refractory material is presented in Fig. 2.1 (left). The weight percentages of alumina (Al_2O_3) and silica (SiO_2) govern to a large extent the thermo-mechanical characteristics of the material. Generally, larger alumina content leads to a lower thermal shock resistance. Nonetheless alumina-silicate bricks are used in harsh high temperature environments because of their high-temperature strength combined with a reasonable thermal shock resistance. Such bricks are mainly composed of mullite ($3Al_2O_3.2SiO_2$) with some glassy phases of SiO_2, generally located around the grain boundaries. These glassy phases begin to soften when approaching their glass transition temperature leading to a quasi-brittle behaviour at higher temperatures [41]. Usually this glass transition temperature lies well below the ultimate usage temperature of the refractory material. Fig. 2.1 (right) shows a typical uni-axial response in tension of a dense refractory material. Upon temperature increase a transition from purely brittle towards a more quasi-brittle behaviour takes place; the post-elastic tail preceding ultimate failure becomes longer. Also the strain at which the peak stress occurs, increases with temperature. Other characteristic changes at increasing temperature are a lower strength and a lower Young's modulus. The aforementioned temperature dependencies need to be incorporated into the constitutive model.

Constituent	Rel. weight (%)
SiO_2	37.6
Al_2O_3	59.5
CaO	0.18
MgO	0.19
TiO_2	0.37
Fe_2O_3	1.26
P_2O_5	0.03
Na_2O	0.2
K_2O	0.42
MnO	0.01

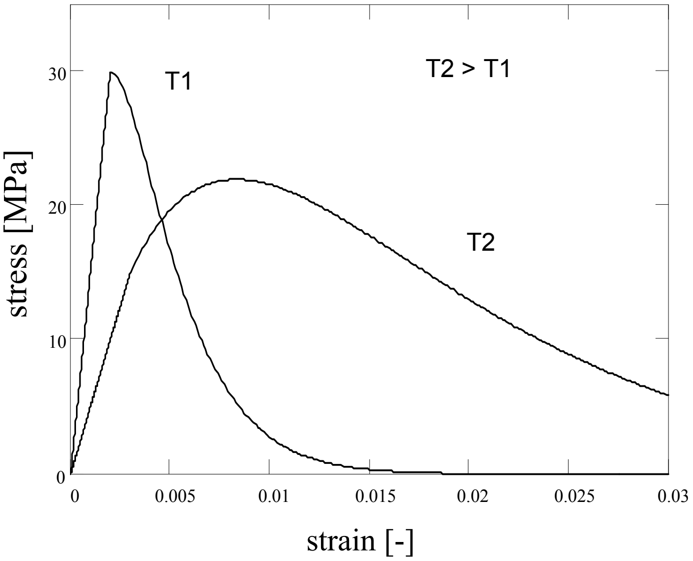

Fig. 2.1. Chemical composition (left) and temperature-dependent mechanical response of a typical alumina-silicate brick (right)

2.3 Constitutive model

2.3.1 Damage evolution

The total strain in a thermo-mechanically loaded refractory material is composed of a thermal strain and an elastic strain defined with respect to a predefined reference configuration. The thermal strain is due to the isotropic thermal expansion following a temperature increase with respect to the reference. The elastic strain originates from stresses due to external material constraints (e.g. neighboring bricks) and due to the constrained thermal expansion within the material itself. The total strain tensor $\boldsymbol{\varepsilon}$ is decomposed according to:

$$\boldsymbol{\varepsilon} = \boldsymbol{\varepsilon}_{th} + \boldsymbol{\varepsilon}_{el} \tag{2.1}$$

where $\boldsymbol{\varepsilon}_{th}$ and $\boldsymbol{\varepsilon}_{el}$ represent the thermal and elastic strain tensor, respectively. The thermal strain tensor can be written as:

$$\boldsymbol{\varepsilon}_{th} = \alpha_{th} \left(\theta - \theta_0\right) \boldsymbol{I} \tag{2.2}$$

where α_{th} is the thermal expansion coefficient, θ and θ_0 denote the actual temperature and the reference temperature in the unstrained state, respectively, and $\boldsymbol{I}$ is the identity tensor. For isotropic elastic damage affected behaviour, Hooke's law reads

$$\boldsymbol{\sigma} = (1 - D)\, {}^4\boldsymbol{C} : (\boldsymbol{\varepsilon} - \boldsymbol{\varepsilon}_{th}) \tag{2.3}$$

where the damage D accounts for both the elasticity-based and the thermal damage and $\boldsymbol{\sigma}$ denotes the stress tensor. The fourth-order tensor ${}^4\boldsymbol{C}$ contains the temperature-dependent elasticity moduli of the undamaged material. The elasticity-based damage is predominantly a macroscopic phenomenon whereas thermal damage is of microscopic origin and induced by thermal expansion mismatches within the micro-structure of the material. For lower damage levels this implies a separation of macroscopic (elastic damage) and microcopic (thermal damage) scales and independently acting damage mechanisms. Hence the total damage D can be written as:

$$0 \le D = d_{el} + d_{th} \le 1 \tag{2.4}$$

where d_{el} represents the elasticity-based damage and d_{th} the thermal damage.

For the elasticity-based damage the following evolution law is proposed [39]:

$$d_{el} = 1 - \frac{\kappa_{el,i}}{\kappa_{el}} \left[(1 - \alpha) + \alpha \exp^{-\beta(\kappa_{el} - \kappa_{el,i})} \right] \tag{2.5}$$

where κ_{el} is the damage driving variable, $\kappa_{el,i}$ denotes its minimum threshold value, α and β are temperature-dependent material parameters where the latter reflects the brittleness of the material. The driving variable κ_{el} is determined through the Kuhn-Tucker relations for damage evolution:

$$\dot{\kappa}_{el} \ge 0,\ \bar{\varepsilon}_{eq} - \kappa_{el} \le 0,\ \dot{\kappa}_{el}(\bar{\varepsilon}_{eq} - \kappa_{el}) = 0 \tag{2.6}$$

where $\bar{\varepsilon}_{eq}$ represents the non-local equivalent strain which equals κ_{el} upon damage evolution. The local and non-local equivalent strains are defined in detail in section 2.3.2. The temperature-dependency of the material parameters α and β may cause an unphysical decrease of the damage unless the numerical implementation is adequately adapted to prevent this inconsistency.

The driving variable for the thermal damage is the maximum attained temperature within the material. A uniform temperature increase induces an isotropic thermal expansion. When the temperature exceeds a certain threshold value small (microscopic) cracks might appear causing irreversible thermal damage [33-38]. From a structural point of view this thermal damage is a typical fine scale micro-structural mechanism, associated to local mismatches in elastic and thermal properties of the constituent phases in the micro-structure. On the other hand certain chemical components of refractory material (e.g. SiO_2) might be subject to phase changes at elevated temperatures. This can lead to a change in the material structure (e.g. local volume changes) and a permanently decreased Young's modulus, which thus also contributes to the thermal damage. For the evolution of thermal damage a new evolution law is proposed:

$$d_{th} = 1 + \sin\left(\frac{1}{2}\pi \left(3 - \left(\frac{\kappa_{th} - \kappa_{th,i}}{\kappa_{th,c} - \kappa_{th,i}} \right)^{\varphi} \right) \right) \tag{2.7}$$

where κ_{th} represents the driving variable for thermal damage: the attained maximum temperature. The parameters $\kappa_{th,i}$ and $\kappa_{th,c}$ denote, respectively the initial and critical temperature for thermal damage. When κ_{th} approaches $\kappa_{th,c}$ the thermal damage would become 1. Normally process temperatures will never reach $\kappa_{th,c}$ and consequently thermal damage will never reach the value 1. The parameter φ in Eq. (2.7) can be chosen such that the thermal damage increases progressively, linear or degressively at increase of the maximum attained temperature. The driving variable κ_{th} is subject to the Kuhn-Tucker relations for the thermal damage evolution:

$$\dot{\kappa}_{th} \geq 0 \, , \; \theta - \kappa_{th} \leq 0 \, , \; \dot{\kappa}_{th}\left(\theta - \kappa_{th}\right) = 0 \tag{2.8}$$

2.3.2 Equivalent strain

For the local equivalent strain the modified Von Mises definition [39] is suitable:

$$\varepsilon_{eq} = \frac{\eta - 1}{2\eta(1-2v)} J_1 + \frac{1}{2\eta} \sqrt{\left(\frac{\eta - 1}{1-2v}\right)^2 J_1^2 + \frac{6\eta}{(1+v)^2} J_2} \tag{2.9}$$

where η is the temperature-dependent ratio of compressive and tensile strength such that an uni-axial compressive stress $\eta\sigma$ leads to identical damage as a tensile stress equal to σ; J_1 and J_2 are invariants of the elastic strain tensor $\boldsymbol{\varepsilon}_{el}$:

$$J_1 = \mathrm{tr}(\boldsymbol{\varepsilon}_{el}),\; J_2 = \mathrm{tr}(\boldsymbol{\varepsilon}_{el} \cdot \boldsymbol{\varepsilon}_{el}\;) - \frac{1}{3}\mathrm{tr}^2(\boldsymbol{\varepsilon}_{el}) \tag{2.10}$$

The formulation of κ_{el} according to (2.6) in terms of a local equivalent strain as described in Eq. (2.9) would lead to a pathological mesh dependency in Finite Element solutions [39]. This can be resolved by adopting a non-local approach involving a weighted average of the equivalent strains within a certain vicinity of a material point. This can e.g. be achieved by using an integral format:

$$\bar{\varepsilon}_{eq}(\vec{x}) = \int_V g(\vec{\xi})\varepsilon_{eq}(\vec{x} + \vec{\xi})dV \tag{2.11}$$

where the non-local equivalent strain $\bar{\varepsilon}_{eq}(\vec{x})$ is the weighted volume average of the local equivalent strain ε_{eq}. Furthermore $g(\vec{\xi})$ is a weight function and $\vec{\xi}$ is relative position vector. As demonstrated by Peerlings et al. [39], Eq. (2.11) can be approximated by the following differential form:

$$\bar{\varepsilon}_{eq} = \varepsilon_{eq} + l_c^2 \nabla^2 \varepsilon_{eq} \tag{2.12}$$

where l_c is a material dependent internal length scale parameter representing the dimensions of the micro-structure of the material and ∇^2 represents the Laplacian operator. Apart from the numerical benefits the adoption of a non-local equivalent strain thus reflects the coarse-grained granular material structure represented by the internal length scale l_c. From a numerical point-of-view it is beneficial to transform Eq. (2.12) into its implicit form [39]:

$$\bar{\varepsilon}_{eq} - l_c^2 \nabla^2 \bar{\varepsilon}_{eq} = \varepsilon_{eq} \tag{2.13}$$

It has been shown previously [39], [43] that the implicit determination of the non-local strain from the applied elliptic partial differential equation gives good results in controlling the predictions of damage models prior to material failure. Eq. (2.13) reflects that the local equivalent strain can be considered as the source term in the differential equation for the non-local equivalent strain and thus as the governing source for damage evolution.

The evolution of thermal shock damage originates from events at two scales. Long range elastic fields at the macro-scale are induced by the thermal gradients at the continuum level, accounted for in Eq. (2.13). However, for thermal shock, a second source of damage exists, associated to a fine scale distribution of deformations. This is induced by microscopic temperature gradients acting on the heterogeneous micro-structure where thermal expansion mismatches are present. Hence the temperature gradients may lead to excessive micro-scale stresses and damage. The governing micro-scale deformation is represented by a micro-structural local equivalent strain which is taken to be proportional to the spatial variation of temperature, defined here as:

$$\varepsilon_{eq,micro} = r_{ths} \left| \bar{\theta} - \theta \right| \tag{2.14}$$

where r_{ths} is a proportionality constant and the non-local temperature $\bar{\theta}$ is obtained via a weighted average of the local temperature θ within a certain vicinity of the material point concerned, analogically defined as the non-local equivalent strain in Eq. (2.11). The fine scale influence of temperature gradients on the granular material structure is reflected in Eq. (2.14). The influence of strain gradients on the micro-scale strains of the heterogeneous materials is thus accounted for. The influence of the local temperature itself is dealt with within the framework of thermal damage. In line with Eq. (2.12), the non-local temperature $\bar{\theta}$ can be approximated by:

$$\bar{\theta} = \theta + l_{ths}^2 \nabla^2 \theta \tag{2.15}$$

where l_{ths} is a material dependent internal length scale parameter representing the dimensions of the micro-structure of the material and the governing material characteristics which incorporate the previously discussed fine-scale thermo-mechanic behaviour. Eq. (2.15) can be substituted into Eq. (2.14), yielding:

$$\varepsilon_{eq,micro} = c_{ths} \left| \nabla^2 \theta \right| \tag{2.16}$$

where the constant c_{ths} replaces the product $r_{ths}\, l_{ths}^2$. Taking into account the diffusion equation for heat transfer without source terms, which reads:

$$\nabla^2 \theta = \frac{1}{\alpha_{dif}} \dot{\theta} \tag{2.17}$$

(with the thermal diffusivity $\alpha_{dif} = \lambda / \rho\, C_p$, λ the thermal conductivity, ρ the mass density and C_p the heat capacity), it follows that adding the second source term, Eq. (2.16), to Eq.(2.13) results in:

$$\bar{\varepsilon}_{eq} - l_c^2 \nabla^2 \bar{\varepsilon}_{eq} = \varepsilon_{eq} + \frac{c_{ths}}{\alpha_{dif}} \left| \dot{\theta} \right| \tag{2.18}$$

If temperature changes proceed quasi-stationary the second source term vanishes from Eq. (2.18). From the definition of α_{dif} it follows from Eq. (2.18) that a higher thermal conductivity (λ) as well as a lower heat capacity ($\rho\, C_p$) lead to less thermal shock damage, provided that c_{ths} is not affected.

2.4 Finite element implementation

This section outlines the implementation of the previously described mathematical model into a Galerkin-based finite element program. The solution process is based on a full Newton-Raphson linearization of the discretized weak forms.

2.4.1 Weak forms and discretization of the governing equations

The system to be solved consists of the equations for heat transport without internal sources, equilibrium without body forces and the equation for the non-local equivalent strain Eq. (2.18):

$$\nabla^2 \theta = \frac{1}{\alpha_{dif}} \dot{\theta} \tag{2.19}$$

$$\vec{\nabla} \cdot \boldsymbol{\sigma} = \vec{0} \tag{2.20}$$

$$\bar{\varepsilon}_{eq} - l_c^2 \nabla^2 \bar{\varepsilon}_{eq} = \varepsilon_{eq} + \frac{c_{ths}}{\alpha_{dif}} \left| \dot{\theta} \right| \tag{2.21}$$

The boundary conditions involved with the differential equations (2.19) and (2.20) are straightforwardly prescribed by the physical problem description. A physically acceptable boundary condition for Eq. (2.21) reads [39]:

$$\vec{\nabla} \bar{\varepsilon}_{eq} \cdot \vec{n} = 0 \tag{2.22}$$

where $\vec{n}$ denotes the normal at the edge of the domain Ω considered. Using a Galerkin discretization of the relevant fields and substitution into the weak forms of Eqs. (2.19) to (2.21) yields:

$$\int_{\Omega} \underline{N}_{\theta}^{T} \rho C_p \underline{N}_{\theta} \, d\Omega \, \underset{\sim}{\dot{\theta}} + \int_{\Omega} \underline{B}_{\theta}^{T} \lambda \underline{B}_{\theta} \, d\Omega \, \underset{\sim}{\theta} = \underset{\sim\, ext}{f^{\theta}} \tag{2.23}$$

$$\int_{\Omega} \underline{B}_{u}^{T} \, \underset{\sim}{\sigma} \, d\Omega = \underset{\sim\, ext}{f^{u}} \tag{2.24}$$

$$\int_{\Omega} \left(\underline{N}_{e}^{T} \underline{N}_{e} \underset{\sim eq}{\bar{\varepsilon}} + \underline{B}_{e}^{T} l_c^2 \underline{B}_{e} \underset{\sim eq}{\bar{\varepsilon}} - \underline{N}_{e}^{T} \varepsilon_{eq} \right) d\Omega - \int_{\Omega} \underline{N}_{e}^{T} \frac{c_{ths}}{\alpha_{dif}} \underline{N}_{\theta} \, d\Omega \left| \underset{\sim}{\dot{\theta}} \right| = \underset{\sim\, ext}{f^{e}} \tag{2.25}$$

where the matrices $\underline{N}_{\theta}$ and $\underline{N}_{e}$ contain the interpolation functions for temperature and non-local equivalent strain, respectively. The matrices $\underline{B}_{\theta}$, $\underline{B}_{u}$ and $\underline{B}_{e}$ contain derivatives of the interpolation functions for temperature, displacement and non-local equivalent strain. The column $\underset{\sim}{\dot{\theta}}$ contains the time derivatives of the nodal temperatures. The column $\underset{\sim}{\sigma}$ contains the components of the stress tensor $\boldsymbol{\sigma}$. The nodal columns $\underset{\sim}{f}{}^{\theta}_{ext}$, $\underset{\sim}{f}{}^{u}_{ext}$ and $\underset{\sim}{f}{}^{e}_{ext}$ represent, respectively, external heat fluxes, external mechanical forces and a column containing external non-local quantities (equaling zero).

2.4.2 Linearization and incremental-iterative solution procedure

For the temporal discretization of Eqs. (2.23) and (2.25) at increment level a backward-Euler scheme is applied. Linearization of the non-linear system of incremental equations has been performed taking into account the temperature dependency of the thermal conductivity, thermal capacity, Young's modulus and the ratio of compressive and tensile strength η. Successive substitution of the linearizations and time descretization into the spatially discretized weak forms Eqs. (2.23) - (2.25) yield the following linear system of equations, applicable for iteration step i:

$$\underline{K}_{i-1}\,\delta \underset{\sim}{a} = \underset{\sim}{f}_{ext} - \underset{\sim}{f}_{int,i-1} \tag{2.26}$$

with $\underline{K}_{i-1}$ the system matrix, $\delta \underset{\sim}{a}$ the column with adaptations of the estimated values of the nodal temperatures $\underset{\sim}{\theta}$, the nodal displacements $\underset{\sim}{u}$ and the nodal non-local equivalent strains $\underset{\sim}{\bar{\varepsilon}}_{eq}$ and $\underset{\sim}{f}_{int,i-1}$ the column with nodal reactions. In a decomposed format the iteration equation (2.27) can be written as:

$$\underline{K}_{i-1} = \begin{bmatrix} \underline{K}^{\theta\theta}_{i-1} & \underline{K}^{\theta u}_{i-1} & \underline{K}^{\theta e}_{i-1} \\ \underline{K}^{u\theta}_{i-1} & \underline{K}^{uu}_{i-1} & \underline{K}^{ue}_{i-1} \\ \underline{K}^{e\theta}_{i-1} & \underline{K}^{eu}_{i-1} & \underline{K}^{ee}_{i-1} \end{bmatrix},\ \delta \underset{\sim}{a} = \begin{bmatrix} \delta \underset{\sim}{\theta} \\ \delta \underset{\sim}{u} \\ \delta \underset{\sim}{\bar{\varepsilon}}_{eq} \end{bmatrix},\ \underset{\sim}{f}_{ext} = \begin{bmatrix} \underset{\sim}{f}{}^{\theta}_{ext} \\ \underset{\sim}{f}{}^{u}_{ext} \\ \underset{\sim}{f}{}^{e}_{ext} \end{bmatrix},\ \underset{\sim}{f}_{int,i-1} = \begin{bmatrix} \underset{\sim}{f}{}^{\theta}_{int,i-1} \\ \underset{\sim}{f}{}^{u}_{int,i-1} \\ \underset{\sim}{f}{}^{e}_{int,i-1} \end{bmatrix} \tag{2.27}$$

In Eq. (2.27) the sub-matrices $\underline{K}_{i-1}^{\theta u}$ and $\underline{K}_{i-1}^{\theta e}$ consist entirely of zero elements indicating that the temperature field is not influenced by damage development i.e. it is assumed that the thermal moduli do not depend on damage. For a more detailed elaboration of the remaining sub-matrices and sub-columns in Eq. (2.27) reference is made to Section 2.9.

2.4.3 Computational solution issues

The sub-matrices composing the global system matrix (Eq. (2.27)) are determined at the element level. Within the three-dimensional element, the temperature and non-local equivalent strain are approximated using tri-linear interpolation functions. The displacement components are approximated using quadratic interpolation functions in a serendipity configuration. Using the same order of interpolation might lead to stress oscillations as was found by Peerlings [43]. Within the context of the proposed quadratic displacement discretization the local elastic strain becomes of reduced order in agreement with the lower order damage stemming from the lower order temperature and non-local equivalent strain. It has been found that this approach gives good results when combined with reduced Gauss integration of the equilibrium equation and full integration of the field equation for the non-local equivalent strain, Eq. (2.21) [43]. Full Gauss integration has been applied for the heat transport equation as well. Note that this implies that eight integration points are used to evaluate the contributions for thermal diffusion, equilibrium and the non-local equivalent strain. Eventually this leads to a 20-noded quadratic serendipity finite element where the displacement components are evaluated at all nodes and the temperature and non-local equivalent strain only at the corner nodes.

2.5 Non-local aspects of thermal shock damage

The influence of the contribution of the transient temperature gradients in the non-locality equation (Eq. (2.21)) as well as the effect of an increasing internal length scale are investigated in sensitivity analyses. The influence of the value assigned to the thermal shock constant c_{ths} and to the intrinsic length l_c (Eq. (2.18)) has been investigated by the analysis of five cases (A to E), summarized in table 2.1. Fig. 2.2 shows the geometry and boundary conditions used in the analysis which is performed in a plane strain context.

The homogeneous initial sample temperature θ_0 equals 20 °C. The bottom sample side is subject to a temperature jump of 1500 °C. Symmetry conditions apply to the left sample side. The vertical displacements are constrained on the upper sample side, which is also thermally insulated. The right sample side is thermally insulated. Eqs. (2.28) and (2.29) specify the temperature-dependent thermal capacity and conductivity, based on measurements on typical refractory material in the relevant temperature regime

$$C_p(\theta) = 782 + 0.3\theta + 0.0003\theta^2 \qquad \text{[J/kgK]} \tag{2.28}$$

$$\lambda(\theta) = 1.979 + 0.0008\theta + 6 \cdot 10^{-7}\theta^2 \qquad \text{[W/mK]} \tag{2.29}$$

where θ is expressed in °C. The values of the model parameters used in this analysis are typical for refractory material. The density, Young's modulus, Poisson's ratio and thermal expansion coefficient used are, respectively, 2220 kg/m^3, 15 GPa, 0.2 and 6*10^{-6} K^{-1}. For the parameter η in the modified Von Mises definition, Eq. (2.9), a value of 4 has been selected. For the parameters α, β and $\kappa_{el,i}$ in Eq. (2.5) values of –1, 10 and 8*10^{-4}, respectively, have been chosen. Thermal damage was not activated. A discretization of 20x40 square elements has been used. A time frame of 30 s was analyzed using time steps of 0.5 s.

Case nr.	**A**	**B**	**C**	**D**	**E**
c_{ths} [m^2/K]	0	2.5*10^{-12}	5.0*10^{-12}	0	0
l_c [mm]	3	3	3	1	5

Table 2.1. Values of thermal shock constant and internal length scale used in the parameter sensitivity analysis

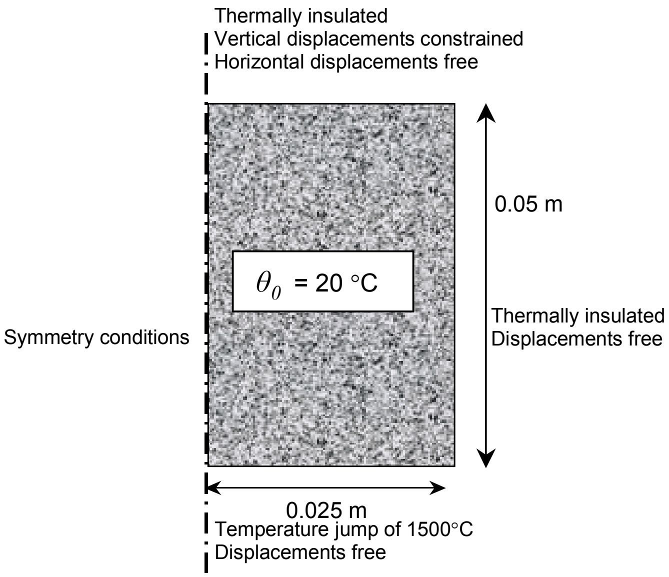
Thermally insulated
Vertical displacements constrained
Horizontal displacements free
0.05 m
θ_0 = 20 °C
Thermally insulated
Displacements free
Symmetry conditions
0.025 m
Temperature jump of 1500°C
Displacements free

Fig. 2.2. Sample subject to an upquench thermal shock

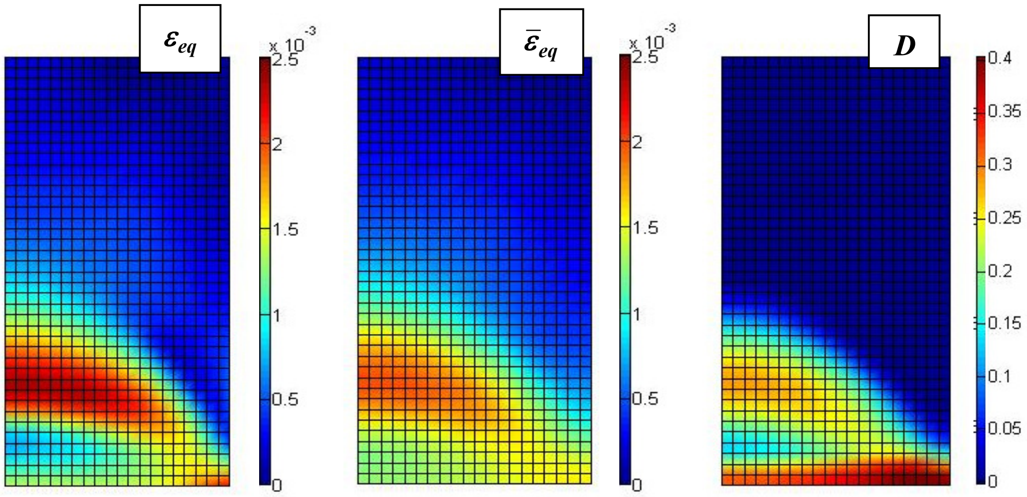

Fig. 2.3. Results for case C (c_{ths} = 5*10^{-12} m^2/K, l_c= 3 mm) at t = 10 s

Fig. 2.3 shows the results for case C at 10 seconds. Compared to the local equivalent strain the non-local equivalent strain is more smooth and has a lower maximum value. This is due to the averaging effect of the non-local formulation on the local equivalent strain field. The high values of the damage at the sample bottom are due to the thermal shock term in Eq. (2.18). This can also be observed in Fig. 2.4 which depicts the centerline non-local equivalent strain and damage as a function of time for the cases A to C. With increasing values of the thermal shock constant c_{ths} the damage at the sample bottom increases while the damage at quarter height and half height decreases slightly. The decrease in damage is due to the aforementioned averaging effect of non-locality. The time at which the maximum in damage is reached (event time), for quarter and half sample heights, hardly changes for the considered values of the thermal shock constant.

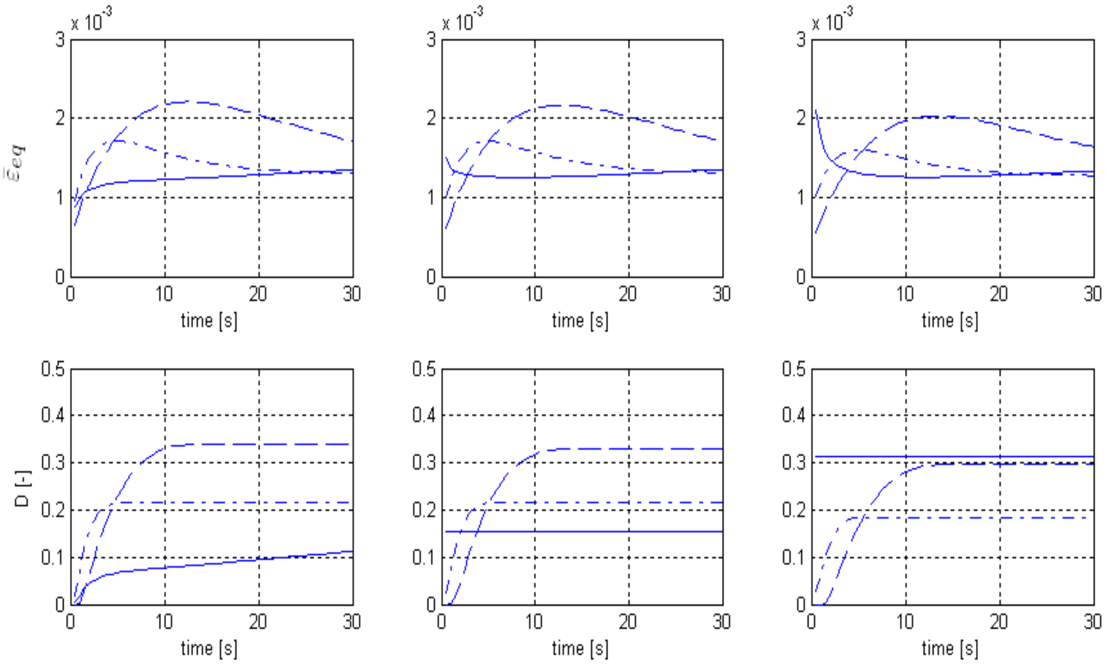

Fig. 2.4. Centerline non-local equivalent strain (upper row) and damage (lower row) as a function of time for the cases A to C (left to right). Solid line: sample bottom, dash-dot: quarter height, dashed: half height

Fig. 2.5 shows the additional time-dependent results for the non-local equivalent strain and the damage, for cases D and E. The influence of an increased value of the internal length scale can be investigated by comparing cases D, A and E. It can be observed that with increasing internal length scale the damage decreases. This applies especially at quarter height and half height and considerably less at the quenched sample side. The aforementioned event time is roughly the same for all cases D, A and E. Most damage does not appear at the sample bottom but at higher locations in the sample, which is due to the stress distribution. At the sample bottom compressive stresses prevail due to restricted thermal expansion (due to less expansion at higher locations). Reversely, at higher locations tensile stresses can be found. The definition for the local equivalent strain, Eq. (2.9), entails a higher (elasticity-based) damage evolution in case of tensile loading. For the maximum applied internal length scale (case E) the averaging effect of non-locality is such that even at the bottom of the sample, damage growth nearly stops after 10 s just as for the higher locations.

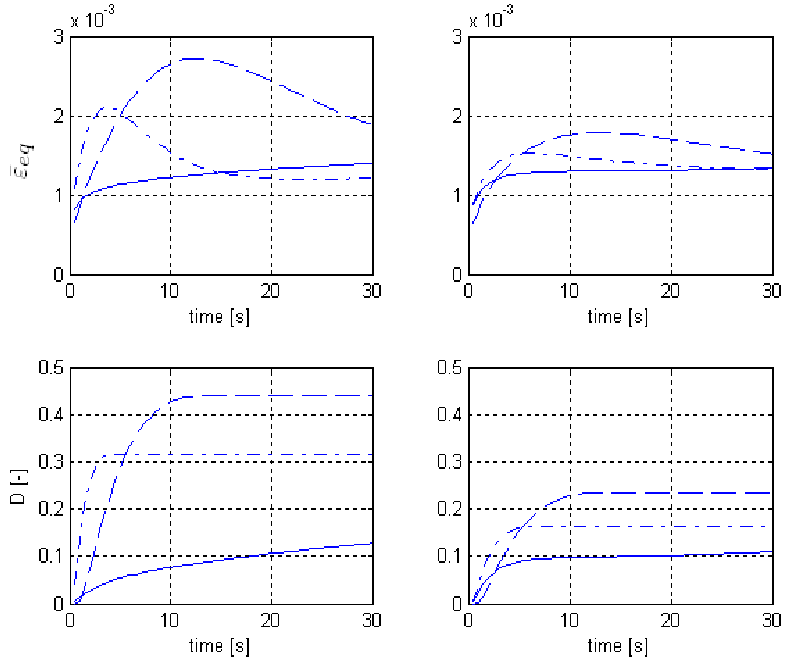

Fig. 2.5. Centerline non-local equivalent strain (upper row) and damage (lower row) as a function of time for the cases D and E (left to right). Solid line: sample bottom, dash-dot: quarter height, dashed: half height

2.6 Thermal shock experiments

The numerical model was used to simulate dedicated thermal shock experiments where refractory samples of ambient temperature were quenched in molten aluminium of 1000 °C. Damage in the samples was determined from sound measurements. Calculated damage is compared with experimental damage.

2.6.1 Set-up and experimental procedures

The left part of Fig. 2.6 shows a schematic view of the set-up and samples used. Solid aluminium was molten and heated to 1000 °C in an open induction furnace, powerful enough to maintain the temperature at a constant level. On top of the furnace a guiding system was mounted which enabled accurate and fast positioning of a sample in contact with the liquid aluminium bath. The sample is connected to the guiding system by a ceramic rod of low thermal conductivity. The sample temperature was measured with thermocouples located on its centerline at 10, 25 and 40 mm from the sample bottom. Samples without thermocouples were used for damage determination. Apart from the quenched side all other sides were thermally insulated. Terracoat ® was applied at the quenched side to prevent aluminium penetration into the sample. The heating period was 20 minutes after which the sample was exposed to ambient air.

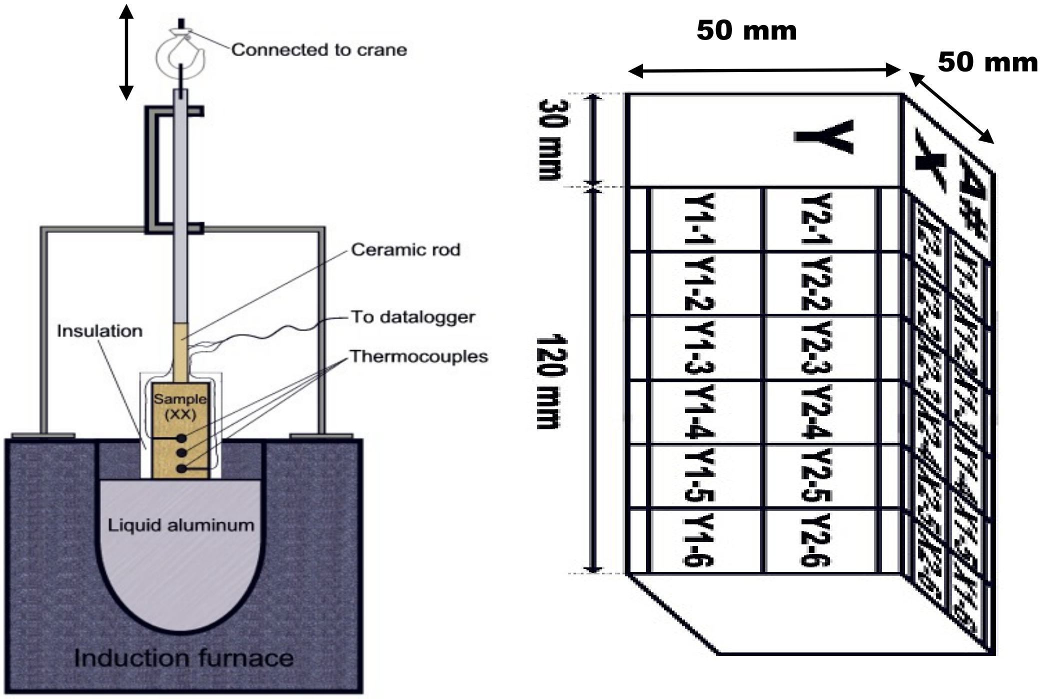
Connected to crane
Ceramic rod
To datalogger
Insulation
Thermocouples
Sample (XX)
Liquid aluminum
Induction furnace
50 mm
50 mm
30 mm
120 mm
Y
X
A#
Y1-1
Y1-2
Y1-3
Y1-4
Y1-5
Y1-6
Y2-1
Y2-2
Y2-3
Y2-4
Y2-5
Y2-6

Fig. 2.6. Schematic view of the set-up used in the thermal shock experiments (left) and sample with measurement grid, not to scale (right)

The sound velocity in the sample was determined before and after the experiment. The right part of Fig. 2.6 shows the measurement grid used. Transducers were positioned opposite to each other at 4 different locations e.g. at Y1-1, Y2-1, X2-1 and X1-1 for 6 positions on the longitudinal sample axis. For each position along the longitudinal axis results were averaged over these 4 locations. From the measured transit time of longitudinal sound waves and the mutual transducer distance the average sound velocity was calculated. Subsequently the dynamic Young's modulus E was calculated using Eq. (2.30) where V and v specify the sound velocity and Poisson's ratio, respectively. Damage causes an increase in transit time and thus a decrease in sound velocity and dynamic Young's modulus. The relative change of the latter is used to calculate the damage from Eq. (2.31), assuming that the sample density and Poisson's ratio are not affected by the damage.

$$E = \rho \left[\frac{(1+v)(1-2v)}{(1-v)} \right] V^2 \tag{2.30}$$

$$D = \frac{E_0 - E}{E_0} \tag{2.31}$$

2.6.2 Results of the experiments and modelling

Fig. 2.7 shows the experimentally determined damage obtained for 3 samples (denoted by A1, A2 and A3) and modeling results, to be discussed in the following. The damage measured is most severe near the quenched sample sides where temperature gradients are the highest.

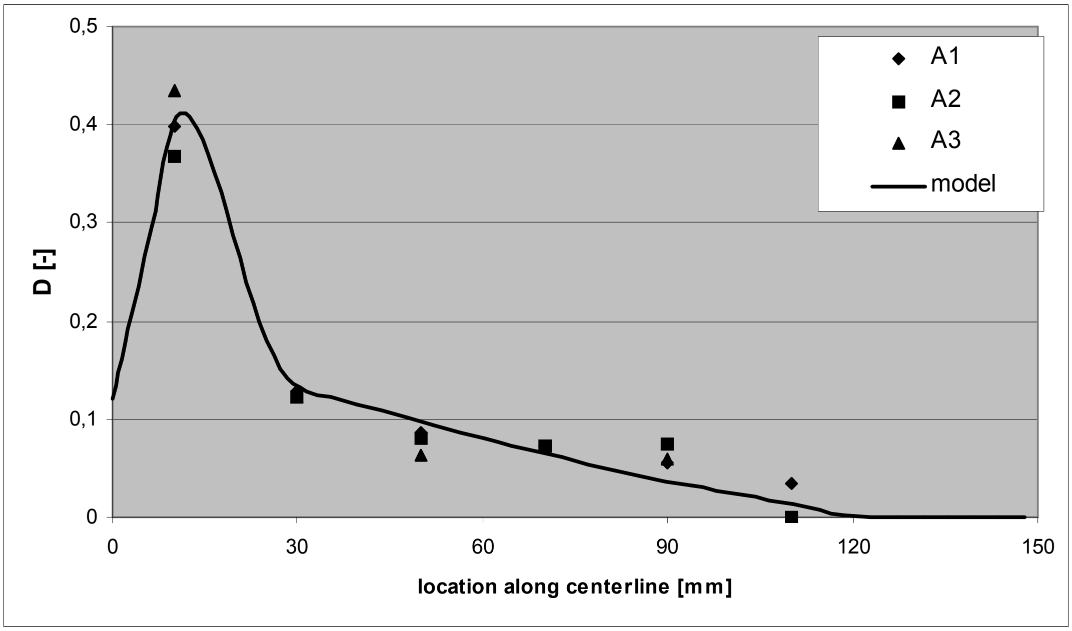

Fig. 2.7. Comparison between experimental and calculated damage

The thermal shock experiments were modeled with appropriate symmetry conditions for only a quarter of the sample (with dimensions: width x depth x height of 25 x 25 x 150 mm^3). The vertical displacement of the top centerline node is constrained consistent with the sample mounting. At the quenched sample side a temperature of 1000 °C is prescribed. The other sample sides are modeled as insulated. The heating period of 20 minutes was modeled using time steps of 3 seconds. The cooling period was not considered due to the relatively low heat transfer coefficient, which has been determined from the measured temperatures by inverse heat transfer modeling. A mesh density of 6 x 6 x 36 (width x depth x height) brick elements was used. The parameters identifying the material behaviour are presented in table 2.2. Some parameters are based on standard measurements in the temperature zone of interest, which are given as functions of the temperature θ expressed in [°C]. The Young's modulus and the damage threshold value for elasticity-based damage were determined from 3-point bending tests. The coefficient of thermal expansion was determined from dilatation measurements. The thermal conductivity and capacity were determined with standard measurements. The ratio of compressive and tensile strength (parameter η in Eq. (2.9)) was determined from uni-axial compressive tests and 3-point bending tests for different temperature levels. The value of Poisson's ratio used, 0.22, was estimated from typical values for refractory materials. Given the average material grain size of about 3 mm a value of the internal length scale parameter l_c equal to 3 mm was used. To ensure that the calculated damage at the sample bottom agreed with the trend in the corresponding experimental damage, a value of the thermal shock constant c_{ths} of 5*10^{-12} m^{2}K^{-1} was used. The damage parameters (α, β, $\kappa_{th,i}$, φ, $\kappa_{th,c}$) are estimated by fitting the numerical and experimental results.

Type	Quantity	Value	Unit	Source
Elastic material parameters	Young's modulus	$E(\theta)=-0.09710\theta^4+86.188\theta^3+\dots$ $\dots+4929.1\theta^2-1\cdot10^{-6}\theta+1\cdot10^{10}$	Pa	Measured
	Poisson's ratio	$v=0.22$	[-]	Estimate
Thermo-elastic material parameters	Thermal expansion	$\alpha_{th}=5.8\cdot10^{-6}$	K^{-1}	Measured
Thermal material parameters	Density	$\rho=2220$	kg m^{-3}	
	Conductivity	$\lambda(\theta)=1.979+0.0008\,\theta+6\cdot10^{-7}\,\theta^2$	W m^{-1} K^{-1}	
	Capacity	$C_p(\theta)=782+0.3\theta+0.0003\theta^2$	J kg^{-1} K^{-1}	
Equivalent strain parameter	Comp./tens. strength	$\eta(\theta)=3\cdot10^{-6}\,\theta^2-0.0001\theta+2.9973$	[-]	
Non-local material parameters	Length scale	$l_c=3$	mm	Estimate
	Thermal shock constant	$c_{ths}=5\cdot10^{-12}$	m^2 K^{-1}	Fitting result
Elasticity-based damage parameters	Damage threshold value	$\kappa_{el,i}(\theta)=0.0008-8\cdot10^{-8}\,\theta+1\cdot10^{-10}\,\theta^2$	[-]	Measured
	Damage evolution parameters	$\alpha=-1.25$	[-]	Fitting result
		$\beta=1250$	[-]	
Thermal damage parameters	Damage threshold value	$\kappa_{th,i}=50$	°C	
	Damage evolution parameters	$\varphi=0.3184$	[-]	
		$\kappa_{th,c}=19000$	°C	

Table 2.2. Parameters used in the modeling of the thermal shock experiments

Fig. 2.8 shows the evolution of the centerline temperature rate and non-local equivalent strain. Fig. 2.9 shows the evolution of the centerline temperature and total damage. Fig. 2.8 illustrates that, compared to the maximum values of the temperature rate, the maximum values of the corresponding non-local equivalent strain are shifted to a somewhat higher location in the sample. The evolution of the temperature rate and non-local equivalent strain indicate that the elasticity-based damage is concentrated in the lowest two centimeters of the sample. This is confirmed by the comparison of the evolution of the (maximum) temperature (the driving variable for thermal damage) and the damage (Fig. 2.9). At higher positions in the sample only thermal damage is present. Its evolution stops when the sample temperature reaches 50 °C after 20 minutes, at 0.12 m.

Fig. 2.7 demonstrates that experiments and calculations compare well; also experimental results point towards the presence of elasticity-based damage in the lowest two centimeters of the sample. The parameters α and β used are normally temperature-independent. For refractory materials, however, these parameters are likely to be temperature-dependent as they affect the post-elastic temperature-dependent stress-strain behaviour, see e.g. Fig. 2.1 and Eq. (2.3). This implies that the parameter values identified here should be regarded as a first attempt to establish the phenomenological relevance of the model. Their uniqueness cannot be proven. The temperature-dependent nature of α and β can be determined from e.g. uni-axial compression and bending tests performed at the temperatures of interest [33], [34], [37], [38]. The parameters governing the thermal damage evolution can be obtained from furnace experiments where samples are heated quasi-stationary to ensure a spatially uniform temperature. The difference between the measured initial and residual properties determines the thermal damage, which can be used to e.g. calculate the parameters in Eq. (2.7). The intrinsic length scale parameter l_c and thermal shock constant c_{ths} are a.o. dependent on the dimensions of the micro-structure. If the parameters of the damage evolution laws are known, l_c and c_{ths} can be determined from dedicated experiments reflecting this size-dependent nature of damage [44].

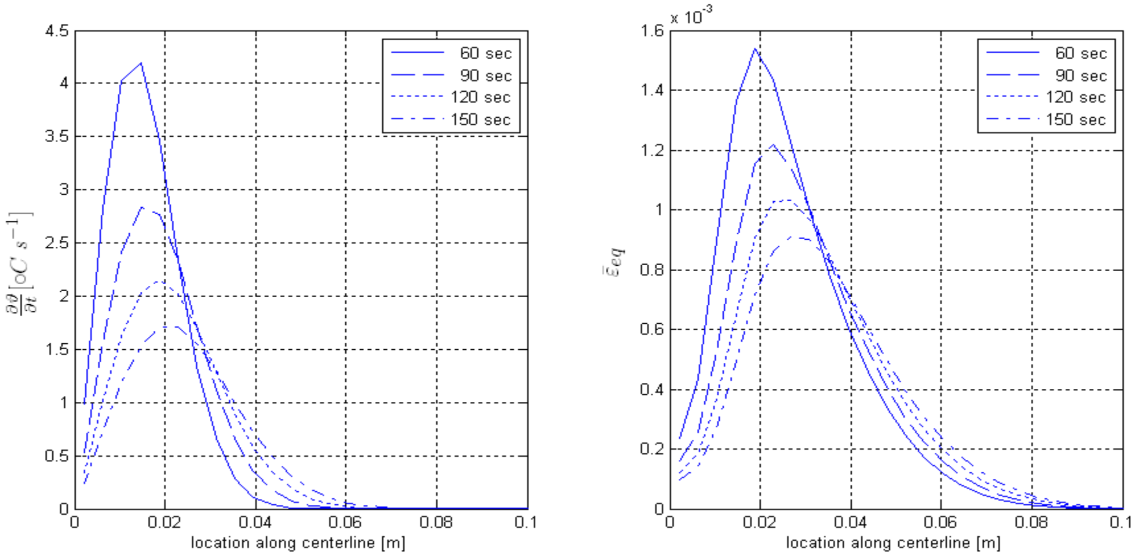

Fig. 2.8. Temperature rate (left) and non-local equivalent strain (right) along the centerline

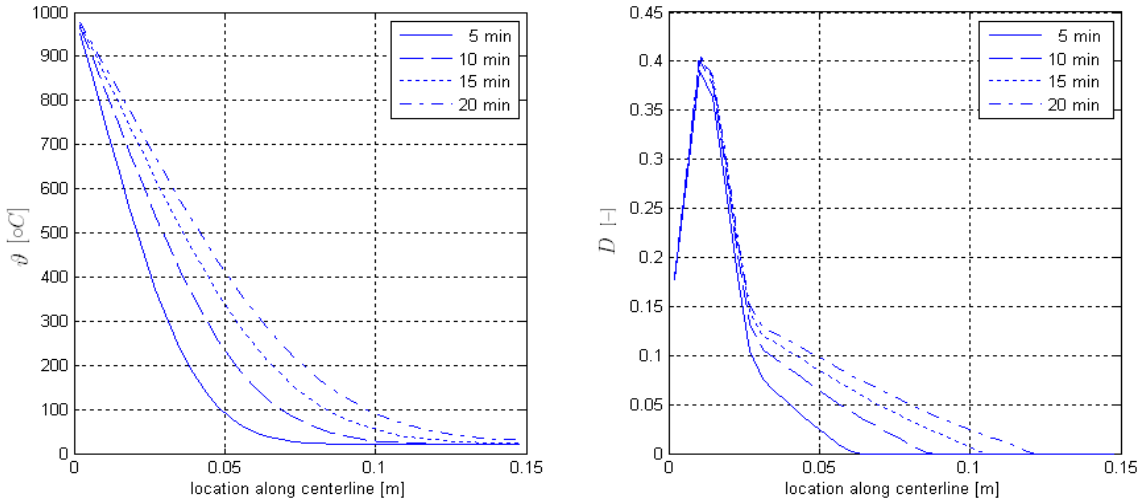

Fig. 2.9. Temperature (left) and damage (right) along the centerline

2.7 Conclusions

The principal causes of premature failure of refractory materials in installations for iron- and steelmaking are fatal thermal stresses induced by high transient temperature gradients, a phenomenon also known as thermal shock. In coarse-grained refractory material this initially leads to diffuse micro-cracking and can be followed by localization to macro-cracks pending on the load severity.

To capture the post-elastic transient thermo-mechanical behaviour of refractory materials a modeling framework has been developed based on continuum damage mechanics. To describe thermal shock damage a single scalar variable is used affecting the temperature-dependent Young's modulus with contributions from two distinct damage mechanisms. The first damage mechanism (elasticity-based damage) is induced by elastic strains stemming from temperature gradients causing internally and externally constrained thermal expansion. The second damage mechanism (thermal damage) is driven by uniform temperature change. This causes isotropic thermal expansion which can induce damage (e.g. micro-cracks) in case thermal expansion mismatches exist between the various constituents (e.g. grains, matrix). This structural phenomenon might be amplified by e.g. phase transitions in certain material components resulting in a permanent degradation of Young's modulus.

Compared to previous work the modeling framework presented in this paper comprises the following new aspects,

- The elasticity-based and thermal damage are combined in an additive way, driven by the assumption that both damage mechanism act independently on different scales.
- The driving variable for elasticity-based damage, the non-local equivalent strain, obtained via a gradient enhanced implicit formulation, is extended with a term accounting for micro-structural strain gradients induced by transient temperature gradients.
- Within the definition used for the local equivalent strain (modified Von Mises) a temperature-dependent ratio of compressive and tensile strength is incorporated. Other parameters in the framework proposed for elasticity-based damage also reflect the distinct temperature-dependent mechanical behaviour of refractory material.
- For thermal damage a new evolution law is proposed enabling progressive as well as degressive evolution with the attained maximum temperature.
- The equations for transient thermal transport, equilibrium and extended (transient) non-locality and are solved simultaneously in a finite element environment using a backward-Euler time integration scheme and full Newton-Raphson linearization. Temperature-dependent elastic and

> thermal moduli are used where appropriate. The transient evolution of non-local damage combined with temperature-dependent parameters has not been described before elsewhere.

The influence of non-locality and its (micro-structural strain gradient) extension has been investigated in a parameter study within a plane strain context. Due to the averaging effect of a non-local formulation, damage decreased and became less localized for an increasing internal length scale (reflecting the coarseness of refractory material). This did not influence the time at which the maximum equivalent strain, the source term for the actual elasticity-based damage, reached maximum values. Increase in the micro-structural strain gradient contribution was apparent through extra damage at the thermally shocked edge, despite the compressive stress state at that location.

The phenomenological relevance of the numerical framework was established through a model of a dedicated thermal shock experiment where ambient refractory samples have been brought in contact with molten aluminium. The temperature-dependent thermal and elastic material properties used were obtained from standard measurements. The values of the parameters governing the evolution of elasticity-based and thermal damage were identified from the obtained experimental results showing an adequate agreement. Elasticity-based damage was present in the immediate vicinity of the quenched sample side while in the remainder of the material thermal damage could be observed. Differences between model and experiments might be reduced by using temperature-dependent damage evolution parameters reflecting the temperature-dependent (post-elastic) constitutive behaviour. The determination of such parameters with dedicated tests will be part of future work.

2.8 References

[1] D.P.H. Hasselman, *Thermal stress resistance parameters for brittle refractory ceramics: a compendium,* Ceramic Bulletin, 1970, Vol. 49, pp. 1033-1037

[2] D.P.H. Hasselman, *Figures-of-merit for the thermal stress resistance of high-temperature brittle materials : a review,* Ceramurgia International, 1978, Vol. 4, pp. 147-150

[3] D.P.H. Hasselman, *Unified theory of thermal shock fracture initiation and crack propagation in brittle ceramics,* J. Am. Cer. Soc., 1969, Vol. 52, pp. 600-604

[4] T.J. Lu and N.A. Fleck, *The thermal shock resistance of solids,* Acta Metall. Mater. 1998, Vol. 46, pp. 4744-4768

[5] H.A. Bahr, H. Balke, M. Kuna, H. Lieske, *Fracture analysis of a single edged cracked strip under thermal shock,* Theoretical and applied fracture mechanics, 1987, Vol. 8, pp. 33-39

[6] H.A. Bahr, T. Fett, I. Hahn, D. Munz, I. Pflugbeil, *Fracture mechanics treatment of thermal shock and the effect of bridging stresses,* Thermal shock and thermal fatigue behaviour of advanced ceramics, Kluwer Academic Publishers, pp. 105-117, 1993

[7] X.R. Wu, *Application of weight function method for crack analysis in thermal stress fields,* Thermal shock and thermal fatigue behaviour of advanced ceramics, Kluwer Academic Publishers, pp. 119-141, 1993

[8] B. Cotterel, W.O. Sze, Q. Caidong, *Thermal shock and size effects in castable refractories,* J. Am. Ceram. Soc., 1995, Vol. 78, pp. 2056-2064

[9] Z.H. Jin, Y.W. Mai, *Effects of damage on thermal shock strength behavior of ceramics,* J. Am. Ceram. Soc. Vol. 78, 1995, pp. 1873-1881

[10] Z.H. Jin, R.C. Batra, *Thermal shock cracking in a metal-particle-reinforced ceramic matrix composite,* Engineering Fracture Mechanics, 1999, Vol. 62, pp. 339-350

[11] W.O. Soboyejo, C. Mercer, *Investigation of thermal shock in a high-temperature refractory ceramic: a fracture mechanics approach,* J. Am. Cer. Soc. , 2001, Vol. 84, pp.1309-1314

[12]. D. Rubesa, *Thermal stress fracture and spalling of well blocks in steel ladles – modeling and numerical simulation,* Veitsch-Radex Rundschau, 1999, Vol. 2, pp. 3-24

[13] F. Bradley, A.C.D. Chaklader, A. Mitchell, *Thermal stress fracture of refractory lining components: Part 1. Thermo-elastic analysis,* Metallurgical Transactions, 1987, Vol. 18B, pp. 355-363

[14] J. Knauder, R. Rathner, *Thermo-mechanical analysis of basic refractories*, Radex-Rundschau, 1990, Heft 4

[15] J.P. Schneider, B. Coste, *Thermo-mechanical modeling of thermal shock in anodes,* Conf. Proceedings, Light Metals 1993, The Minerals, Metals & Materials Society

[16] A. Keisuke, *Evaluation of thermal stress in refractory bricks by the finite element method,* Taikabutsu Overseas, 1989, Vol. 10, No. 4

[17] J. Knauder, R. Rathner, *Improved design of a BOF-lining based on thermo-mechanical analysis,* Radex-Rundschau, 1990, Heft 1

[18] R. Rathner, *Lining design and behavior of BOF's,* Radex-Rundschau, 1990, Heft 4

[19] K. Andreev, H. Harmuth, *Application of finite element modeling to the thermo-mechanical behaviour of refractories,* Finite Elements in Civil Engineering Applications, Hendriks & Rots (eds.), Swets & Zeitlinger, 2002

[20] K. Andreev, H. Harmuth, *FEM simulation of the thermo-mechanical behavior and failure of refractories-a Case study,* J. of Mat. Proc. Techn., 2003, Vol. 143-144, pp. 72-77

[21] M.A.J. van Gils, L.J.M.G. Dortmans and G. de With, *Thermal shock predictions for refractory ceramics,* Proceedings of the Second International Symposium on Thermal Stresses and Related Topics, June 8-11 1997, Rochester Institute of Technology, pp. 682-697, Eds.: R.B. Hetnarski, N. Noda, H. Ghoneim, 1997

[22] N. Schmitt, A. Burr, Y. Berthaud, J. Poirier, *Micro mechanics applied to the thermal shock behavior of refractory ceramics,* Mechanics of Materials, 2002, Vol. 34, pp. 725-747

[23] A. Gasser, K. Terny-Rebeyrotte, P. Boisse, J. Poirier, *A multi-scale approach for refractory structure modeling,* Proceedings of the Unified International Technical Conference on Refractories, Nov. 8-11 2005, The Am. Cer. Soc., pp. 998-1002, Ed. J.D. Smith, 2005

[24] F. Simonin, C. Olagnon, S. Maximilien, G. Fantozzi, L.A. Diaz, R. Torrecillas, *Thermo-mechanical behaviour of high-alumina refractory castables with synthetic spinel additions,* J. Am. Cer. Soc., 2000, Vol. 83, pp. 2481-2490

[25] C. Aksel, B. Rand, F.L. Riley, P.D. Warren, *Thermal shock behaviour of magnesia-spinel composites,* J. Eur. Cer. Soc., 2004, Vol. 24, pp. 2839-2845

[26] C. Aksel, P.D. Warren, F.L. Riley, *Fracture behaviour of magnesia and magnesia-spinel composites before and after thermal shock,* J. Eur. Cer. Soc., 2004, Vol. 24, pp. 2407-2416

[27] M. Boussuge, *Some numerical approaches of creep, thermal shock, damage and delayed failure of ceramics and refractories,* Bull. Mater. Sci., 2001, Vol. 24, pp. 97-100

[28] M. Boussuge, *Thermo-mechanical behaviour: from ceramics to refractories,* Advances in refractories for the metallurgical industries IV, 43rd Annual Conference of Metallurgists of CIM, Eds. M. Rigaud, C. Allaire, 2004

[29] J.L. Chaboche, *Continuum damage mechanics: Part I – General concepts,* J. of Appl. Mech., 1988, Vol. 55, pp. 59-64

[30] W.L. Headrick, M. Karukus, X. Laing., *Refractory for black liquor gassifiers,* University of Missouri-Rolla, Rolla, MO 65409-1130, DOE Award Number: DE-FC26-02NT41491, 2005

[31] N. Prompt, E. Ouedraogo, T. Joly, P. Stutz, *Thermo-mechanical modeling of a refractory structure: the wear layer of a blast furnace trough,* Proceedings of the Unified International Technical Conference on Refractories, Nov. 4-7 2001, The Am. Cer. Soc., pp. 282-288, 2001

[32] X. Liang, W.L. Headrick, L.R. Dharani, S. Zhao, J. Wei, *Failure analysis of refractory cup under thermal loading and chemical attack using continuum damage mechanics,* Proceedings of the Unified International Technical Conference on Refractories, Nov. 8-11 2005, The Am. Cer. Soc., pp. 980-984, Ed. J.D. Smith, 2005

[33] W. Nentech, F. Meftah, J.M. Reynouard, *An elasto-plastic damage model for plain concrete subjected to high temperatures*, Engineering Structures, 2002, Vol. 24, pp. 597-611

[34] B.M. Luccioni, M.I. Figueroa, R.F. Danesi, *Thermo-mechanic model for concrete exposed to elevated temperatures*, Engineering Structures, 2003, Vol. 25, pp. 729-742

[35] D. Gawin, C.E. Majorana, B.A. Schrefler, *Numerical analysis of hygro-thermal behaviour and damage of concrete at high temperature,* Mech. of Coh.-Frict. Mat., 1999, Vol. 4, pp. 37-44

[36] J. Stabler, G. Baker, *On the form of free energy and specific heat in coupled thermo-elasticity with isotropic damage,* Int. J. of Sol. and Struct., 2000, Vol. 37, pp. 4691-4713

[37] J. Stabler, G. Baker, *Fractional step methods for thermo-mechanical damage analyses at transient elevated temperatures,* Int. J. for Num. Meth. in Eng., 2000, Vol. 48, pp. 761-785

[38] C.J. Pearce, C.V. Nielsen, N. Bicanic, *Gradient-enhanced thermo-mechanical damage for concrete at high temperatures including transient thermal creep*, Int. J. for Num. and Anal. Methods in Geom., 2004, Vol. 28, pp. 715-735

[39] R.H.J. Peerlings, R. de Borst, W.A.M. Brekelmans, J.H.P. de Vree, *Gradient enhanced damage for quasi-brittle materials,* Int. J. for Num. Meth. in Eng., 1996, Vol. 39, pp. 3391-3403

[40] R.H.J. Peerlings, R. de Borst, W.A.M. Brekelmans, M.G.D. Geers, *Gradient-enhanced damage modeling of concrete fracture,* Mech. of Coh.-Frict. mat., 1998, Vol. 3, pp. 321-342

[41] C. Aksel, *Mechanical Properties and Thermal Shock Behaviour of Alumina-mullite-zirconia and Alumina-mullite Refractory Materials by Slip Casting*. Ceramics International, 2003, Vol. 29, pp. 311-316

[42] K. Andreev, H. Harmuth, *Modeling of the thermo-mechanical behaviour of the lining materials of teeming ladles,* Proceedings of the Unified International Technical Conference on Refractories, Nov. 4-7 2001, pp. 830-840, 2001

[43] R.H.J. Peerlings, *Enhanced damage modeling for fracture and fatigue,* PhD Thesis, Eindhoven University of Technology, 1999

[44] M.G.D. Geers, R. de Borst, W.A.M Brekelmans, R.H.J. Peerlings, *Strain-based transient-gradient damage model for failure analyses,* Comput. Methods Appl. Mech. Eng., 1998, Vol. 160, pp. 133-153

2.9 Linear system of equations

The linear system of equations to be solved within the numerical modeling framework presented in this paper (Eq. 2.26) reads:

$$\underline{K}_{i-1}\delta\underset{\sim}{a} = \underset{\sim}{f}_{ext} - \underset{\sim}{f}_{int,i-1} \tag{2.32}$$

with the following components

$$\underline{K}_{i-1} = \begin{bmatrix} \underline{K}^{\theta\theta}_{i-1} & \underline{K}^{\theta u}_{i-1} & \underline{K}^{\theta e}_{i-1} \\ \underline{K}^{u\theta}_{i-1} & \underline{K}^{uu}_{i-1} & \underline{K}^{ue}_{i-1} \\ \underline{K}^{e\theta}_{i-1} & \underline{K}^{eu}_{i-1} & \underline{K}^{ee}_{i-1} \end{bmatrix},\ \delta\underset{\sim}{a} = \begin{bmatrix} \delta\underset{\sim}{\theta} \\ \delta\underset{\sim}{u} \\ \delta\underset{\sim}{\varepsilon}_{eq} \end{bmatrix},\ \underset{\sim}{f}_{ext} = \begin{bmatrix} \underset{\sim}{f}^{\theta}_{ext} \\ \underset{\sim}{f}^{u}_{ext} \\ \underset{\sim}{f}^{e}_{ext} \end{bmatrix},\ \underset{\sim}{f}_{int,i-1} = \begin{bmatrix} \underset{\sim}{f}^{\theta}_{int,i-1} \\ \underset{\sim}{f}^{u}_{int,i-1} \\ \underset{\sim}{f}^{e}_{int,i-1} \end{bmatrix} \tag{2.33}$$

The sub-matrices of the global system matrix $\underline{K}_{i-1}$ are presented below in row-wise order.

Row 1

$$\underline{K}^{\theta\theta}_{i-1} = \underline{L}_{1,i-1} + \underline{L}_{2,i-1} + \underline{L}_{3,i-1} + \underline{L}_{4,i-1} \tag{2.34}$$

where the abbreviations $\underline{L}_{1,i-1}$, $\underline{L}_{2,i-1}$, $\underline{L}_{3,i-1}$ and $\underline{L}_{4,i-1}$ denote

$$\underline{L}_{1,i-1} = \int_{\Omega} \underline{N}_{\theta}^{T} \rho \left(\frac{\partial C_p}{\partial \theta}\right)_{i-1} \left(\underline{N}_{\theta} \frac{\underset{\sim}{\theta}_{i-1} - \underset{\sim}{\theta}_{n}}{\Delta t}\right) \underline{N}_{\theta} d\Omega$$

$$\underline{L}_{2,i-1} = \int_{\Omega} \underline{N}_{\theta}^{T} \rho C_{p_{i-1}} \underline{N}_{\theta} d\Omega \, \frac{1}{\Delta t}$$

$$\underline{L}_{3,i-1} = \int_{\Omega} \underline{B}_{\theta}^{T} \left(\frac{\partial \lambda}{\partial \theta}\right)_{i-1} \underline{B}_{\theta} \, \underset{\sim}{\theta}_{i-1} \, \underline{N}_{\theta} d\Omega$$

$$\underline{L}_{4,i-1} = \int_{\Omega} \underline{B}_{\theta}^{T} \lambda_{i-1} \underline{B}_{\theta} \, d\Omega$$

$$\underline{K}_{i-1}^{\theta u} = \underline{K}_{i-1}^{\theta e} = \underline{0} \tag{2.35}$$

Row 2

$$\underline{K}_{i-1}^{u\theta} = \underline{S}_{1,i-1} + \underline{S}_{2,i-1} + \underline{S}_{3,i-1} \tag{2.36}$$

where the abbreviations $\underline{S}_{1,i-1}$, $\underline{S}_{2,i-1}$ and $\underline{S}_{3,i-1}$ denote

$$\underline{S}_{1,i-1} = -\int_{\Omega} \underline{B}_{u}^{T} \left[\begin{array}{l} R(d_{el}, \kappa_{el}, \bar{\varepsilon}_{eq}) + R(d_{el}, \kappa_{el,i}, \theta) + R(d_{el}, \alpha, \theta) + \ldots \\ \ldots + R(d_{el}, \beta, \theta) + R(d_{th}, \kappa_{th}, \theta) \end{array} \right] \underline{C}_{i-1} \underset{\sim}{\varepsilon}_{el,i-1} \, d\Omega$$

$$\underline{S}_{2,i-1} = \int_{\Omega} \underline{B}_{u}^{T} \left(1 - d_{el,i-1} - d_{th,i-1}\right) \left(\frac{\partial \underline{C}}{\partial E}\right)_{i-1} \left(\frac{\partial E}{\partial \theta}\right)_{i-1} \underset{\sim}{\varepsilon}_{el,i-1} \, \underline{N}_{\theta} d\Omega$$

$$\underline{S}_{3,i-1} = -\int_{\Omega} \underline{B}_{u}^{T} \left(1 - d_{ths,i-1} - d_{th,i-1}\right) \underline{C}_{i-1} \underline{N}_{\theta} d\Omega$$

In the expression for $\underline{S}_{1,i-1}$, in the above, the abbreviation $R(F,G,H)$ has been used for clarity such that e.g.

$$R(F,G,H) = \left(\frac{\partial F}{\partial G}\right)_{i-1} \left(\frac{\partial G}{\partial H}\right)_{i-1} \underline{N}_{H}$$

$$\underline{K}_{i-1}^{uu} = \int_{\Omega} \underline{B}_{u}^{T} \left(1 - d_{th,i-1} - d_{el,i-1}\right) \underline{C}_{i-1} \underline{B}_{u} d\Omega \tag{2.37}$$

$$\underline{K}^{ue}_{i-1} = -\int_{\Omega} \underline{B}_u^T \left(\frac{\partial d_{el}}{\partial \kappa_{el}}\right)_{i-1} \left(\frac{\partial \kappa_{el}}{\partial \bar{\underset{\sim}{\varepsilon}}_{eq}}\right)_{i-1} \underline{C}_{i-1}\, \underset{\sim}{\varepsilon}_{el,i-1}\, \underline{N}_e d\Omega \tag{2.38}$$

Row 3

$$\underline{K}^{e\theta}_{i-1} = \int_{\Omega} \underline{N}_e^T \left(\left(\frac{\partial \varepsilon_{eq}}{\partial \underset{\sim}{\varepsilon}_{el}}\right)^T_{i-1} \underset{\sim}{m} - \left(\frac{\partial \varepsilon_{eq}}{\partial \eta}\right)_{i-1} \left(\frac{\partial \eta}{\partial \theta}\right)_{i-1} - \left(\frac{\partial C_{ths}}{\partial \theta}\right)_{i-1} \underline{N}_{\theta} \left| \frac{\underset{\sim}{\theta}_{i-1} - \underset{\sim}{\theta}_{n}}{\Delta t} \right| \right) \underline{N}_{\theta}\, d\Omega \tag{2.39}$$

$$\underline{K}^{eu}_{i-1} = -\int_{\Omega} \underline{N}_e^T \left(\frac{\partial \varepsilon_{eq}}{\partial \underset{\sim}{\varepsilon}_{el}}\right)^T_{i-1} \underline{B}_u d\Omega \tag{2.40}$$

$$\underline{K}^{ee}_{i-1} = \int_{\Omega} \left(\underline{N}_e^T \underline{N}_e + \underline{B}_e{}^T l_c^2 \underline{B}_e \right) d\Omega \tag{2.41}$$

3. Experimental analysis of the evolution of thermal shock damage using transit time measurement of ultrasonic waves

Thermal shock is a principal cause of catastrophic wear of the refractory lining of high temperature installations in metal making processes. To investigate thermal shock experimentally with realistic and reproducible heat transfer conditions, chamotte and corund refractory samples of ambient temperature were subjected to surface contact with molten aluminium followed by passive cooling in ambient air. The evolution of damage was characterized by measuring the transit time of ultrasonic longitudinal waves at various sample locations after each test cycle. The mechanical validity of transit time measurement was confirmed in independent experiments. The single test cycle performed with chamotte material indicated the reproducibility and reliability of the experimental set-up and damage characterization method. Multiple test cycles performed with corund material yielded a reliable set of data, to be used for model validation purposes. Both non-uniform damage due to temperature gradients as well as uniform damage due to exposure to a uniform temperature were determined experimentally. The interaction between both damage mechanisms requires further investigation as well as the possible shielding of heat transport by damage.

3.1 Introduction

The refractory lining of iron and steelmaking installations is prone to wear as the result of excessive thermal stresses. This wear process occurs for example when molten steel is introduced into a cold ladle. Another example of this so-called thermal shock event is the sudden opening of an operating furnace where the hot refractory material becomes exposed to ambient air.

Experimental investigations into thermal shock behaviour of refractory materials are reported extensively in the literature. Severe down-quenching was achieved using water [1-13], oil [14-17] and molten salt [18]. Milder down-quenching was realized using passive or active cooling by ambient air mostly preceded by mild up-quenching in a hot furnace atmosphere [19-24]. Also fluidized beds with ambient air were used for this purpose [25]. Severe up-quenching was achieved using burners [26-29], molten metal [30-32], lasers

Reproduced from: F. Damhof, W.A.M. Brekelmans, M.G.D. Geers., *Experimental analysis of the evolution of thermal shock damage using transit time measurement of ultrasonic waves*,
J. Eur. Cer. Soc., 2009, Vol. 20, pp. 1159-1167

[33-35] and film heaters [36]. For this purpose also electrical induction [37], resistance [38] and discharge [39] have been used on refractories containing carbon. Milder up-quenching was achieved using a hot furnace atmosphere [40-43], infrared heaters [44] and hot compressed gas [45]. Due to the poor reproducibility of the heat transfer conditions most of the aforementioned test methods do not qualify for the use in a model parameter estimation process. A down-quenched sample in water is e.g. surrounded by boiling water affecting the heat transfer. Lasers do provide a constant heat flux but only over a very small sample surface, not suitable for refractory material with coarse grains. Furthermore, the use of molten salts can lead to chemical corrosion. The up-quench achieved with a hot furnace atmosphere is of low severity and not representative for thermal shock in the refractories of interest here under realistic process conditions. Although up-quenching with burners does represent the heating of a process furnace, the heat flux generated is not constant over the sample surface.

Experimental characterization of thermal shock damage has been performed e.g. by (microscopic) examination of the crack pattern [18, 28, 31, 33, 34, 35, 45], recording the number of test cycles or the quenching temperature difference to reach material failure [1, 2, 32], by determination of the residual mechanical properties [1, 3, 4, 5, 8, 9, 10, 25, 36, 37, 38, 39, 42] and of the weight loss after layer-wise spalling [43]. Other characterization techniques rely on the measurement of acoustic emission during thermal shock [11, 22, 24, 26, 44, 46, 47] and the determination of the change in sound velocity [40, 48, 49], attenuation [48] and resonance frequency [6, 16, 20, 29] due to thermal shock. The described methods characterize the material state of an entire test sample and thus only allow for a qualitative ranking of materials. Apart from laborious and expensive techniques as X-ray and ultrasonic tomography [50-52], the location-dependent characterization of damage evolution in coarse granular materials has not been reported yet.

Thermal shock initially induces micro-cracks, localizing to macro-cracks, depending on the load severity and repetition. To predict this thermo-mechanical behaviour a phenomenological constitutive model has been developed [53] based on Hooke's law for damaged isotropic material [54]:

$$\boldsymbol{\sigma} = (1 - D)\,{}^{4}\boldsymbol{C} : \boldsymbol{\varepsilon}_{el} \tag{3.1}$$

with $\boldsymbol{\sigma}$ the stress tensor, D a scalar variable representing the damage ranging from zero to unity (loss of structural integrity), ${}^{4}\boldsymbol{C}$ the fourth order elasticity tensor of the undamaged material and $\boldsymbol{\varepsilon}_{el}$ the elastic strain tensor, which is here induced by a constrained thermal expansion. The damage D includes both non-uniform and uniform damage. Thermal shock leads to temperature gradients, non-uniform thermal expansion and non-uniform damage. A uniform temperature increase induces uniform thermal expansion in mechanically unconstrained configurations. This may lead to uniform damage due to micro-scale thermal expansion mismatches within the microstructure of the material [55-57].

Damage development is described by evolution laws, involving material-dependent parameters. These have to be determined from standard tests and dedicated experiments reflecting the thermal shock damage process under consideration with representative and reproducible boundary conditions. Model parameter estimation requires furthermore the quantification of the evolution of damage at various locations in a test sample.

In this paper an experimental set-up is proposed allowing the triggering of a thermal shock with reproducible heat transfer conditions such that realistic process conditions are adequately represented. The damage evolution in a test sample, using consecutive test cycles, is characterized by measuring the transit time of ultrasonic longitudinal waves at various locations. The discussion starts with the specification of the test materials used and selected experimental details on the method of damage characterization. Thereafter quasi-stationary heating and cooling experiments are described to introduce the phenomenon of uniform thermal damage experimentally. In order to establish the mechanical validity of the damage characterization method a comparison is made between the residual mechanical and the corresponding acoustic damage properties after water quench experiments. The thermal shock experiments discussed subsequently entail the surface contact of ambient refractory samples with molten aluminium followed by cooling in ambient air. To simulate the one-dimensional temperature profile of thick-walled refractory linings of high temperature installations, thermal insulation is applied at the non-quenched sample sides. Reproducible damage evolution was measured in two different types of refractory material and a representative set of data was obtained, useful for future model validation purposes.

3.2 Materials

Chamotte and corund refractory materials have been used in the experiments presented in this paper. Chamotte material is typically applied in the shaft of a blast furnace suitable for the production of raw iron and in iron and steel ladles. corund material is typically used in the hearth of a blast furnace, in re-heating furnaces of a hot strip mill plant and in reactor vessels used in the petro-chemical industry. The test materials have been selected for their known sensitivity to thermal shock. Samples were cut to size from commercially available refractory bricks. The chamotte bricks, based on a combination of calcined clays (chamotte) and raw clays, received their final properties after pressing and drying during a sintering stage of 15 hours in a tunnel kiln heated to a temperature of 1400-1450 ºC. The corund bricks, based on corundum and mullite, received their final properties after pressing and drying during a sintering stage of 3 to 5 hours in a tunnel kiln heated to a temperature of 1500-1600 ºC. The chemical composition of both materials is presented in Table 3.1. The main properties at room temperature are presented in Table 3.2, as well as characteristics reflecting the material structure.

Rel. weight of components [%]	**chamotte**	**corund**
Al_2O_3	58.7	90.9
SiO_2	40.0	8.8
Na_2O	-	0.2
Fe_2O	1.1	-

Table 3.1. Chemical composition of the test materials

Property	**Symbol**	**Unit [-]**	**chamotte**	**corund**
Density	ρ	kg m^{-3}	2220	3038
Porosity	ϕ	%	18.2	17.0
Young's modulus	E	GPa	10.0	13.0
Poisson's ratio	ν	[-]	0.22	0.22
Bending strength	σ_b	MPa	9.0	8.7
Compressive strength	σ_c	MPa	27.8	68.9
Thermal expansion	α	K^{-1}	$6*10^{-6}$	$8*10^{-6}$
Thermal conductivity	λ	W m^{-1} K^{-1}	2.0	3.7
Thermal capacity	C_p	J kg^{-1} K^{-1}	788	773
Maximum grain size	-	mm	3	4
Average grain size	-	mm	2	3

Table 3.2. Properties of the test materials

With the presented material properties the Hasselman parameter R for resistance against thermal shock fracture initiation [58] defined by:

$$R = \frac{\sigma_b(1-\nu)}{\alpha E} \tag{3.2}$$

can be determined. The parameter R represents the maximum allowable temperature increase in a material during infinitely fast heating-up. For the chamotte and corund sample materials this parameter values 117 °C and 65 °C respectively. The predicted allowable temperature increase is largely exceeded in the thermal shock tests discussed in this paper. This implies that considerable damage can be expected.

3.3 Damage characterization

The characterization of damage in the test samples is performed by measuring the transit time of ultrasonic longitudinal waves using a Pundit system from C.N.S. Farnell. The exciting and receiving transducers are located on the tests samples opposite to each other. Hence, the wave propagation direction is perpendicular to the transducer surfaces. The average longitudinal wave velocity V is determined as the ratio of the distance between the transducers and the transit time. Subsequently the dynamic Young's modulus E_{dyn} is calculated according to:

$$E_{dyn} = \rho\left[\frac{(1+\nu)(1-2\nu)}{(1-\nu)}\right]V^2 \tag{3.3}$$

Damage, as a result of micro-cracks induced by e.g. thermal shock, increases the wave transit time and consequently causes a reduction of E_{dyn}. The relative decrease of this dynamic modulus with respect to the initial (undamaged) state is defined in this paper as the damage D, unless mentioned otherwise. The density and Poisson's ratio are assumed to be only negligibly affected by damage.

In the experiments reported in this paper, transducers of 54 kHz (40 mm diameter) have been used for the larger samples and transducers of 200 kHz (20 mm diameter) have been used for the smaller samples and for location-dependent measurements. Similar results were obtained with both transducer types. For a typical refractory wave velocity of 3200 m/s wave lengths (calculated from the ratio of velocity and frequency) of 0.059 m and 0.016 m are thus generated, respectively. In the context of the maximum grain size of the refractory materials investigated, see Table 3.2, the spatial resolution is fully acceptable.

The acoustic contact between the transducers and the test samples is established by applying 1 mm thick self-adhering silicon rubber pads to the transducers. The registered transit time has to be corrected with that of the rubber pads which was determined in dedicated experiments. In the ‘sandwich experiments’ described hereafter contact gel was used to establish the acoustic contact between the samples and transducers but also between individual samples.

To investigate how non-uniform damage may affect the wave transit time the latter was measured over two ‘sandwiches’, composed of pairs of refractory samples: 1 and 2 in series as well as 3 and 4. Samples 1, 3 and 4 (height/transducer distance 30 mm) were of corund material. Sample 2 (height/transducer distance 50 mm) was of chamotte material. Contact gel was used for acoustic coupling with the 200 kHz transducers and between the individual sandwich components. It is assumed here that the contact gel neither penetrated the sample surfaces nor affected the transit time. The transit time was measured of both the sandwiches and their individual components. Subsequently all the relevant material surfaces were polished (using 120 diamond followed by 1200 diamond disks) and the measurement was repeated.

Table 3.3 presents the results of the sandwich experiments. It can be observed that the transit times of the polished sandwiches are equal to the summed transit times of their individual components. The difference of 0.4 μs appearing when dealing with the unpolished samples is ascribed to the roughness of the relevant sample surfaces. These results indicate furthermore that in case of non-uniform damage, the measured transit time equals the summed transit time of the various damaged material zones present between the transducers.

Polishing of the samples lowers the transit time with 1-3 % and 2 % for the measurements with 30 mm and 50 mm transducer distance, respectively. Given these low percentages and the common scattering in material properties of coarse grained refractory materials, the effect of surface roughness will be neglected in the rest of this paper.

	Unpolished		**Polished**	
Sample no.	**Transit time (μs)**	**Height (mm)**	**Transit time (μs)**	**Height (mm)**
1	9.5	30.34	9.4	30.01
2	15.7	50.03	15.4	49.71
1+2 individual	25.2	80.37	24.8	79.72
1+2 sandwich	25.6	80.37	24.8	79.72
3	6.3	30.31	6.1	29.85
4	6.7	30.36	6.5	29.92
3+4 individual	13.0	60.67	12.6	59.77
3+4 sandwich	13.4	60.67	12.6	59.77

Table 3.3. Results of the sandwich experiments

3.4 Uniform damage experiments

The effect of a uniform temperature field on refractory material was investigated by subjecting corund samples to quasi-stationary heating and subsequent cooling. The resulting acoustic damage was compared with the residual crushing strength.

3.4.1 Experimental set-up and procedures

Cube-shaped corund samples with sides of 50 mm are placed in a furnace and are heated quasi-stationary up to a range of temperatures. Except for the ultimate corner areas this symmetric sample geometry promotes the induction of a uniform temperature field After a dwelling period the samples are cooled down quasi-stationary to ambient temperature. Maximum furnace temperatures of 450 °C, 600 °C, 750 °C and 900 °C have been applied, which are within the temperature range of the thermal shock experiments described in sections 3.5 and 3.6. For each temperature level, 3 samples have been used. To determine the damage both the 54 kHz and 200 kHz transducers were used for transit time measurements with similar result. As their diameter better suited the sample size and the expected uniform damage field only the results obtained with the 54 kHz transducers are dealt with in the following. These transducers were positioned at the opposite face centers of the sample. This resulted in 3 mutually orthogonal measurements per sample. After the thermal treatment the samples were subjected to room temperature crushing tests. The nominal crushing strength was determined as the maximum load divided by the virgin sample area. Table 3.4 presents the detailed test programme.

1	Measure transit time, determine E_{dyn}
2	Heating at 2°C/min
3	Dwelling at maximum temperature for 120 min
4	Cooling at 2°C/min
5	Measure transit time, determine E_{dyn} and damage
6	Perform ambient crushing test, determine crushing strength

Table 3.4. Experimental programme for uniform damage tests

3.4.2 Results

Fig. 3.1 (left) presents the average acoustic damage of the batch as a function of the maximum temperature as well as the residual crushing strength of the individual samples as function of their dynamic Young's modulus determined after the thermal treatment. The trend lines are obtained from linear regression. The damage induced by the uniform temperature field appears to be linearly depending on the maximum temperature. As the attained testing temperatures do not exceed the maximum sintering temperature used in the processing of the refractory materials the occurring damage originates solely from thermal expansion mismatches within the microstructure of the material. Moreover, the material constituents are such that thermo-chemical changes at temperatures below the sintering temperature are not expected.

Only a moderate correlation appears to exist between the residual crushing strength and E_{dyn}, determined after the thermal treatment, as shown in Fig. 3.1 (right). The observed large statistical variations in the crushing strength, characteristic for coarse grained materials hampers definite conclusions. The closure of the micro-cracks present, prior to reaching the material failure state may also contribute to this moderate correlation. The material degradation determined with ultrasonic measurements is only weakly confirmed here by a deteriorating crushing strength. Nonetheless in recently published work [49] a relation between the degrading strength of refractory material in compression due to thermal shock and the corresponding degradation in ultrasonic longitudinal sound velocity has been observed.

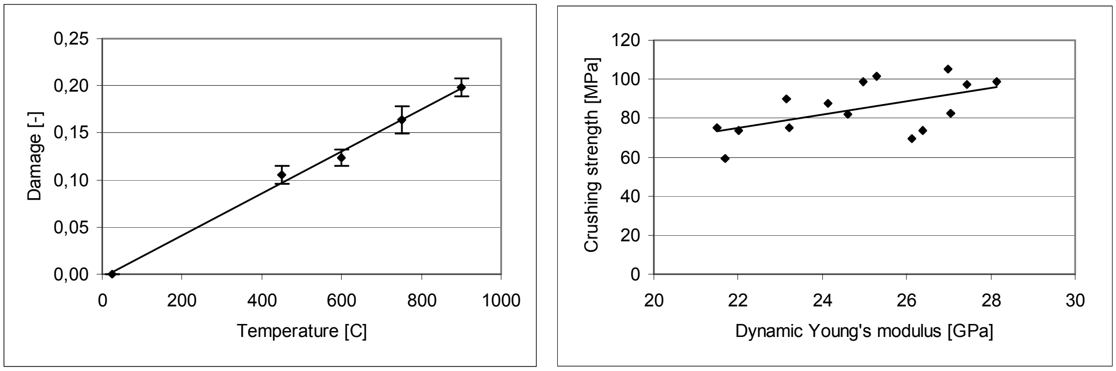

Fig.3.1. Uniform damage (left) and residual crushing strength (right)

3.5 Thermal shock experiments with hot air followed by water quenching

The proposed damage characterization method is validated mechanically by comparing the residual bending strength with the acoustic damage in samples subjected to water quench experiments.

3.5.1 Experimental set-up and procedures

To induce an up-quench thermal shock under mild conditions, beam shaped corund samples of ambient temperature and of dimensions 30 x 30 x 150 mm^3 are inserted rapidly into a furnace, which was pre-heated to a temperature of 1200 °C. After a dwelling period to allow redistribution to a uniform temperature, the samples are quenched in silent water of ambient temperature. A large volume of water was used to maintain a constant bath temperature during the down-quench.

The damage was determined from transit time measurements using the 200 kHz transducers at the locations depicted in Fig. 3.2. Acoustic measurements were performed at three sample locations in the two perpendicular transverse directions as well as centrally in the longitudinal direction. This results in 7 measurements per sample.

The experiment started with a series of 18 samples. After each test cycle 3 samples were removed from the series and subjected to a three-point bending test. Also a separate set of 3 virgin samples was subjected to a three-point bending test without receiving the thermal treatment. The bending strength was determined from the maximum load and the geometrical bending properties of the sample cross-section. The detailed test programme is presented in Table 3.5.

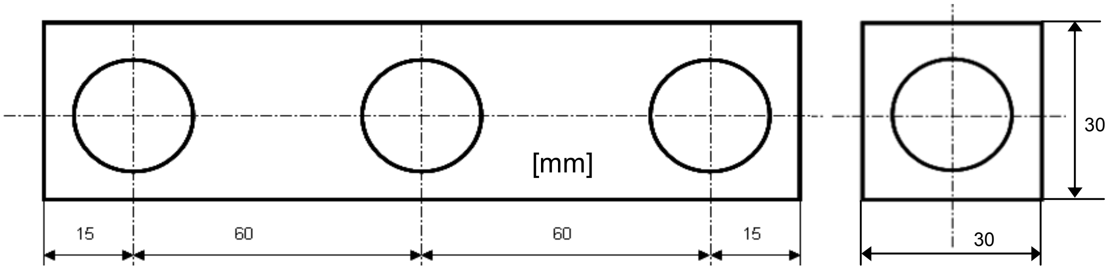

Fig. 3.2. Measurement grid (200 kHz transducers) used in the non-uniform damage test

	Start with batch of 18 samples
1	Measure transit time and determine E_{dyn}
2	Introduce samples into heated furnace of 1200 °C
3	Dwelling time of 60 min. in the furnace
4	Quench samples in ambient silent water
5	Dry samples for 60 min. at 110 °C
6	Measure transit time, determine E_{dyn} and damage
7	Remove 3 samples from batch and subject these to three-point bending test
8	Determine bending strength of these 3 samples
	Repeat steps 2 to 8 with the remaining samples

Table 3.5. Experimental programme for water quench tests

3.5.2 Results

Fig. 3.3 shows the average transversal and longitudinal damage determined from transit time measurement (left) and the residual bending strength (right) as function of the number of test cycles. The introduced mechanical damage variable D_b represents the relative decrease of the residual bending strength compared to the bending strength of the undamaged batch (10.28 MPa). With the effective stress concept [54] it can be shown that the damage defined by D_b is mechanically equivalent with the damage conventionally based on the degradation of the elastic stiffness properties. The determination of the residual mechanical Young's moduli however would require the inverse modelling of the three-point bending tests. It can be observed that the largest increase in acoustic as well as in mechanical damage is obtained in the first 3 thermal shock cycles. The damage saturates in the consecutive test cycles which might be due do the increasing density of the network of micro-cracks with the number of thermal shock cycles. This implies that the available energy, per test cycle, for the propagation of each micro-crack, decreases in the consecutive thermal shocks.

Qualitatively the average transverse and longitudinal damage exhibit a similar dependency on the number of thermal shock cycles. The higher damage in the longitudinal direction is attributed to the beam shaped sample geometry. The shrinkage of the sample in the water quench experiments induces a preferential direction of the micro-cracks, perpendicular to the longitudinal sample axis. Fig. 3.3 shows that indeed the longitudinal damage compares better with the damage variable D_b than the transversal damage.

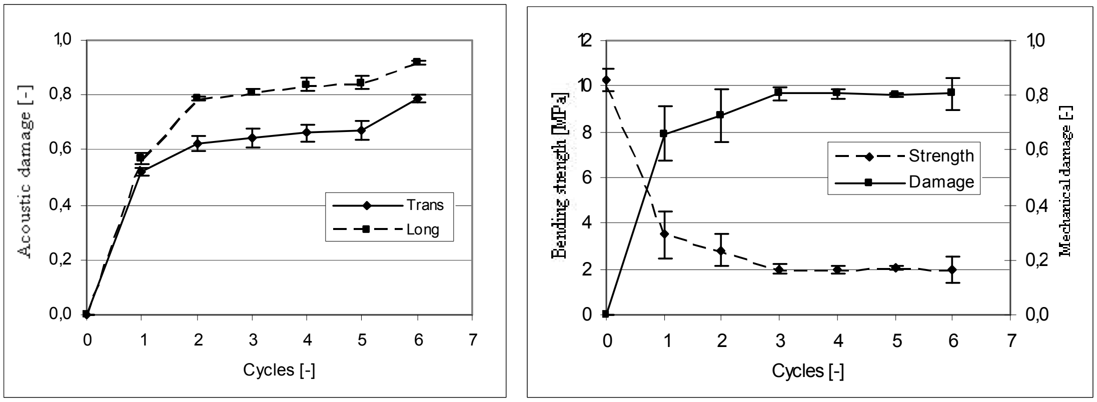

Fig. 3.3. Acoustic (left) and mechanical damage (right) after cycling

Fig. 3.4 presents the (residual) bending strength of the individual samples as function of the acoustic transversal damage (D_{trans}) and longitudinal damage (D_{long}). It can be observed that both damage indicators have a predictive value with regard to the degradation of the bending strength as a result of the applied thermal treatment. From a theoretical point of view, it is expected that the strength vanishes when the damage approaches unity. This is particularly the case for the longitudinal damage which again confirms its predictive value. The qualitative equivalence between D_b and D_{long}, presented in Fig. 3.3, as well as the observed correlation between the bending strength and the acoustic damage, presented in Fig. 3.4, underline the quantitative correlation between the defined damage indicators and the static damage. The latter is defined as the relative decrease of Young's modulus, determined from mechanical tests, compared to the initial, undamaged state. This static damage is typically used in constitutive models describing damage evolution [53, 54]. For the future experimental validation of such models it appears that a direct comparison can be made between the numerically calculated damage and the damage obtained from transit time measurements.

In general, thermal shock induces damage caused by tensile failure at the micro-scale. Assuming that material failure in bending proceeds accordingly, the results depicted in Figs. 3.3 and 3.4 indicate that transit time measurement of ultrasonic longitudinal waves provides an adequate and reproducible way to characterize the evolution of thermal shock damage.

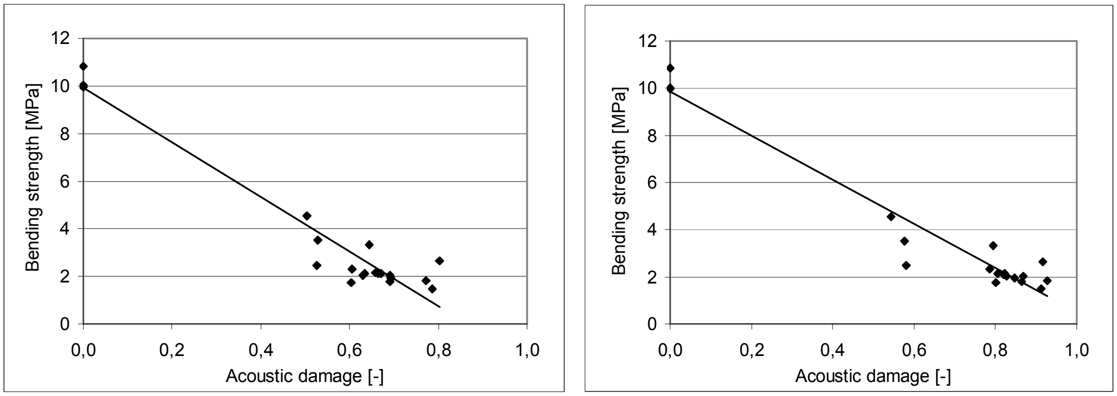

Fig. 3.4. Bending strength versus transversal (left) and longitudinal damage (right)

3.6 Thermal shock experiments with molten aluminium

To simulate thermal shock with realistic and reproducible boundary conditions, representative for metal making processes, refractory samples of ambient temperature were brought into contact with molten aluminium followed by cooling in ambient air. Experiments with chamotte and corund material were performed to investigate the viability of the experimental set-up. The corund material was subject to multiple thermal shock cycles to induce damage evolution and to produce a reliable set of data for future model validation.

3.6.1 Experimental set-up and procedures

Solid aluminium is molten and heated to 1000 °C in an open induction furnace, powerful enough to maintain a constant bath temperature. A guiding system, mounted on top of the furnace, enables an accurate and fast positioning of the test samples on top of the aluminium bath, minimizing the heating-up by radiation. Prior to this the aluminium bath was stirred to remove any oxidation layer present and to safeguard the thermal contact between bath and sample. The set-up is shown schematically in Fig. 3.5. After surface contact with the aluminium bath for a period of time, the samples were removed from the set-up and cooled in ambient air, inducing a down-quench thermal shock. According to the calculated Hasselman parameter R of the sample materials the imposed difference of initial sample and bath temperature is high enough to induce thermal shock damage.

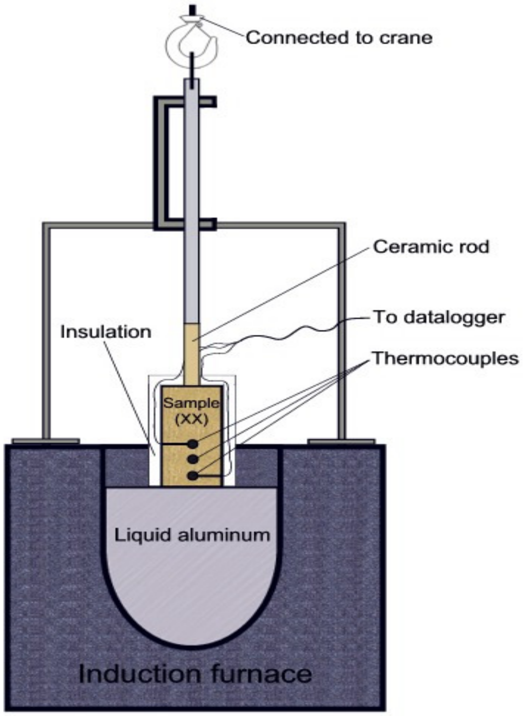
Connected to crane
Ceramic rod
To datalogger
Insulation
Thermocouples
Sample (XX)
Liquid aluminum
Induction furnace

Fig. 3.5. Thermal shock test set-up

A number of three chamotte and six corund samples of dimensions 50 x 50 x 150 mm^3 were used. The temperature was measured in two corund samples (1 and 2). From the other corund samples (3 to 6) and from the chamotte samples the damage was determined.

Apart from the quenched surface (50 x 50 mm^2) all sample sides were cladded with 30 mm thick thermal insulation. This triggers a one-dimensional temperature profile similar to that encountered in thick-walled refractory linings of high temperature installations. Terracoat ® was applied at the quenched sample side to prevent invasion of the molten aluminium.

During the experiment the temperature was measured and recorded as a function of time of samples 1 and 2 of the corund material. To this end thermocouples were mounted on the longitudinal axis of the samples, at distances of 10, 25 and 40 mm from the quenched sample side. To minimize the effect on the temperature profile, the holes for the thermocouple wires were drilled orthogonally as illustrated schematically in Fig. 3.6. This figure also shows the ceramic tube, inserted over a length of 40 mm in the sample for the connection with the guiding system.

With each of the chamotte samples a single thermal shock cycle was performed. The corund samples were subject to three consecutive thermal shock cycles (indicated as C1, C2 and C3) in order to investigate the evolution of thermal shock damage. After a period of 20 min. surface contact with the molten aluminium a hold time of 48 hours was maintained to allow the complete cooling down of the samples. Consecutively, the insulation material was removed from the chamotte samples and from the corund samples 3 to 6. Transit time measurements were then performed at various locations on these samples. This was also done prior to the first thermal treatment. The 200 kHz transducers were positioned at the locations coinciding with the line intersections in the measurements grids schematically illustrated in Fig. 3.7. Compared to the chamotte material the grid used for the corund material was of higher density as these results are to be used for quantitative model validation in the furnace. The transit time measurements were performed between the opposite pairs of sample faces in the two orthogonal directions. In the processing of the results it is assumed from theoretical considerations that the experimental damage will be symmetric with respect the longitudinal sample axis. The damage after each thermal shock cycle was calculated as the relative decrease of the corresponding residual E_{dyn} compared to the value in the undamaged state. The detailed test programme with the corund samples is presented in Table 3.6.

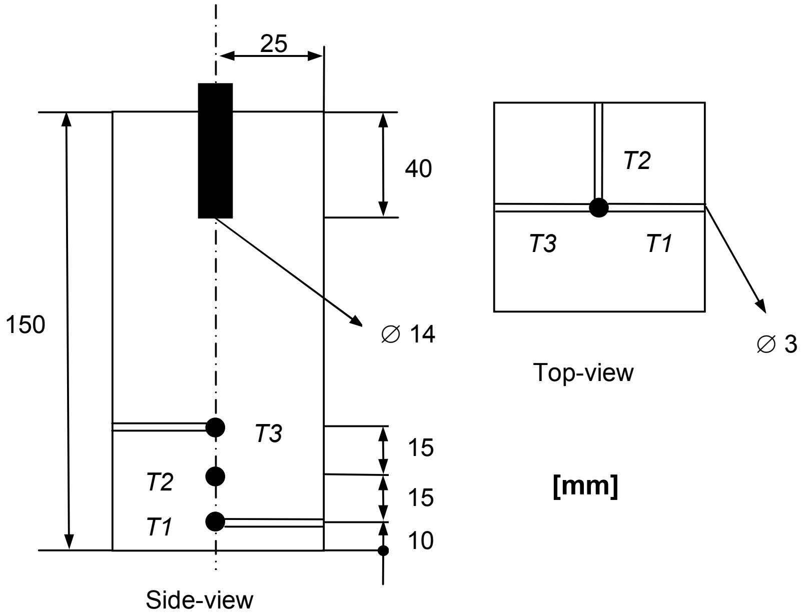
25
40
150
∅ 14
T3
T2
T1
15
15
10
Side-view
T2
T3
T1
∅ 3
Top-view
[mm]

Fig. 3.6. Corund sample with thermocouple locations and wire feeds

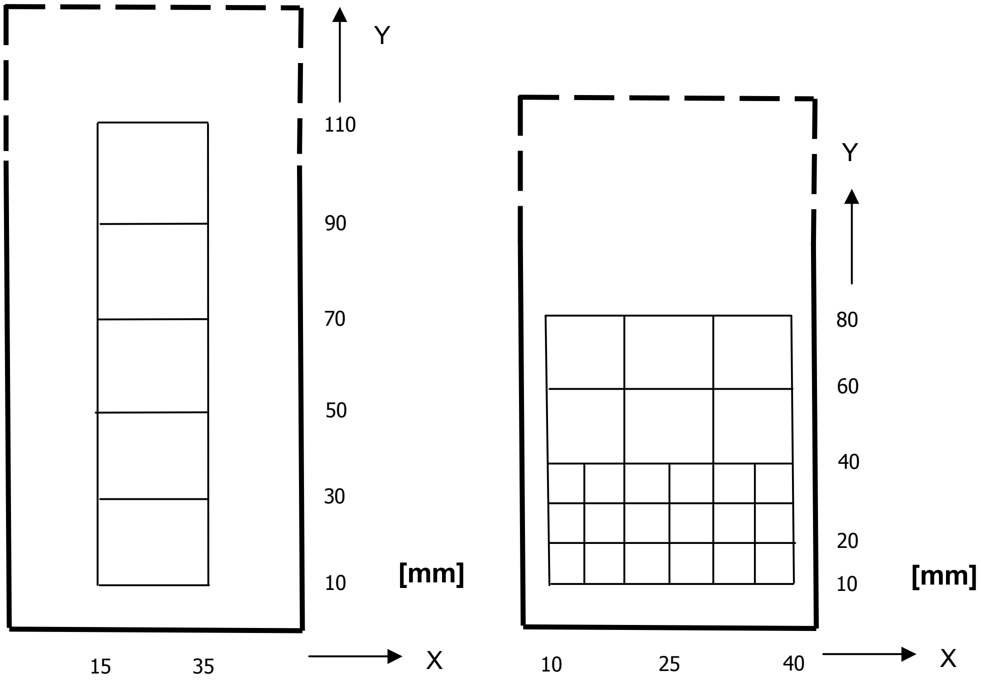
Y
110
90
70
50
30
10
[mm]
15
35
X
Y
80
60
40
20
10
[mm]
10
25
40
X

Fig. 3.7. Measurement grid for chamotte (left) and corund sample (right)

1	Measure transit time, determine E_{dyn} of samples 3 to 6
2	Surface contact of samples with molten aluminium of 1000 °C for 20 min. Register temperature of samples 1 and 2
3	Cool down samples in ambient air for 48 hrs. Continue temperature registration of samples 1 and 2 for 30 min.
4	Measure transit time, determine E_{dyn} and damage of samples 3 to 6
	Repeat steps 2 to 4 twice

Table 3.6. Experimental programme for one-sided thermal shock tests with corund samples

3.6.2 Results with chamotte material

Fig. 3.8 (left) presents the damage determined in an individual chamotte sample. The orthogonal pairs of sample surfaces on which the acoustic measurements are performed are denoted by AA and BB. It can be observed that the single thermal shock cycle has induced significant damage in the sample. Despite the scattering in damage at a given Y-coordinate the trend of an increasing damage with a decreasing distance to the molten aluminium is noticeable. The observed scattering in the results is ascribed to the common variation in material properties of refractory bricks due to processing and their heterogeneous granular structure.

The damage averaged over all X-coordinates, at a given Y-coordinate of all chamotte samples used, is presented in Fig. 3.8 (right). The use of 3 test samples and 4 transit time measurements per sample at a given Y-coordinate results in an average of 12 transit time measurements per data point. It can be concluded that with the presented experimental set-up the damage can be effectively created while the characterization method renders a reproducible quantification.

Fig. 3.8 (right) shows that most damage is concentrated in the vicinity of the quenched sample side where the temperature gradients are the highest. At 10 mm distance from the molten aluminium a damage level of 0.39 is achieved. This may be exceeded by even higher damage levels at smaller distances from the quenched sample side. From a macroscopic mechanical point-of-view this is unlikely. The thermal expansion at the heated, quenched sample side induces a compressive stress state equilibrated somewhat higher in the sample by a state of tensile stress. The latter induces tensile strains exceeding the material limits and causing the initiation of damage at some distance from the quenched sample surface. Nonetheless at distances to the molten aluminium smaller than 10 mm, thermal expansion mismatches at the microscopic level may induce micro-cracks and damage. Here appropriate transit time measurements could not be performed given the 20 mm diameter of the transducers used.

Lower thermal gradients will be present higher in the sample where uniform, thermal damage might be more prominent. Contributions to the observed damage may also originate from phase changes in certain constituents (e.g. SiO_2) of the sample material. This can be accompanied by local volume changes and thermal expansion affecting the transit time of passing ultrasonic waves and E_{dyn} determined thereof.

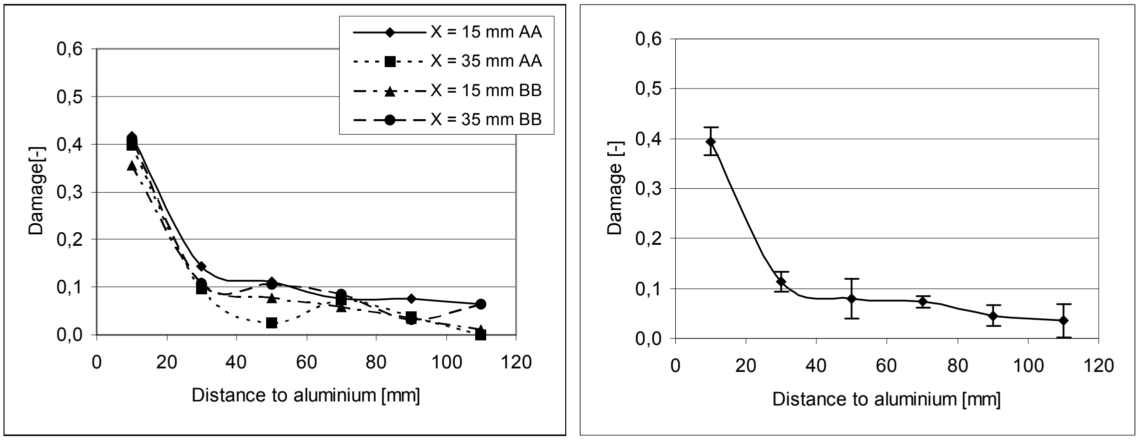

Fig. 3.8. Damage in an individual chamotte sample (left) and averaged over all coordinates and all samples (right) (AA and BB denote orthogonal measurement directions)

3.6.3 Results with corund material

Fig. 3.9 presents the temperatures *T1, T2* and *T3* (see Fig. 3.6) of corund samples 1 and 2 measured in test cycle 1. A good reproducibility of the temperatures can be observed indicating a reproducible heat transfer to and from the samples in respectively the heating and cooling cycle. Nonetheless sample 2 seems to cool down somewhat slower. This could be due to residues of aluminium, attached to the quenched sample side and affecting the irradiative heat transport to the ambient surroundings.

Evidently, the thermocouple temperature *T1* near the quenched sample side exhibits the steepest increase over time. At that location the highest temperature gradients and thermal shock appear. The temperature at which the maximum temperature rates occur lies below 300 °C, a temperature area in which the properties of the corund sample material do not change. The temperatures *T2* and *T3* at positions 25 and 40 mm still rise after the onset of the cooling period. At these locations the heat flow is still directed from the molten aluminium into the sample. At even higher locations the temperature might continue to rise during the first half hour of the cooling period. Uniform thermal damage may be more dominant there as the temperature rates will remain relatively low.

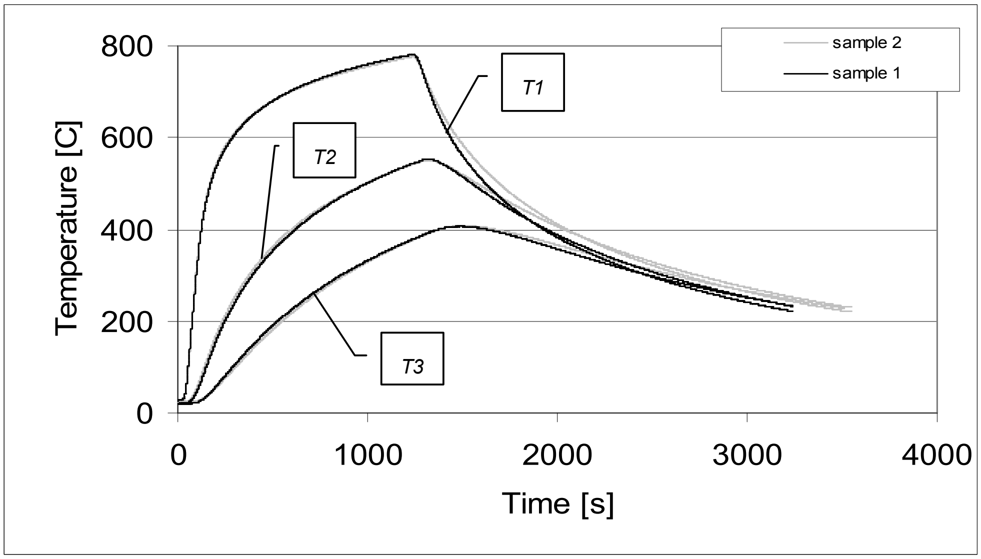

Fig. 3.9. Temperatures in corund samples 1 and 2 during the first test cycle

Figs. 3.10 to 3.13 present the average damage distribution in the corund samples 3 to 6 in the three consecutive test cycles C1 to C3. The damage depicted is the average value of the pairs obtained at the X-coordinates (see Fig. 3.7 (right)) 20 and 30 mm, 15 and 35 mm as well as 10 and 40 mm. As the transit time measurements were performed on the two pairs of orthogonal sample faces on a batch consisting of four samples the presented data points are obtained from averaging over 16 sets of data. It is again assumed here that the sample geometry induces a symmetric damage pattern with respect to the longitudinal sample axis. Analogically the data points at the 25 mm X-coordinate (sample axis) are obtained from averaging over 8 sets of datas. It can be observed that the set of data depicted represents the damage evolution in the sample material in a reasonably reproducible way. The exposure of the samples to multiple consecutive thermal shock cycles has lead to a reproducible damage at various locations along the sample height. This confirms the homogeneity of the sample material with regard to the determined acoustic stiffness properties in damaged and in undamaged state. It appears furthermore that the damage pattern determined at the X-coordinates 10 and 40 mm was not influenced by edge effects and surface roughness resulting from possible damage caused by cutting the samples to size.

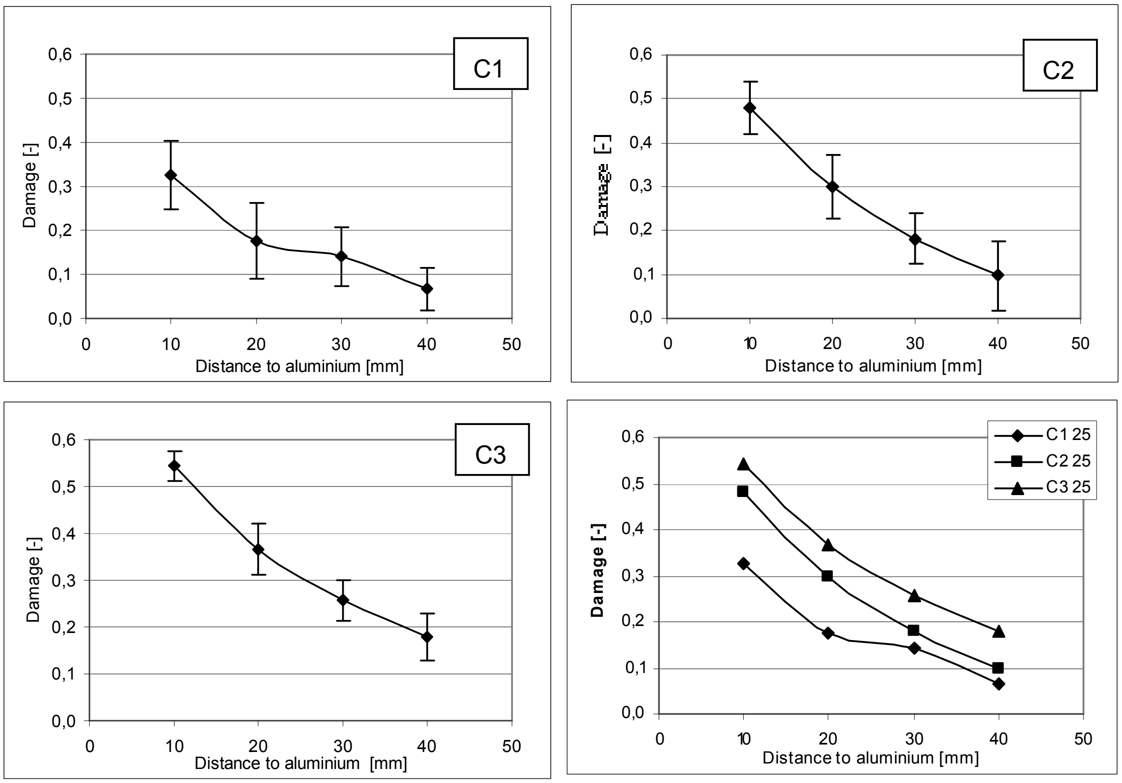

Fig. 3.10. Damage in the corund samples at the 25 mm X-coordinate (sample axis)

As predicted by the low allowable value of the governing Hasselman parameter R, the corund sample material will be affected by damage due to the sudden heat input induced by the repeated surface contact with the molten aluminium. Thermal conduction and forced convection due to flowing of the molten aluminium in the induction furnace both contribute to the heat transfer in the up-quench stage. Compared to the cooling stage, characterized by radiation and free convection, this results in a high heat transfer coefficient and corresponding thermal gradients. The difference in temperature rates at the beginning of the heating and cooling period can be observed in Fig. 3.9. At e.g. the 25 mm X-coordinate maximum damage levels of 0.32, 0.48 and 0.53 were obtained in the consecutive thermal shock cycles C1 to C3, respectively. In all test cycles the damage decreases rapidly with increasing distance to the aluminium contact area. The fact that a uni-axial thermal load is applied, is reflected in the damage which does not vary significantly between the X-coordinates for a given Y-coordinate.

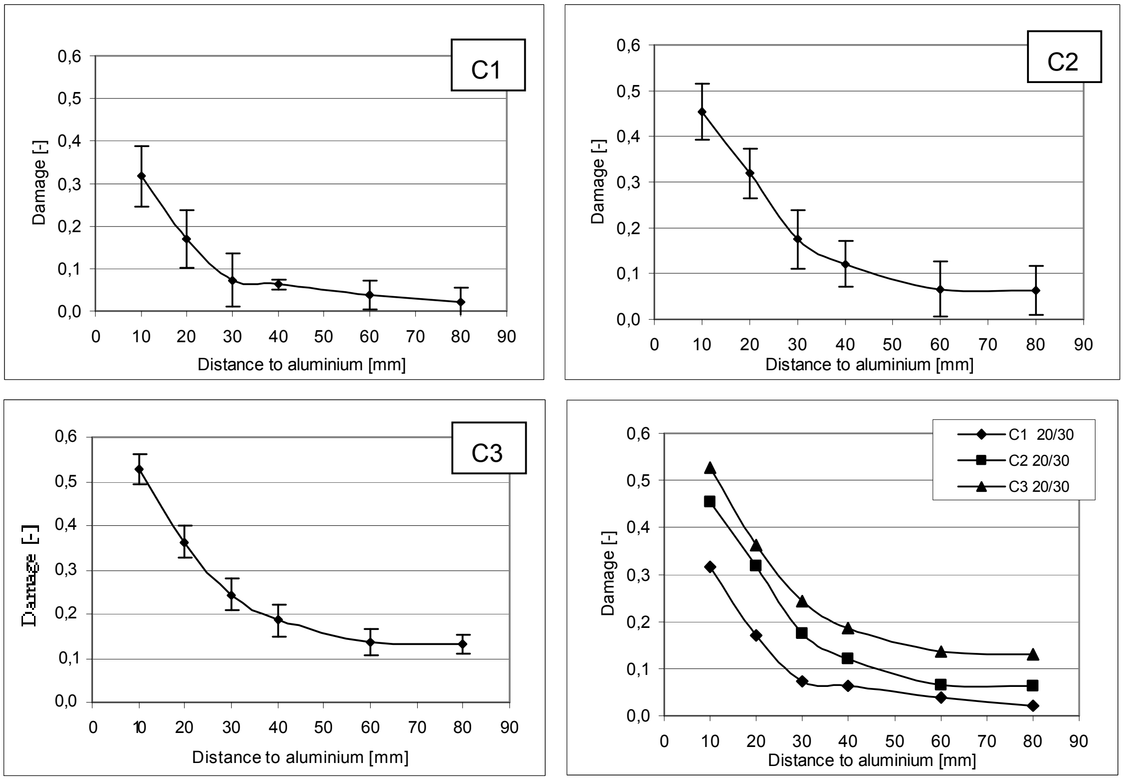

Fig. 3.11. Damage in the corund samples at the 20/30 mm X-coordinate

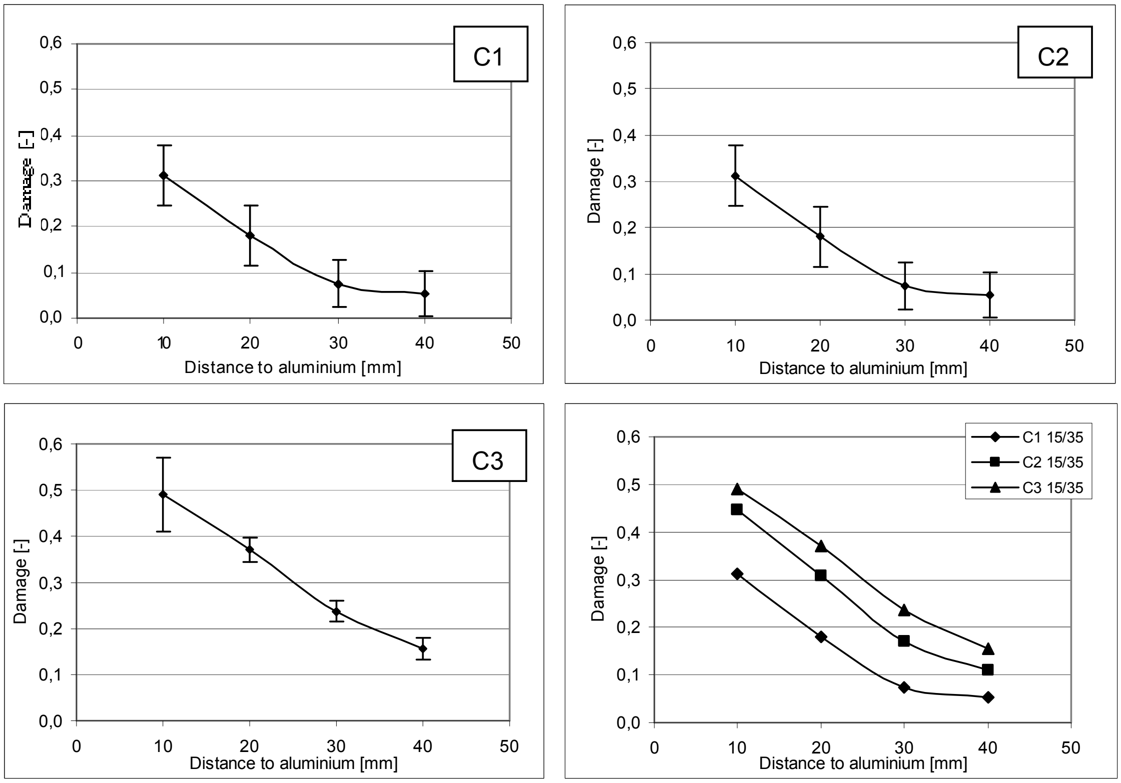

Fig. 3.12. Damage in the corund samples at the 15/35 mm X-coordinate

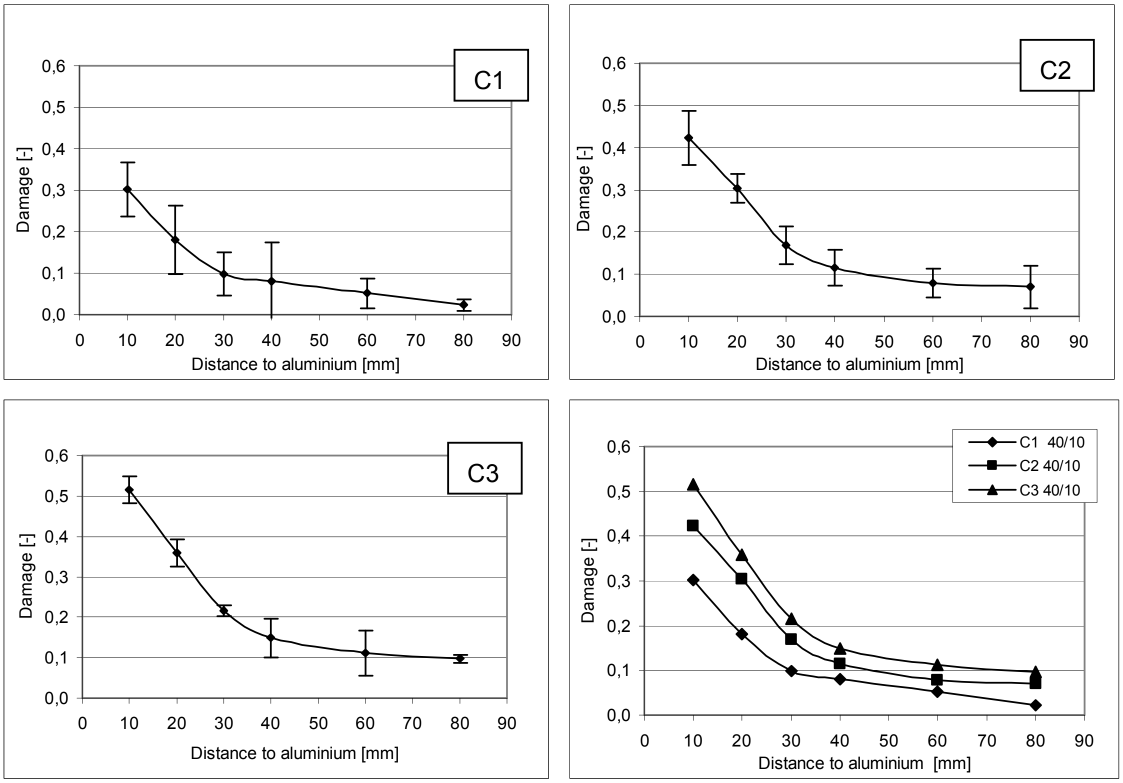

Fig. 3.13. Damage in the corund samples at the 10/40 mm X-coordinate

The evolution of damage is the highest in the first thermal shock cycle. Analogous to the previously discussed water-quench tests, the damage is saturating in the consecutive test cycles. In view of the constant temperature of the aluminium bath the heat input in the consecutive test cycles is invariant although the damage increases considerably. This cannot be attributed to a uniform damage development as the maximum temperature is already achieved in the first test cycle. Apparently with every test cycle the sample material becomes increasingly susceptible to further damage propagation. With regard to the considerable damage increase at particularly the X-coordinates 60 and 80 mm this effect may be amplified by shielding of the heat transport by the micro-cracks present. The degraded thermal conductivity then induces higher thermal gradients in the material and more non-uniform damage. When the insulated test sample is considered as a semi-infinite wall an approximation of the penetration depth of a sudden heat pulse can be derived from the governing analytical solution for the temperature distribution [59] and reads:

$$d = \sqrt{\pi \frac{\lambda}{\rho C_p} t} \tag{3.4}$$

with t the time period of surface contact with the molten aluminium. The penetration depth is then estimated to be 7.7 cm, using the properties listed in Table 3.2. This indicates that at sample locations as high as the 80 mm Y-coordinate the achieved thermal gradients may be high enough to cause non-uniform damage. The occurring thermal gradients can be quantified more accurately with appropriate thermal models. This item is, however, not within the scope of this paper. It is finally stated that property changes at temperatures below the specified ultimate sintering temperature can only be of thermo-mechanical nature, according to the information supplied by the producer of the refractory bricks used.

Fig. 3.14 shows the damage at the 25 mm X-coordinate, after the first test cycle, compared at the thermocouple positions with the maximum occurring temperature rate as determined from Fig. 3.9. The damage at the 25 mm thermocouple position was obtained from averaging the damage determined at the 20 mm and 30 mm Y-coordinate. A prediction of the uniform damage at the thermocouple positions, has also been added. To this end, the trend line derived from the uniform damage experiments as presented in Fig. 3.1 (left), has been used. It can be observed that the temperature rates decline rapidly with increasing distance from the quenched sample surface. Yet, a temperature rate of 0.47 °C/s (28 °C/min) at the 40 mm thermocouple position is sufficient to induce thermal shock damage in the corund refractory material used. This implies that thermal shock also contributes to the damage present at even higher locations in the sample. Temperature rates as low as 0.17 °C/s (10 °C/min) suffice to cause non-uniform damage in the corund material used.

Fig. 3.14 reveals that the relative contribution of the uniform damage to the total damage increases with an increasing distance from the aluminium. Moreover, the predicted uniform damage exceeds the experimentally determined total damage at the 40 mm thermocouple position in a rather unphysical way. This is an indication that the development of uniform damage may be hampered by the development of non-uniform thermal shock damage. Both damage mechanisms may interact if in a certain material point the temperature as well as the temperature rate are increasing simultaneously. Similar to the observed damage saturation in consecutive thermal shock cycles the growth of uniform damage may also be shielded by the presence of non-uniform damage developed previously or vice versa.

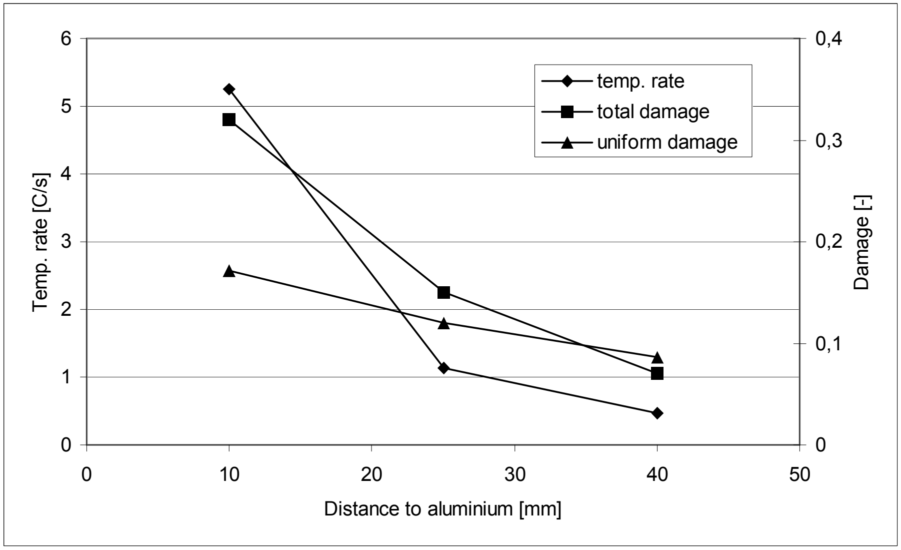

Fig. 3.14. Temperature rates and damage in corund samples at the thermocouple positions

3.7 Discussion

In high temperature installations the refractory bricks are surrounded by adjacent bricks and mortar joints imposing certain mechanical constraints. This influences the thermal shock behaviour to a degree where layer-wise spalling is prominent [60, 61]. Although the heat transfer conditions in the one-sided quench tests are representative for thermal shock occurring in metal making processes, it is difficult to impose the aforementioned mechanical boundary conditions in a reliable and reproducible manner. The influence of such constraints on the exhibited thermal shock behavior can, however, be investigated with a numerical model which has to incorporate the constitutive damage behaviour representative for coarse grained refractory material.

The transit time measurements performed during the one-sided thermal shock experiments allowed the location-dependent characterization of damage evolution. Nonetheless the damage at a distinct location between the transducers cannot be quantified. This requires the use of a numerical damage model which can however be validated with the obtained set of data and subsequently be used to predict the damage at all distinct sample locations. The transit time measured, in case of non-uniform damage, is the cumulated transit time of the ultrasonic waves passing the various damaged material zones present between the transducers (Section 3.3). This facilitates the comparison with model predictions. The calculated damage in a material volume of finite dimensions can be recalculated into a representative transit time. Summation of such calculated transit times over the transducer distance yields a numerical simulation which can be compared with its experimental counterpart.

When a refractory material is subject to thermal shock the interaction between non-uniform and uniform damage may be of importance. This interdependency of both damage mechanisms can be investigated experimentally. Test samples, previously subjected to uniform damage experiments, can be subjected consecutively to thermal shock experiments or vice versa. However, if a temperature wave is travelling non-uniformly (i.e. via unstationary heat transport) through the material both non-uniform and uniform damage can develop simultaneously and may interact. In a material, sensitive to both damage mechanisms, this occurs when both the thermal gradients (non-uniform damage) and the temperatures (uniform damage) are increasing and have not yet reached their maximum values. This distinguishable effect on the mechanical behaviour is not reflected well by consecutive experiments involving both damage mechanisms and can only be investigated by indirect identification procedures, that rely on a parallel numerical description of the interaction phenomena. The following, frequently used relation accounts for the simultaneous interaction between non-uniform, elastic and uniform, thermal damage [55-57]:

$$D = 1 - (1 - d_{el})(1 - d_{th}) = d_{el} + d_{th} - d_{el} d_{th} \tag{3.5}$$

where d_{el} and d_{th} represent elastic and thermal damage respectively. When both damage mechanisms contribute to the evolution of the total damage Eq. (3.5) clearly shows that they affect one another.

The experimental results of the one-sided quench experiments indicate that the thermal conductivity of the corund material may be influenced by damage. Similar to the degradation of elastic material properties, the degradation of the thermal conductivity by damage could also be quantified as a function of the damage variable D. When damage is considered as a form of porosity, Loeb's equation [62] is useful. Here the thermal conductivity decreases linearly with the evolution of damage until a residual value is attained. The parameters in the damage-conductivity relation can be obtained from (room temperature) thermal conductivity measurements on samples previously subjected to uniform damage experiments.

The residual mechanical properties determined after the uniform damage and water quench experiments only showed a moderate reproducibility compared to that of the corresponding acoustic properties. The coarse grain structure of the refractory material causes a variation in the location of crack initiation and propagation and a corresponding variation in the resulting mechanical properties. These may be obtained alternatively using relations as proposed by Posarac et al. [49] and Aly et al. [63] who relate the degradation of strength to a corresponding decrease in ultrasonic velocity i.e. acoustic damage. (The strength of the undamaged material has to be determined in that case).

3.8 Conclusions

In order to investigate the evolution of thermal shock damage in refractory materials, a new experimental approach has been proposed. In contradiction to previously described methods, the imposed reproducible heat transfer conditions are representative for thermal shock in high temperature installations in metal making processes. The exposure of chamotte and corund refractory material to molten aluminium followed by passive air cooling induced high temperature gradients and corresponding damage levels. After consecutive test cycles the evolution of damage in the corund samples could be quantified in a reproducible way by measuring the transit time of ultrasonic longitudinal waves at various sample locations. With independent experiments the mechanical validity of transit time measurement was established. Apart from the application of laborious tomographic methods the location-dependent quantification of damage evolution in heterogeneous, granular materials has not been described before in the literature.

In a refractory material subject to an unstationary temperature increase (thermal shock) both non-uniform and uniform damage can develop simultaneously and may interact. Non-uniform damage is induced by internally and externally constrained thermal expansion. Uniform damage is induced by thermal expansion mismatches in the micro-structural constituents of the material. Internally constrained thermal expansion can be reproducibly induced with the proposed experimental set-up for one-sided up-quench. The investigation of externally constrained thermal expansion and its effect on the exhibited thermal shock damage as well as the interaction between uniform and non-uniform damage can only be suffiently investigated using a numerical model which can however be validated with the produced set of data.

Although saturating, the growth of damage in the consecutive test cycles performed with the corund material is considerable. This indicates an increased susceptibility of the corund material to the growth of non-uniform damage with an increasing number of test cycles, possibly facilitated by the shielding of heat transfer by damage. Locally this may lead to a degraded thermal conductivity, higher thermal gradients and a corresponding higher level of non-uniform damage.

3.9 References

[1] Wei, W.J., Lin, Y.P., *Mechanical and thermal shock properties of size graded MgO-PSZ refractory*, J. Eur. Cer. Soc., 2000, Vol. 20, pp. 1159-1167

[2] Volkov, T., Jancic, R., *Prediction of thermal shock behavior of alumina based refractories, fracture resistance parameters and water quench test*, Proceedings of CIMTEC 2002, pp. 109-116, Eds. P. Vincenzini, G. Aliprandi, 2003

[3] Ko, Y.C., Horng, W.H., Wang, C.H., Chieh Teng, L.C., *Fines content effects on the thermal shock resistance of Al2O3-Spinel Castables*, China Steel Technical Report, 2001, Vol. 15, pp. 7-14

[4] Aksel, C., *The effect of mullite on the mechanical properties and thermal shock behaviour of alumina-mullite refractory materials*, Cer. Int., 2003, Vol. 29, pp. 183-188

[5] Cotterel, B., Sze, W.O., Caidong, Q., *Thermal shock and size effects in castable refractories*, J. Am. Cer. Soc., 1995, Vol. 78(8), pp. 2056-2064

[6]. Tonnesen, T., Telle, R., *Evaluation of thermal shock damage in castables by a resonant frequency and damping method*, Proceedings of 49th Internationales Feuerfest-Kolloquium 2006, pp. 133-136

[7] Anderson, T., Rowcliffe, D.J., *Thermal cycling of indented ceramic materials,* J. Eur. Cer. Soc., 1998, Vol. 18, pp. 2065-2071

[8] Absi, J., Glandus, J.C.*, Improved method for severe thermal shocks testing of ceramics by water-quenching*, J. Eur. Cer. Soc., 2004, Vol. 24, pp. 2835-2838

[9] Boccaccini, D.N., Leonelli, C., *Thermal shock behaviour of mullite-cordierite refractory materials*, Advances in Applied Ceramics, 2007, Vol. 106(3), pp. 142-148

[10] Sebbani, M.J.E., Allaire, C., *Influence of firing temperature on correlation between thermal shock and mechanical impact resistance of refractory castables,* British Ceramic Transactions, 2000, Vol. 99(5), pp. 215-218

[11] Lee, J.K., Lee, J.H., Lee, S.P., *Nondestructive evaluation of damage behavior of ceramic under thermal shock cycle*, Key Engineering Materials, 2004, Vol. 270-273, pp. 497-502

[12] Das, A.C., Mukherjee, S., Chaudhury K., Niyogi, S.K., Phani, K.K., *Crack growth in castable refractory due to thermal shock fatigue: an acousto-ultrasonic study,* Transactions of the Indian Ceramic Society, 1993, Vol. 52(4), pp. 139-145

[13] Chung, H.W., *Ultrasonic testing of concrete after exposure to high temperatures*, NDT International, 1985, Vol. 18(5), pp. 275-278

[14] Kamiya, N., *Thermal proof test of ceramics*, Thermal shock and thermal fatigue behaviour of advanced ceramics, pp. 473-482, Eds. Schneider, G.A., Petzow, G., Kluwer Academic Publishers, 1993

[15] Bao, Y.W., Wang, X.H., Zhang, H.B., Zhou, Y.C, *Thermal shock behavior of* Ti_3AlC_2 *from between 200℃ and 1300℃*, J. Eur. Cer. Soc., 2005, Vol. 25, pp. 3367-3374

[16] Aksel, C., Riley, F.L., *Young's modulus measurements of magnesia-spinel composites using load-deflection curves, sonic modulus, strain gauges and Rayleigh waves*, J. Am. Cer. Soc., 2003, Vol. 23, pp.3089-3096

[17] Aksel, C., Warren, P.D., *Thermal shock parameters* $[R, R''',R'''']$ *of magnesia-spinel composites*, J. Eur. Cer. Soc., 2003, Vol. 23, pp. 301-308

[18] Soboyejo, W.O., Mercer, C., *Investigation of thermal shock in a high-temperature refractory ceramic: a fracture mechanics approach*, J. Am. Cer. Soc., 2001, Vol. 84(6), pp.1309-1314

[19] Uzaki, N., Ishii, H., Aratani, K., Kawakami, T., Sakai, T., *Development of magnesite-chrome refractories with high thermal shock resistance*, Interceram, 1991, Vol. 5, pp. 279-283

[20] Sen, S., Chowdhury, A., Roy, S.K.C., Ghosh, K.S., *Comparative behaviour of fracture and thermal shock behaviour of conventional, low cement and ultra low cement castables*, Proceedings of Unitecr 97, New Orleans, USA, 1997, pp. 53-62

[21] Glandus, J.C., Hugot, F., *Thermo-mechanical behavior of structural ceramics submitted to mild thermal shocks,* Proceedings of Euroceramics V, 1997, pp. 619-622

[22] Mignard, F., Olagnon, C., Fantozzi, G., *Acoustic emission monitoring of damage evaluation in ceramics submitted to thermal shock,* J. Eur. Cer. Soc., 1995, 15, pp. 651-653

[23] Aksel, C., *Mechanical properties and thermal shock behaviour of alumina-mullite-zirconia and alumina-mullite refractory materials by slip casting*, Cer. Int., 2003, Vol. 29(3), pp. 311-316

[24] Hamidouche M., Bouaouadja, N., Olagnon, C., Fantozzi, G., *Thermal shock behaviour of mullite ceramic*, Cer. Int., 2003, Vol. 29(6), pp. 599-609

[25] Schneibel, J.H., Sabol, S.M., Morrison, J., Ludeman, E., Carmichael, C.A., *Cyclic thermal shock resistance of several advanced ceramics and ceramic composites,* J. Am. Cer. Soc., 1998, Vol. 81(7), pp. 1888-1892

[26] Panda, P.K., Kannah, T.S., Dubois, J., Olagnon, C., Fantozzi, G., *Thermal shock and thermal fatigue study of ceramic materials on a newly developed ascending thermal shock test equipmen*t, Science and Technology of Advanced Materials, 2002, Vol. 3, pp. 327-334

[27] Soady, J.S., Plint, S., *A quantitative thermal shock approach to the development of magnesia-spinel refractories for the cement kiln*, Proceedings of Unitecr 1991, Aachen, Germany, 1991, pp. 443-449

[28] Panda, P.K., Kannan, T.S., Dubois, J., Olagnon, C., Fantozzi, G., *Thermal shock and thermal fatigue study of alumina*, J. Eur. Cer. Soc., 2002, 22, pp. 2187-2196

[29] Coppack, T.J., *A method for thermal cycling refractories and an appraisal of its effect by a non-destructive technique*, J. of the Brit. Cer. Soc., 1981, Vol. 80(2), pp. 43-46

[30] Meyer-Rau, S., Telle, R., *Testing strategies for corrosive interactions of ceramics with semi-solid and molten metal alloys*, J. Eur. Cer. Soc., 2005, Vol. 25, pp. 1049-1055

[31] Radenthein, M.O., *Fully automated thermal shock test method for testing fired refractory brick*, Radex-Rundschau, 1990, Vol. 2,3, pp. 268-274

[32] Dienst, W., Scholtz, H., Zimmermann, H., *Thermal shock resistance of ceramic materials in melt immerion test*,
J. Eur. Cer. Soc., 1989, Vol. 5(6), pp. 365-370

[33] Morita, N., *Generation and propagation behavior of laser induced thermal cracks*, J. of the Cer. Soc. of Japan, 1993, Vol. 101(5), pp. 522-527

[34] Akiyama S., Amada, S., *A new method to evaluate the thermal shock resistance of ceramics by laser pulse irradiation*, Fusion Technology, 1992, Vol. 23, pp. 426-434

[35] Benz, A., Nickel, H., Naoumidis, A., Menzel, S., Wetzig, K., Rossek, U., *Thermal shock behaviour of various first-wall materials under simulation load test by laser beam irradiation*, Journal of Nuclear Materials, 1994, Vol. 212-215, pp. 1318-1322

[36] Mizutani, Y., Nishikawa, T., Fukui, T., Takatsu, M., *Thermal shock fracture of ceramic disc under rapid heating*, J. of the Cer. Soc. of Japan, Int. Edition, 1995, 103(5), pp. 525-528

[37] Leatherland J.L., Rawlings, R.D., *Thermal shock testing of alumina-graphite refractories*, Proceedings of Steelmaking Conference No. 79, 1996, Vol. 23(6), pp. 51-21

[38] Bell. D. A., *Thermal shock of magnesia-graphite refractories*, Proceedings of Unitecr 1991, Aachen, Germany, 1991, pp. 342-344

[39] Latella, B.A., Tainshun, L., *The initiation and propagation of thermal shock cracks in graphite*, Carbon, 2006, Vol. 44(14), pp. 3043-3048

[40] Boccaccini, D.N., Romagnoli, M., Veronesi, P., Cannio, M., Leonelli, C., Pellacani, G.C., *Quality control and thermal shock damage characterization of high-temperature ceramics by ultrasonic pulse velocity testing,* Int. J. Appl. Ceram. Technol., 2007, Vol. 4(3), pp. 260-268

[41] Boccaccini, D.N., Romagnoli, M., Kamseu, E., Veronesi, P., Leonelli, C., Pellacani, G.C., *Determination of the thermal shock resistance in refractory materials by ultrasonic pulse velocity measurement*, J. Eur. Cer. Soc., 2007, Vol. 27, pp. 1859-1863

[42] Quintela, M.A., Melo, T.M.F., Lage, I.J., Rodrigues, J.A., Pandolfelli, V.C., *Thermal shock resistance of carbon-containing refractories*, 2003, Interceram, Refractories Manual 2003

[43] Geck, H.G., Langhammer, H.J., Chakraborty, A., *Kammerofen zur betriebsnahen Prüfung der Temperaturwechselbeständigkeit feuerfester Steine,* Stahl und Eisen, 1973, Vol. 93(21), pp. 967-976

[44] Yamuna, A., Honda, S., Sumita, K., Yanagihara, M., Hashimoto, S., Awaij, H., *Synthesis, sintering and thermal shock resistance estimation of porous*

cordierite by IR heating, Microporous and mesoporous materials, 2005, Vol. 85(1,2), pp. 169-175

[45] Wei, G.C., *Hot gas method and apparatus for thermal shock testing*, Thermal shock and thermal fatigue behaviour of advanced ceramics, 1993, pp. 483-494, Eds. Schneider, G.A., Petzow, G., Kluwer Academic Publishers

[46] Konsztowicz, K.J., *Acoustic emission amplitude analysis in crack growth studies during thermal shock of ceramics*, Thermal shock and thermal fatigue behaviour of advanced ceramics, 1993, pp. 429-441, Eds. Schneider, G.A., Petzow, G., Kluwer Academic Publishers

[47] Tuchozka-Szmeja, B., Wala, T.B., *Thermal shock acoustic emission and microstructure of refractories I. High alumina refractories (60-90% Al_2O_3),* Cer. Int., 1994, Vol. 20(6), pp. 359-366

[48] Davis, W.R., Brough, R., *Ultrasonic techniques in ceramic research and testing,* Ultrasonics, May 1972, pp. 118-126

[49] Posarac, M., Dimitrijevic, M., Volkov-Husovic, T., Devecerski, A., Matovic, B., *Determination of thermal shock resistance of silicon carbide/cordierite composite material using nondestructive test methods*, J. Eur. Cer. Soc., 2008, Vol. 6, pp. 1275-1278

[50] Landis, E.N., Nagy, E.N., Keane, D.T., Nagy, G., *Technique to measure 3D work-of-fracture of concrete in compression,* Journal of Engineering Mechanics, June 1999, pp. 599-605

[51] Daigle, M., Fratta, D., Wang, L.B., *Ultrasonic and X-ray tomographic imaging of highly contrasting inclusions in concrete specimens,* Proceedings of GeoFrontier 2005 Conference

[52] Landis, E.N., *Towards a physical damage variable for a heterogeneous quasi-brittle material*, Proceedings of 11th International Conference on Fracture, Turin, March 20-25, 2005, p. 1150

[53] Damhof, F., Brekelmans, W.A.M., Geers, M.G.D., *Non-local modeling of thermal shock damage in refractory materials,* Eng. Fract. Mech., 2008, Vol. 75, pp. 4706-472

[54] Chaboche, J.L., *Continuum damage mechanics: Part I – General concepts*, J. of Appl. Mech., 1988, Vol. 55, pp. 59-64

[55] Nentech, W., Meftah. F., Reynouard, J.F., *An elasto-plastic damage model for plain concrete subjected to high temperatures,* Eng. Struct., 2002, Vol. 24, pp. 597-611

[56] Luccioni, B.M., Figueroa, M.I., Danesi, R.F., *Thermo-mechanic model for concrete exposed to elevated temperatures*, Eng. Struct., 2003, Vol. 25, pp. 729-742

[57] Gawin, D., Majorana, C.E, Schrefler, B.A., *Numerical analysis of hygro-thermal behaviour and damage of concrete at high temperature*, Mech. of Coh.-Frict. Mat., 1999, 4, pp. 37-44
[58] Hasselman, D. P. H., *Thermal stress resistance parameters for brittle refractory ceramics: a compendium,* Am. Cer. Soc. Bull., 1970, Vol. 49(12), pp. 1033-1037
[59] Carslaw, H.S., Jaeger, J.C., *Conduction of heat in solids,* 1959, pp. 60-61,Oxford University Press
[60] Andreev, K., Harmuth, H., *Application of finite element modeling to the thermo-mechanical behaviour of refractories*, Finite Elements in Civil Engineering Applications, 2002, pp. 61-66, Eds. Hendriks, Rots
[61] Andreev, K., Harmuth, H., *FEM simulation of the thermo-mechanical behaviour and failure of refractories – a case study*, J. of Mat. Processing, 2003, Vol. 143,144, pp. 72-77
[62] Loeb, A.L., *Thermal conductivity: VIII, A theory of thermal conductivity of porous materials*, J. Am. Cer. Soc., 1954, Vol. 37(2), pp. 96-99
[63] Aly, F., Semler, C.E., *Prediction of refractory strength using non-destructive sonic measurements*, Am. Cer. Soc. Bull., 1985, Vol. 64(12), pp. 1555-1558

4. Non-local modelling of cyclic thermal shock damage including parameter estimation

In this paper, rate dependent evolution laws are identified and characterized to model the mechanical (elasticity-based) and thermal damage occurring in coarse grain refractory material subject to cyclic thermal shock. The mechanisms for elasticity driven damage induced by temperature gradients and thermal damage induced by isotropic thermal expansion are combined and represented by a single variable for the total damage. The constitutive model includes the shielding of micro-structural thermal damage by the non-local elasticity-based damage induced at the macroscopic and microscopic scale. Quasi-stationary thermal experiments are used to identify the parameters used in the evolution law for thermal damage. The remaining model parameters, including a micro-structural length scale, are quantified by inverse modelling of cyclic thermal shock experiments. Longitudinal wave propagation measurements through damaged material are simulated, enabling the identification on the basis of the first and second thermal shock cycle. A third thermal shock cycle was performed to evaluate the quality of the obtained parameter set. The set-up of the thermal shock experiments has been optimized through a parameter identifiability analysis. The damage evolution in three consecutive thermal shock cycles is investigated numerically with the optimized model.

4.1 Introduction

Refractory materials in high temperature installations for iron and steelmaking are subject to wear due to thermal shock loading, e.g. induced by the pouring of molten steel into a cold ladle, or the sudden opening of an operating furnace (exposing the hot refractory material to ambient air). High thermal gradients result which may induce excessive stresses and the overall failure of the refractory lining.

To model the mechanical impact of thermal shock, a non-local thermo-mechanical damage framework was proposed in previous work [1]. Both elasticity driven damage due to temperature gradients (at the macro and micro scale) and microscopic thermal damage due to locally non-uniform thermal expansion contributed to the total damage. The interaction between both

Based on: F. Damhof, W.A.M. Brekelmans, M.G.D. Geers., Non-local modelling of cyclic thermal shock damage including parameter estimation, to be submitted

damage mechanisms has been observed from the results of dedicated experiments involving both homogeneous thermal damage and heterogeneous cyclic thermal shock damage [2].

Identification of the parameters of non-local damage models for coarse grain continua can in general only be pursued by inverse modelling of particular experiments in which the investigated material behavior is triggered. The minimization of a predefined error between the experimental and numerical results renders the unknown model parameters. The information extracted from the experimental data should enable a well-posed quantification of the model parameters, assuming that the model error is sufficiently small.

Various authors reported on the qualitative validation of quasi-brittle thermo-mechanical damage frameworks by modelling of high temperature mechanical tests [3-5] or by reproducing representative experiments [6-8]. However, the large number of model parameters in a temperature-dependent damage framework hampers a reliable quantification by inverse modelling. This may explain the lack of published work on this subject.

Parameter identification in the context of isothermal (non-local) damage models by inverse modelling has been reported extensively. The length scale of a non-local continuum can be determined directly from dedicated mechanical tests [9]. The well-posed quantification of multiple unknown model parameters requires the use of local data, e.g. local displacement or strain fields [10-12]. The use of data from multiple mechanical tests involving size-effects [13], [14] is also generally accepted, possibly combined with local data [11]. The reproduction of load-displacement curves from a single test [15] does not suffice neither does the modelling of a one-dimensional mechanical test for the calibration of a two-dimensional model [16].

A large number of mechanical tests with multiple congruent sample geometries needs to be performed to trigger the size effect [13], [14]. A generally unacceptable number of tests is thus required to optimize a temperature-dependent damage model. It is furthermore not possible to adequately simulate the transient propagation of thermal shock damage by a series of quasi-stationary iso-thermal mechanical tests. To remedy these concerns, (time dependent) local measurements as discussed in e.g. [12] may be performed. However, at higher temperatures reliable experiments are far from trivial. The well-posed identification of parameters of a transient non-local thermo-mechanical damage model is therefore a challenging task.

This paper proposes a solution by modelling the damage growth in a refractory material subject to cyclic thermal shock, making use of rate dependent evolution laws for the interacting elasticity-based and thermal damage to properly capture the evolution in a cyclic loading process. Rate dependent evolution of thermal damage including the shielding by elasticity-based damage has not been described before in the literature. Based on experimental observations it is assumed that the extension of micro-cracks induced by thermal damage is obstructed by the elasticity-based damage present at both the macro and micro scale. The damage evolution laws are implemented in a non-local thermo-elastic material description [1]. The evolution law for thermal damage was brought into its iso-static form to enable the parameter identification from quasi-stationary thermal experiments. The remaining model parameters including the non-local length scale are estimated by the inverse modelling of cyclic thermal shock experiments. The aforementioned experiments include the characterization of the damage by transit time measurements as discussed in detail in [2]. The numerical-experimental investigation involves three consecutive thermal shock cycles. The objective function used in the Gauss-Newton identification process is constructed on the differences between the transit times measured in the first and second thermal shock cycle and those obtained from the model (reflecting the propagation of longitudinal waves through the damaged material). The proposed optimization of a transient non-local thermo-mechanical damage model based on these transient damage experiments is an original contribution to this field of research. The resulting parameters are validated by the modelling of a third thermal shock cycle. Using a parameter identifiability analysis it is investigated whether the thermal shock experiments can be improved by modifying the acoustic measurement grid. Finally the optimized numerical model is used to investigate the characteristics of the damage evolution in the three consecutive thermal shock cycles.

4.2 Damage experiments

The experiments described in this section have been outlined in detail in previous work [2]. They are only briefly discussed here to clarify the origin of the data to be used in the parameter identification problem.

4.2.1 Thermal damage

Cube-shaped samples of corund refractory material with edges of 50 mm are placed in a furnace and are heated quasi-stationary (2 °C/min.) up to a range of maximum temperatures. Before cooling the samples quasi-stationary (2 °C/min.) down to ambient temperature a dwell time of 120 min. was maintained at the maximum temperature. The applied maximum furnace temperatures were 450 °C, 600 °C, 750 °C and 900 °C, which are all in the range of the temperatures used in the thermal shock experiments in Section 4.2.2.

The damage induced by the thermal load was determined by measuring the transit time of ultrasonic longitudinal waves with 40 mm diameter transducers using a wave frequency of 54 kHz. Measurements were performed between the 3 opposite pairs of face centres of the sample. The average wave velocity V is calculated from the ratio of the transducer distance and the measured transit time. Subsequently the dynamic Young's modulus E_{dyn} is calculated as follows [2]:

$$E_{dyn} = \rho \left[\frac{(1+\nu)(1-2\nu)}{(1-\nu)} \right] V^2 \tag{4.1}$$

where ρ and ν denote respectively the density and Poisson's ratio. The damage is defined as the decrease of the dynamic Young's modulus relative to the undamaged state. Assuming that the density and Poisson's ratio are negligibly affected by the induced micro-cracks [17], the thermal damage d_{th} is calculated according to:

$$d_{th} = 1 - \frac{t_0^2}{t^2} \tag{4.2}$$

where t and t_0 denote the transit times in the damaged and undamaged state, respectively. The experimental damage results will be presented in Section 4.4.1.

4.2.2 Thermal shock damage

corund refractory samples, initially at ambient temperature, were put into surface contact with molten aluminium, maintained at a temperature of 1000 °C in an open induction furnace. After a heating period of 20 min. the samples were passively cooled in ambient air. The samples were subjected to three consecutive thermal shock cycles (indicated as C1, C2 and C3).

Except for the quenched side all sample sides were thermally insulated, triggering a nearly one-dimensional temperature field as encountered in thick-walled refractory linings of steelmaking installations. The insulation was removed from the samples to enable the measurement of damage after every thermal shock cycle by transit time measurements with transducers of 20 mm diameter using a wave frequency of 200 kHz. The transducer measurement grid is presented in Fig. 4.1. Every line intersection represents the location of a pair of transducers positioned on opposite pairs of the sample faces in two orthogonal directions. Based on the boundary conditions and sample geometry, it is assumed that a symmetric damage pattern develops with respect to the vertical sample axis. The average results of the transit time measurements indicating the damage are presented in Section 4.4.3.

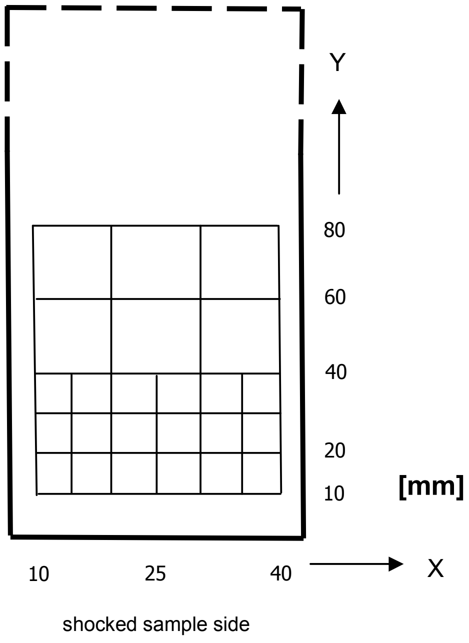

Fig. 4.1. Side view of the transducer measurement grid on one of the sample faces (36 measurement points)

4.3 Material model and solution procedure

A constitutive model is presented to describe the damage growth in coarse grain refractory material subject to consecutive thermal shock cycles. The parameter identification procedure is discussed as well along with the finite element solution used in the inverse analysis. From the computational results the transit time of longitudinal waves propagating through the damaged material is extracted.

4.3.1 Constitutive model

In a refractory material subject to thermo-mechanical loading both the elastic strain tensor $\boldsymbol{\varepsilon}_{el}$ and the thermal strain tensor $\boldsymbol{\varepsilon}_{th}$ contribute to the total strain tensor $\boldsymbol{\varepsilon}$ according to:

$$\boldsymbol{\varepsilon} = \boldsymbol{\varepsilon}_{th} + \boldsymbol{\varepsilon}_{el} \tag{4.3}$$

Thermal strain originates from (isotropic) thermal expansion induced by a temperature increase with respect to a reference state. Elastic strain originates from stresses due to local or global constraints on thermal expansion. The elastic behavior affected by isotropic damage can be described by:

$$\boldsymbol{\sigma} = (1 - D)\,{}^4\boldsymbol{C} : (\boldsymbol{\varepsilon} - \boldsymbol{\varepsilon}_{th}) \tag{4.4}$$

where the damage variable D accounts for both the elasticity-based and the thermal damage. The fourth-order tensor ${}^4\boldsymbol{C}$ is the elasticity tensor of the undamaged material.

During up-quench thermal shock, the elasticity-based damage d_{el} and the thermal damage d_{th} may interact as confirmed experimentally [2]. The total damage D is assumed to be described as a multiplicative combination of both damage mechanisms according to [20]:

$$D = 1 - (1 - d_{el})(1 - d_{th}) \tag{4.5}$$

To model the elasticity-based damage growth a rate dependent evolution law is proposed which is a simplified version of the one proposed in [21] to model fatigue:

$$\begin{aligned} \dot{d}_{el} &= A\left\langle \dot{\bar{\varepsilon}}_{eq} \right\rangle \exp\left(-\boldsymbol{\beta} d_{el}\right) && \text{if } \bar{\varepsilon}_{eq} > \kappa_0 \text{ and } d_{el} < 1 \\ \dot{d}_{el} &= 0 && \text{else} \end{aligned} \tag{4.6}$$

where A and β are material parameters and κ_0 denotes the damage growth threshold value of the non-local equivalent strain $\bar{\varepsilon}_{eq}$. Saturation of elasticity-based damage is triggered by positive values of the material parameter β.

The non-local equivalent strain $\bar{\varepsilon}_{eq}$ is determined implicitly using the following partial differential equation [1], [22]:

$$\bar{\varepsilon}_{eq} - l_c^2 \nabla^2 \bar{\varepsilon}_{eq} = \varepsilon_{eq} + \frac{c_{ths}}{\alpha_{dif}} \left| \dot{T} \right| \tag{4.7}$$

with T the temperature. The role of the micro-structure is represented by the internal length scale parameter l_c. The thermal diffusivity is represented by α_{dif} (defined as $\lambda / \rho C_p$, with λ the thermal conductivity, ρ the density and C_p the thermal capacity) and c_{ths} denotes a material parameter. The second part in the right-hand side of Eq. (4.8) represents the effect of fine scale deformations due to local mismatches at the micro level. The local equivalent strain ε_{eq} is an equivalent strain measure that triggers the damage at the continuum level, determined by [22]:

$$\varepsilon_{eq} = \frac{\eta - 1}{2\eta(1 - 2v)} J_1 + \frac{1}{2\eta} \sqrt{\left(\frac{\eta - 1}{1 - 2v}\right)^2 J_1^2 + \frac{6\eta}{(1 + v)^2} J_2} \tag{4.8}$$

In here, η is the ratio of the compressive and tensile strength of undamaged material, J_1 and J_2 are invariants of the elastic strain tensor $\boldsymbol{\varepsilon}_{el}$:

$$J_1 = \mathrm{tr}\left(\boldsymbol{\varepsilon}_{el}\right) \qquad J_2 = \mathrm{tr}\left(\boldsymbol{\varepsilon}_{el} \cdot \boldsymbol{\varepsilon}_{el}\right) - \frac{1}{3} \mathrm{tr}^2\left(\boldsymbol{\varepsilon}_{el}\right) \tag{4.9}$$

Compared to the average damage occurring in the thermal shock experiments described in Section 4.2.2, the damage attained in dedicated uniform damage experiments (Section 4.2.1) is high [2]. The material degradation in thermal shock experiments is due to both elasticity-based and thermal damage, where the latter is of microscopic origin (induced by small-scale thermal expansion mismatches [1]). In the quasi-stationary uniform damage experiments the material degradation is solely due to thermal damage. Elasticity-based damage is absent due to the low temperature gradients. In a material subject to thermal shock, the micro-crack growth induced by thermal damage may stagnate, whereby progressing micro-cracks collapse into the elasticity-based damage present at both the microscopic and continuum level. Taking into account this shielding mechanism induced by the elasticity-based damage, the following evolution law is proposed for the thermal damage:

$$\begin{aligned} &\dot{d}_{th} = B\left\langle \dot{T} \right\rangle \exp\left(-\gamma\, d_{th}\right)\left(1 - d_{el}^{\phi}\right) && \text{if } T > T_0 \text{ and } d_{th} < 1 \\ &\dot{d}_{th} = 0 && \text{else} \end{aligned} \qquad (4.10)$$

where B and γ are material parameters and T_0 denotes the damage growth threshold value for the temperature T. Saturation of thermal damage is triggered by positive values of the material parameter γ. The parameter $\phi > 0$ controls the level of shielding by the elasticity-based damage.

The presented constitutive framework is implemented in a Galerkin based thermo-mechanical finite element code discussed in detail in [1]. To this end, the evolution laws for elasticity-based and thermal damage are discretized in time using a backward-Euler scheme.

4.3.2 Parameter identification procedure

The unknown model parameters are stored in the column $\underset{\sim}{\theta}$, to be identified by the minimization of an objective function $J(\underset{\sim}{\theta})$. Point of departure is the assumption that the model of the material behaviour triggered in the damage experiments is sufficiently accurate to neglect the influence of the model error. The experimental observations and corresponding model response are stored in the respective columns $\underset{\sim}{m}$ and $\underset{\sim}{h}(\underset{\sim}{\theta})$ defined as:

$$\underset{\sim}{m} = \begin{bmatrix} m_1 \\ \ldots \\ m_n \end{bmatrix} \qquad \underset{\sim}{h}(\underset{\sim}{\theta}) = \begin{bmatrix} h_1(\underset{\sim}{\theta}) \\ \ldots \\ h_n(\underset{\sim}{\theta}) \end{bmatrix} \tag{4.11}$$

where the index n denotes the number of measured and calculated responses involved in the identification process. The objective function $J(\underset{\sim}{\theta})$ is defined as:

$$J(\underset{\sim}{\theta}) = (\underset{\sim}{m} - \underset{\sim}{h}(\underset{\sim}{\theta}))^T (\underset{\sim}{m} - \underset{\sim}{h}(\underset{\sim}{\theta})) \tag{4.12}$$

This definition implies that each of the experimental observations is considered equally relevant. A Gauss-Newton algorithm is used to minimize the objective function. This results in the following iterative scheme for updates $\delta \underset{\sim}{\theta}$ of the parameter set $\underset{\sim}{\theta}$ [10], [23], [24]:

$$\delta \underset{\sim}{\theta} = \underline{K}^{(i\text{-}1)^{-1}} \underline{H}^{(i\text{-}1)} (\underset{\sim}{m} - \underset{\sim}{h}^{(i-1)}) \tag{4.13}$$

$$\underline{H}^{(i-1)} = \frac{\partial \underset{\sim}{h}^{(i-1)}}{\partial \underset{\sim}{\theta}} \tag{4.14}$$

$$\underline{K}^{(i-1)} = \underline{H}^{(i-1)^T} \underline{H}^{(i-1)} \tag{4.15}$$

$$\underset{\sim}{\theta}^{(i)} = \underset{\sim}{\theta}^{(i-1)} + \psi \, \delta \underset{\sim}{\theta} \tag{4.16}$$

where $\underset{\sim}{h}^{(i-1)}$ is the abbreviated notation for the model response $\underset{\sim}{h}(\underset{\sim}{\theta}^{(i-1)})$. The parameter updates are scaled by a numerical damping factor ψ $(0 < \psi < 1)$, commonly used to stabilize the convergence [23]. Small values of the damping factor are to be used if it is expected that small variations in the model parameters may result in a large variation of the model response. The matrix $\underline{H}$ represents the sensitivity of the model response to parameter variations. It is obtained by perturbation of each parameter with respect to the updated parameter set from the previous iteration. The elements of the sensitivity matrix are calculated using a conventional finite difference approach [24]. A regular identifiability matrix $\underline{K}$ is required to calculate the parameter updates $\delta \underset{\sim}{\theta}$. The iteration process is stopped when the convergence criterion is satisfied, expressed according to the relation:

$$\frac{J^{(i)}(\underset{\sim}{\theta}) - J^{(i-1)}(\underset{\sim}{\theta})}{J^{(i-1)}(\underset{\sim}{\theta})} < 10^{-4} \tag{4.17}$$

The parameter identifiability is represented by the condition number of the matrix $\underline{K}$ [23]. Values less than 100 imply a robust parameter identification. Higher values may indicate a linear dependency between columns of the sensitivity matrix $\underline{H}$ due to correlated parameters. To enhance the parameter identifiability the condition number of the identifiability matrix can be improved for every Gauss-Newton iteration. To this end the iterative system (4.13) to (4.16) is written into a dimensionless format using a diagonal matrix $\underline{R}$. Its elements R_{jj} with the index j ranging from 1 to p, the number of unknown parameters, are defined as the ratio of the reference values θ_j^R ($\neq 0$) of the parameters θ_j and the reference value h^R ($\neq 0$) of the model response h. A single reference values suffices for the model response as only one type of measurement is involved in the inverse analysis. The resulting dimensionless sensitivity matrix $\underline{H}^*$ and identifiability matrix $\underline{K}^*$ are defined as:

$$\underline{H}^* = \underline{H}\,\underline{R} \tag{4.18}$$

$$\underline{K}^* = \underline{H}^{*T}\,\underline{H}^* \tag{4.19}$$

In full the dimensionless sensitivity matrix $\underline{H}^*$ reads:

$$\underline{H}^{*} = \begin{bmatrix} \dfrac{\partial h_1}{\partial \theta_1}\dfrac{\theta_1^R}{h^R} & \cdots & \dfrac{\partial h_1}{\partial \theta_p}\dfrac{\theta_p^R}{h^R} \\ \cdots & \dfrac{\partial h_k}{\partial \theta_j}\dfrac{\theta_j^R}{h^R} & \cdots \\ \dfrac{\partial h_n}{\partial \theta_1}\dfrac{\theta_1^R}{h^R} & \cdots & \dfrac{\partial h_n}{\partial \theta_p}\dfrac{\theta_p^R}{h^R} \end{bmatrix} \tag{4.20}$$

By using Eqs. (4.18) and (4.19), the iterative system (4.13) to (4.16) can be rewritten into a dimensionless format. The condition number of the matrix $\underline{K}^{*}$ is generally improved through the scaling with the reference values θ_j^R and h^R [25] for every iteration.

The apparent correlation between the material parameters is quantified by correlation coefficients which are the off-diagonal elements C_{ij} of a symmetric correlation matrix $\underline{C}$ defined as [23]:

$$C_{ij} = \frac{P_{ij}}{\sqrt{P_{ii} P_{jj}}} \tag{4.21}$$

where the matrix $\underline{P}$ is the inverse of the identifiability matrix $\underline{K}^{*}$. The values of the correlation coefficients range from -1 to 1 which indicates respectively a fully negative and positive correlation between a pair of parameters. Correlation between a pair of parameters is absent if the governing correlation coefficient equals zero. A pair of two parameters cannot be uniquely identified (and are correlated) if the absolute value of the governing correlation coefficient exceeds 0.9 [14] [25].

4.3.3 Geometry, boundary conditions and discretization

The thermal shock experiments are modelled by taking a quarter of the sample geometry with dimensions width x height x depth of 25 x 150 x 25 mm^3 assuming a symmetric damage pattern with respect to the vertical mid-planes of the sample. For the FE discretization brick elements with 20 nodes are used, discussed in detail in [1]. In the height direction, over a distance of 40 mm from the quenched sample side a mesh density of 2 x 8 x 2 (width x height x depth) elements is used. The other part of the sample is modelled with a mesh density of 2 x 11 x 2 (width x height x depth) elements. Appropriate boundary conditions were applied at the planes of symmetry together with a constrained vertical displacement of the top centre line node to model the sample mounting (and to prevent rigid body motion). At the quenched sample side, the molten aluminium temperature of 1000 °C is prescribed. The remaining sample sides were modelled as thermally insulated. The heating period of 20 minutes is modelled using time steps of 3 s. Due the relatively slow heat transfer ([2], [18]), the damage induced during the cooling period is negligible and is therefore not taken into account.

4.3.4 Calculation of transit time

The dynamic Young's modulus E_{dyn} of damaged sample material is calculated according to:

$$E_{dyn} = (1 - D)E_{dyn,0} \tag{4.22}$$

where $E_{dyn,0}$ is the dynamic Young's modulus in the undamaged state. The damage variable D is defined here as the decrease of the dynamic Young's modulus relative to the initial undamaged state. Substitution of Eq. (4.22) into Eq. (4.1) and subsequent re-arranging renders a relation for the longitudinal wave velocity V in damaged material:

$$V = \sqrt{\frac{(1 - D)E_{dyn,0}(1 - \nu)}{\rho(1 + \nu)(1 - 2\nu)}} \tag{4.23}$$

In [2], it is shown that the damage variable D implicitly defined by Eq. (4.22) is consistent with its static equivalent. Hence, the (static) damage and the wave velocity can be directly determined from the computational results.

The longitudinal wave velocity is calculated at equidistant locations (calculation points) on an imaginary line connecting the transducer positions with a numerical resolution given by the finite element mesh. The wave velocity in a calculation point is determined by interpolation of the nodal wave velocities of a finite element calculated with Eq. (4.23). Eventually the transit time is obtained by summation of the transit times between all calculation points on the considered line, each calculated as the ratio of the distance between two neighbouring calculation points and the corresponding wave velocity.

4.4 Mixed numerical-experimental analysis

4.4.1 Model parameters, identification and validation

Table 4.1 contains the already available model parameters determined from conventional tests. The static and dynamic Young's modulus were respectively determined from three-point bending tests and from transit time measurements performed on undamaged sample material. The estimated value for Poisson's ratio is typical for coarse grain refractory materials. The coefficient of thermal expansion was determined from dilatation tests. The thermal conductivity and capacity were determined from standard measurements in the temperature regime of interest and are specified as functions of the temperature T in °C. The compressive and tensile strength, defining the ratio η, were determined respectively from uniaxial compressive tests and three-point bending tests.

Type	Quantity	Value	Unit
Elastic material parameters	Static Young's modulus	$E_{stat} = 13.0$	GPa
	Dynamic Young's modulus	$E_{dyn} = 26.0$	GPa
	Poisson's ratio	$\nu = 0.22$	[-]
Thermo-elastic material parameter	Thermal expansion	$\alpha_{th} = 8 \cdot 10^{-6}$	$°C^{-1}$
Thermal material parameters	Density	$\rho = 3038$	kg m^{-3}
	Conductivity	$\lambda(T) = 4.29 - 0.0028T + 2 \cdot 10^{-6} T^2$	W m^{-1} $°C^{-1}$
	Capacity	$c_p(T) = 732 + 1.89T - 0.003T^2 + 2 \cdot 10^{-6} T^3 - 7 \cdot 10^{-10} T^4$	J kg^{-1} $°C^{-1}$
Equivalent strain parameter	Compressive/tensile strength	$\eta = 5.69$	[-]

Table 4.1. Available standard material parameters from conventional tests

Table 4.2 contains the damage material parameters that have been determined through other tests. The elasticity-based damage threshold κ_0 is based on the modelling of the thermal shock experiments reported in [26]. Note that this elasticity-based damage threshold is largely exceeded in the tests reported here, which does not make it possible to determine the κ_0 value from the present experiments.

Type	Quantity	Value	Unit
Elasticity-based damage parameter	Damage threshold value	$\kappa_0 = 1 \cdot 10^{-6}$	[-]
Thermal damage parameters	Damage evolution parameters	$B = 2.33 \cdot 10^{-4}$	°C^{-1}
		$\gamma = 0.4$	[-]
	Damage threshold value	$T_0 = 21$	°C

Table 4.2. Estimated damage model parameters not involved in the identification process

Both the elastic and thermal damage initiate at the microscopic level within the granular structure of the sample material. It is therefore assumed that the thermal strain at the initiation of thermal damage equals the elasticity-based damage threshold κ_0. Consequently, the thermal damage threshold T_0 results from the uniform thermal expansion relation:

$$\kappa_0 = \alpha_{th}\left(T_0 - T_i\right) \tag{4.24}$$

where T_i denotes the reference temperature in the unstrained state.

Finally the parameters B and γ can be determined directly on the basis of the thermal damage experiments. To this end Eq. (4.10) is integrated which in the absence of elasticity-based damage yields:

$$d_{th} = \frac{1}{\gamma}\ln\left[\gamma B\left(T_{\max} - T_0\right) + 1\right] \tag{4.25}$$

where $T_{\max}$ denotes the maximum temperature attained in the history. Fig. 4.2 shows the thermal damage as a function of the maximum applied temperature. The trend line is obtained by fitting of the experimental results with the evolution law for thermal damage. It can be observed that considerable damage is induced by the thermal loading. The damage depends nearly linearly on the maximum holding temperature. It appears that the quantified value of T_0 is in agreement with the thermal damage threshold.

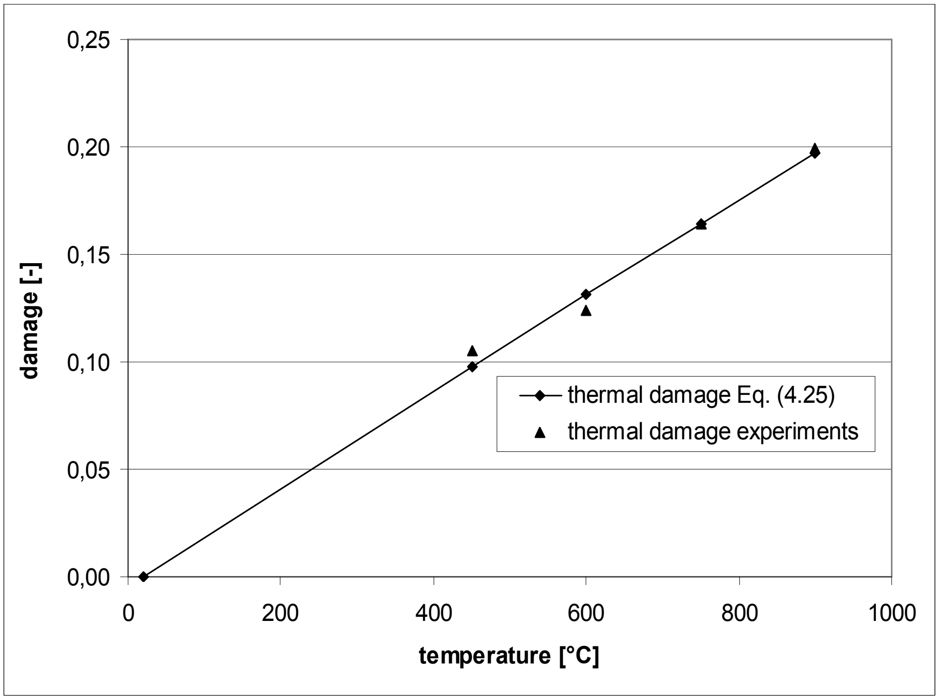

Fig. 4.2. Damage after quasi-stationary heating and cooling

Table 4.3 contains the remaining material parameters A, c_{ths}, l_c, β and ϕ that are determined in the actual identification process. The initial length scale value represents the typical grain size of the sample material [9], [27], [28]. A value of 0.075 is taken as the initial estimate of the shielding constant ϕ. This value effectively prevents that the thermal damage exceeds the elasticity-based damage in the considered experiments. The initial estimates for the remaining parameters A, β and c_{ths} are taken in the expected range that may represent the measured response.

Type	Quantity	Value	Unit
Elasticity-based damage parameters	Damage evolution parameters	$A = 55$	[-]
		$\beta = 2.5$	[-]
	Shielding constant	$\phi = 0.075$	[-]
Non-local material parameters	Length scale	$l_c = 8 \cdot 10^{-3}$	m
	Thermal shock constant	$c_{ths} = 6.3 \cdot 10^{-10}$	$m^2\,°C^{-1}$

Table 4.3. Initial estimates for the damage model parameters involved in the identification process

The material parameters are estimated in four consecutive identification steps numbered 1 to 4. In step 1 the parameter set $\underset{\sim}{\theta} = [A, E_{ths}, c, \beta, \phi]^T$ is identified. The gradient parameter c denotes the square of the length scale l_c. The parameter E_{ths} denotes the parameter c_{ths} divided by the parameter A. It was found that this lowers the governing correlation coefficient, the high value of which is stemming from the contribution $c_{ths}|\dot{T}|/\alpha_{dif}$ to the (rate of the) non-local equivalent strain, the driver of the elasticity-based damage. It appeared that the parameters A and ϕ are correlated in step 1. Consecutively, steps 2 to 4 are performed with fixed values of respectively 0.05, 0.075 and 0.1 for the shielding constant ϕ. The objective function attains a minimum value in step 3.

The parameter values after for each identification step are presented in Table 4.4 including the corresponding value of the objective function $J(\underset{\sim}{\theta})$ and the condition number of the matrix $\underline{K}^*$ averaged over the performed Gauss-Newton iterations. The values obtained for the parameters l_c and β show only small deviations. The experimental data sufficiently triggers the spatial averaging of the local equivalent strain, controlled by the parameter l_c as well as the saturation of the elasticity-based damage, controlled by the parameter β. The parameters A and c_{ths} vary considerably with the selected fixed value of the shielding constant ϕ. For steps 2 to 4 the lowest value of the objective function is obtained in step 3. A more precise minimum and hence more accurate values of the parameters A and c_{ths} may be obtained if additional experimental data is included in the fitting process, see Section 4.4.2. The parameter values obtained in steps 1 and 3 are comparable in value which indicates an adequate robustness of the identification process.

Step	A	c_{ths} [m^2°C^{-1}]	l_c [mm]	β	ϕ	$\underset{\sim}{J}(\theta)$ *10^{-10} [s^2]	cond($\underline{K}^*$)
1	*55.63*	*1*10^{-9}*	*10.8*	*3.70*	*0.069*	*1.30*	*795.64*
2	*70.42*	*8.28*10^{-10}*	*10.9*	*3.62*	*0.05*	*1.34*	*206.13*
3	*50.37*	*1.23*10^{-9}*	*10.7*	*3.72*	*0.075*	*1.30*	*241.44*
4	*26.68*	*2.46*10^{-9}*	*10.6*	*3.82*	*0.1*	*1.31*	*292.62*

Table 4.4. Optimized parameter values and estimation procedure properties

	Step	β	c	ϕ	E_{ths}
A	*1*	*0.23 [0.07]*	*0.43 [0.12]*	*0.92 [0.01]*	*0.82 [0.08]*
	2	*0.23 [0.05]*	*0.54 [0.12]*		*0.72 [0.04]*
	3	*0.21 [0.04]*	*0.62 [0.12]*		*0.76 [0.04]*
	4	*0.19 [0.04]*	*0.70 [0.12]*		*0.80 [0.05]*
E_{ths}	*1*	*0.69 [0.04]*	*0.26 [0.1]*	*0.65 [0.09]*	
	2	*0.82 [0.05]*	*0.10 [0.06]*		
	3	*0.78 [0.06]*	*0.18 [0.08]*		
	4	*0.72 [0.07]*	*0.29 [0.12]*		
ϕ	*1*	*0.17 [0.07]*	*0.20 [0.07]*		
c	*1*	*0.36 [0.04]*			
	2	*0.43 [0.04]*			
	3	*0.41 [0.03]*			
	4	*0.38 [0.03]*			

Table 4.5. Correlation coefficients in steps 1 to 4, average values and standard deviations (in brackets)

The correlation coefficients of steps 1 to 4, averaged over the performed Gauss-Newton iterations, are presented in Table 4.5. The governing correlation coefficients confirm that the five unknown model parameters cannot be estimated independently as opposed to the parameters identified in steps 2 to 4. The parameter identifiability decreases with an increasing fixed value of parameter ϕ as reflected in the value of the condition number. The correlation between the parameter c and the other parameters is relatively low. The information contained in the data of thermal shock experiments seems well suited to quantify the intrinsic length scale of non-locality. The correlation between the parameters A and E_{ths} is relatively high, but still acceptable.

The parameters estimated in steps 1 and 3, normalized by their initial value, are presented as a function of the iteration counter in respectively the left and right part of Fig. 4.3. The correlation between the parameters A and ϕ in step 1 is obvious. Note that in step 3 all the parameters contribute to the minimization of the objective function. The magnitude of the parameter updates early in the fitting process justifies the applied value of the damping factor ψ, see Eq. (4.16).

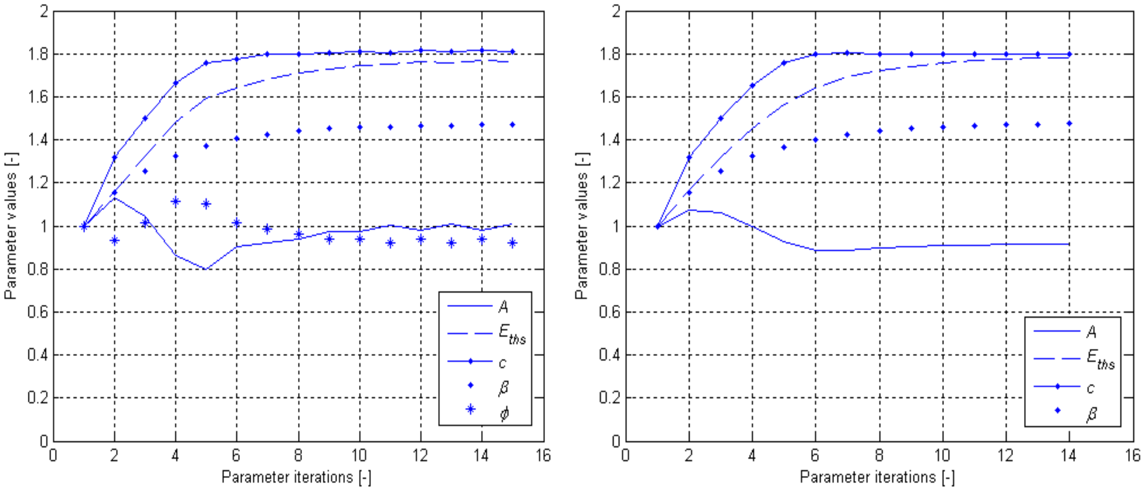

Fig. 4.3. Normalized parameter values in step 1 (left) and in step 3 (right)

The transit times calculated with the model parameters obtained in step 3 are compared with the experimental results in Fig. 4.4. At the Y-coordinates 10, 20 and 30 mm a decreasing damage growth can be observed in consecutive thermal shock cycles. This ‘saturation effect’, which appears to be absent at the Y-coordinates 40, 60 and 80 mm, is ascribed to a redistribution of energy over the network of micro-cracks of which the density increases with every test cycle [2]. This mechanical phenomenon has also been observed in thermal shock experiments on other coarse grain refractory materials [19]. The third thermal shock cycle is now modelled as well to validate the obtained parameter set. At the Y-coordinates 10 mm to 40 mm, the model results compare adequately with the experimental data. At the Y-coordinates 60 mm and 80 mm the results are obviously reasonable for the first and second thermal shock cycle but deviate more for the third cycle. The values of the transit times at these locations approach the undamaged value (16 μs) and the accuracy of the entire procedure (including the model) may not be sufficient enough to capture these differences. Overall it can be stated that a satisfactory numerical-experimental agreement has been obtained.

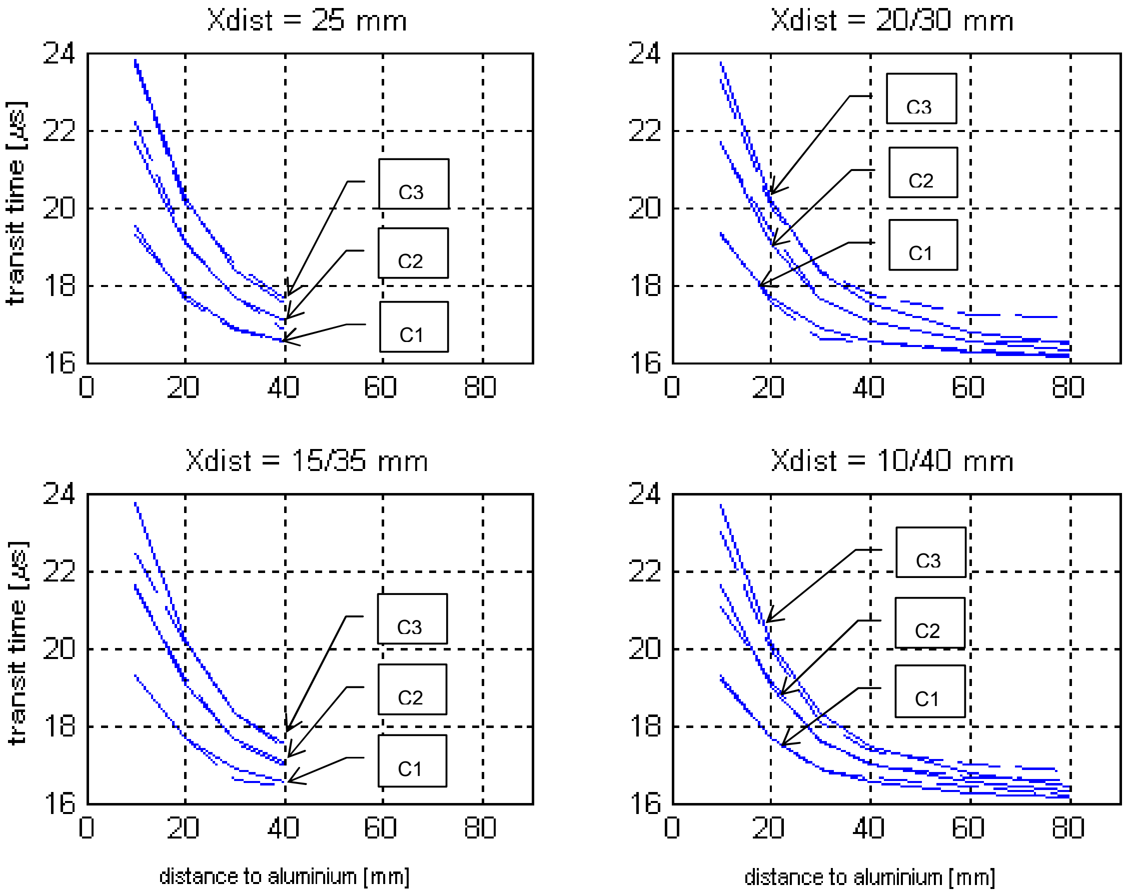

Fig. 4.4. Comparison of measured and calculated transit times with the model optimized in step 3; dashed lines represent measured transit times, solid lines represent calculated transit times

4.4.2 Parameter identifiability analyses

To inversely improve the thermal shock test set-up, the parameter identifiability is investigated as a function of the number and position of the transducers in the measurement grid. To this end the condition number of the matrix $\underline{K}^*$ as well as the corresponding correlation coefficients are calculated for the initial parameter sets as used in steps 1 and 3.

In the first identifiability analysis the vertical distance between the transducer locations is varied. The variable Y-coordinates (see Fig. 4.2) are contained in a column $\underset{\sim 1}{Y}$ which reads:

$$\underset{\sim 1}{Y} = \left[10 \quad 10+\Delta \quad 10+2\Delta \quad 10+3\Delta \quad 10+5\Delta \quad 10+7\Delta \right]^T \tag{4.26}$$

where Δ denotes the variable part of the Y-coordinates. A value of Δ equal to 10 mm represents the transducer locations as applied in the thermal shock experiments. A range of Δ values is used increasing from 2 mm to 18 mm, in steps of 2 mm. It is tacitly assumed that the identification process converges for values of Δ other than 10 mm. The identifiability analysis is repeated with values of the length scale l_c of 4 mm, 6 mm and 10 mm to investigate the influence of the material micro-structure.

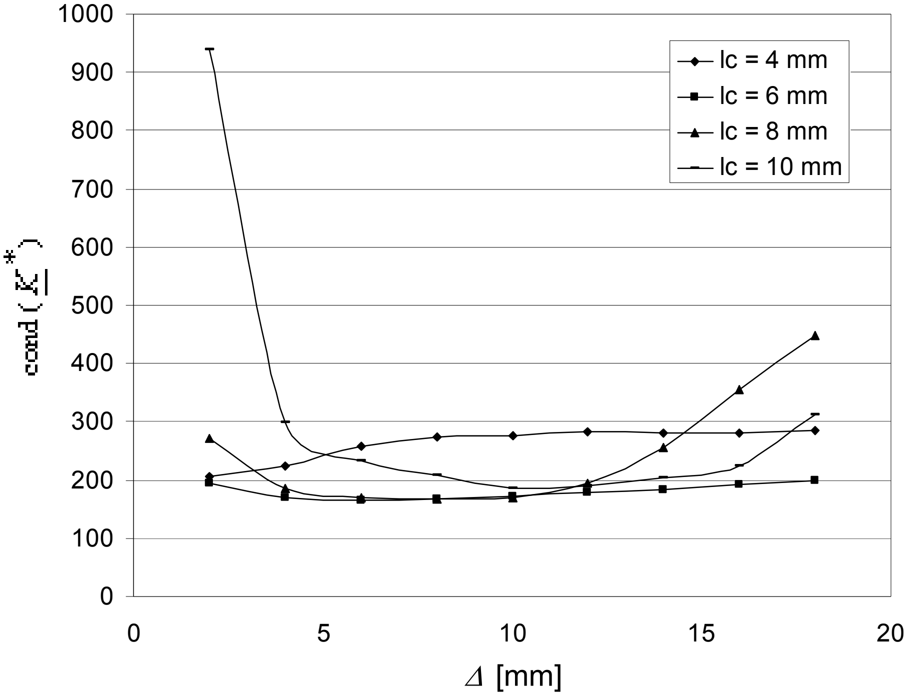

Fig. 4.5. Parameter identifiability as function of the vertical transducer distance

The results, presented in Fig. 4.5, show that optimal values of Δ exist for higher length scale values. The optimal vertical transducer distance increases with an increasing length scale value due to a more evenly distributed non-local equivalent strain and damage over the sample height. It can furthermore be observed (a posteriori) that the transducer positions used in the thermal shock experiments were suitable. The optimal vertical transducer distance aligns with the location of the maximum elasticity-based damage in the sample, see Section 4.3 and [1]. For coarse grain refractory materials (represented by length scale values of 8 mm and 10 mm) it is possible to optimize the measurement set-up by changing the vertical transducer positions. However, to adequately quantify the full set of model parameters (A, c_{ths}, l_c, β and ϕ) the current experimental data set needs to be extended. This is investigated in a second identifiability analysis.

The resolution of the measurement grid is next extended in a second identifiability analysis. The initial grid has transducer positions with the X and Y-coordinates contained in the respective columns $\underset{\sim}{X}_2$ and $\underset{\sim}{Y}_2$ defined as:

$$\underset{\sim}{X}_2 = \begin{bmatrix} 10 & 15 & 20 & 25 & 30 & 35 & 40 \end{bmatrix}^T \tag{4.27}$$

and

$$\underset{\sim}{Y}_2 = \begin{bmatrix} 10 & 15 & 20 & 25 & 30 \end{bmatrix}^T \tag{4.28}$$

Subsequently the grid is extended with a row of 7 transducers positioned at the 35 mm Y-coordinate. In consecutive identifiability analyses the grid is extended in the vertical direction in steps of 5 mm up to a row of transducers positioned at the 120 mm Y-coordinate.

The calculated condition numbers are presented in Fig. 4.6 as a function of the highest Y-coordinate in the grid denoted by $Y_{2,max}$. It can be observed that the parameter identifiability increases considerably up to a value of $Y_{2,max}$ of 100 mm due to the increased number of suitable ‘experimental’ observations involved in the identification process. For grids extended to higher measurement locations the condition number does not decrease significantly anymore due to the low damage level higher in the sample, Section 4.4.3. Table 4.6 contains the absolute value of the calculated correlation coefficients including those of the used experimental grid calculated for the initial parameter set. It can be observed that the correlation coefficients have become acceptable (lower than 0.9) for a grid extended to the 120 mm Y-coordinate. For the grid extended from $Y_{2,max}$ of 30 mm to 120 mm the correlation between the parameters A and ϕ has decreased because of the increased relative contribution of the thermal damage to the total damage at high Y-coordinates. The correlation between the gradient parameter c and the other parameters remains low because the elasticity-based damage is most important in the lower part of the sample. It appears that the condition number is predominantly affected by the decrease of the correlation between the parameters A and ϕ. These results show that in general with a more extended measurement grid it may well be possible to independently quantify the full set of model parameters (A, c_{ths}, l_c, β and ϕ) from the thermal shock experiments. A sufficient number of acoustic measurements then needs to be performed and involved in the inverse analysis. The acoustic grid may be further optimized by using a higher measurement resolution in the lower part of the test sample where high thermal gradients occur.

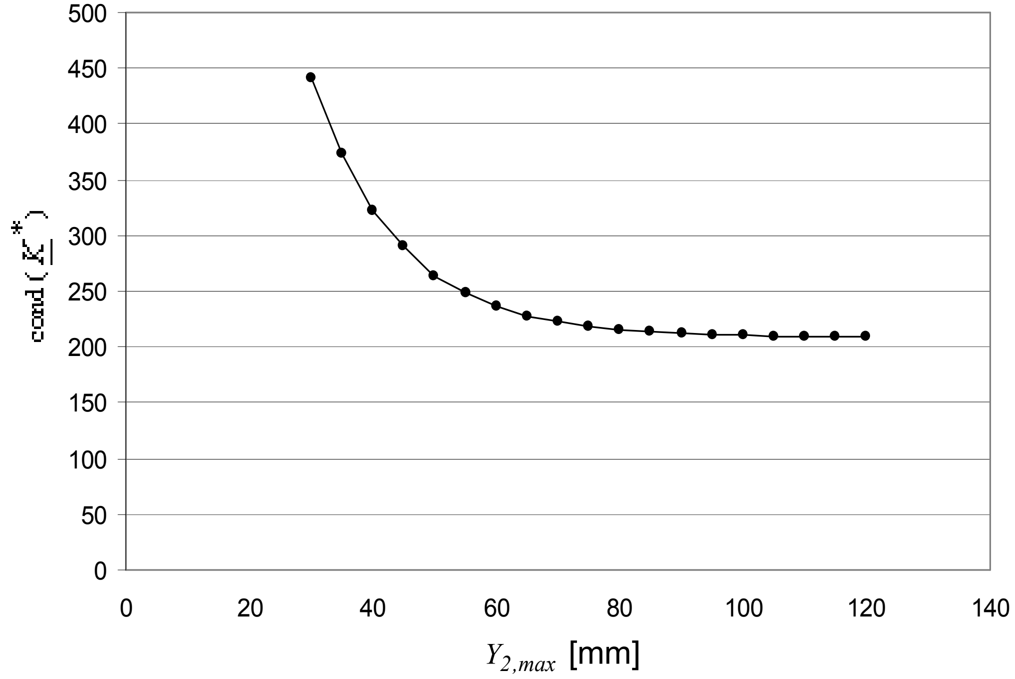

Fig. 4.6. Parameter identifiability as function of the grid extension

	$Y_{2,max}$	β	ϕ	c	E_{ths}
A	*exps*	*0.06*	*0.91*	*0.27*	*0.61*
	30	*0.04*	*0.95*	*0.00*	*0.58*
	120	*0.11*	*0.88*	*0.27*	*0.52*
E_{ths}	*exps*	*0.78*	*0.39*	*0.06*	
	30	*0.80*	*0.42*	*0.24*	
	120	*0.88*	*0.23*	*0.24*	
c	*exps*	*0.06*	*0.09*		
	30	*0.45*	*0.10*		
	120	*0.48*	*0.22*		
ϕ	*exps*	*0.07*			
	30	*0.06*			
	120	*0.11*			

Table 4.6. Correlation coefficients for the actually used experimental grid (indicated with 'exps') and two alternative grids

4.4.3 Damage evolution

The damage evolution in three consecutive thermal shock cycles is assessed with the model identified in the previous subsections. in step 3. The temperature during one cycle and the total damage are shown as a function of time in the left and right part of Fig. 4.7, respectively. The elastic and thermal damage are shown, respectively, in the left and right part of Fig. 4.8. Presented are the results along the vertical sample axis, at the vertical position of the transducers.

It can be observed that at the start of every thermal shock cycle the elasticity-based damage at the Y-coordinates 10, 20 and 30 mm increases stepwise to its end value. This is due to the contact with the molten aluminium which causes nearly instantaneous thermal expansion of the sample. The resulting strain rates are high enough to induce the observed elasticity-based damage increment. At higher sample locations, the described thermal expansion is less prominent and temperature gradients induce a more gradual evolution of the elasticity-based damage. From the comparison between the left parts of Figs. 4.7 and 4.8 it appears that the temperature at all sample locations is still well below 100 °C before the elasticity-based damage has reached its maximum value. The use of temperature-independent parameters to describe the elasticity-based damage evolution suffices for the considered sample locations.

The evolution of the thermal damage follows the temperature increase and hence progresses continuously in every thermal shock cycle. Shielding by elasticity-based damage takes place at the Y-coordinates 10, 20 and 30 mm. Shielding occurs at constant elasticity-based damage and not during a simultaneous growth of elastic and thermal damage. The relative contribution of the thermal damage to the total damage remains nonetheless significant at all Y-coordinates.

It is shown that saturation effects of the thermal damage in the consecutive thermal shock cycles are present at all the sample locations. Note that saturation is defined here as a decrease of the damage growth in consecutive test cycles. A saturation tendency of the elasticity-based damage as such can only be observed at the Y-coordinates 10, 20 and 30 mm. Saturation of the total damage at the higher sample locations is thus stemming from saturation of the thermal damage. Considering the observed saturation of both the thermal and elasticity-based damage it appears that this occurs both at a microscopic and macroscopic scale.

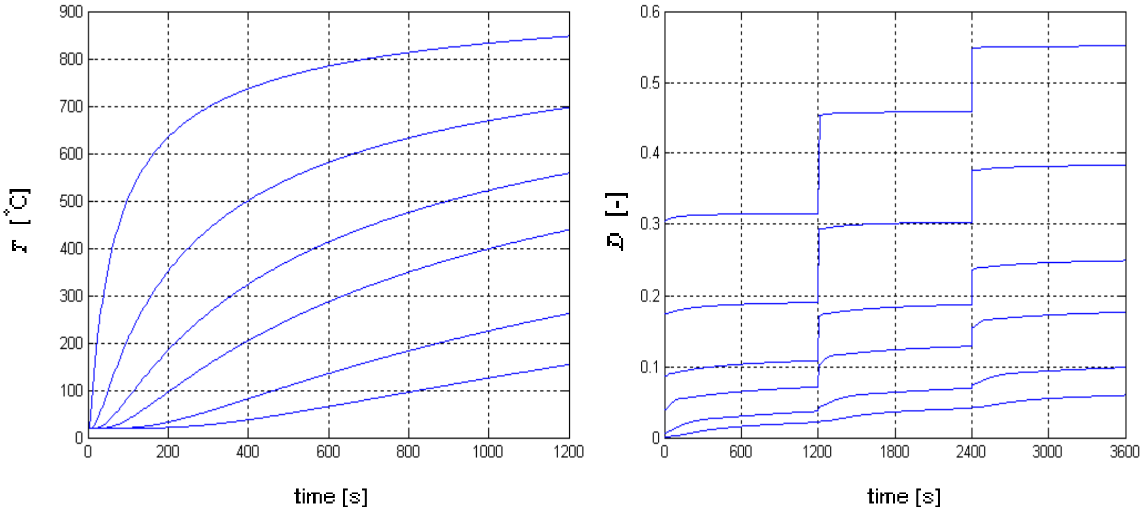

Fig. 4.7. Temperature and total damage at the transducer locations, the curves from top to bottom represent the 10, 20, 30, 40, 60 and 80 mm Y-coordinate respectively

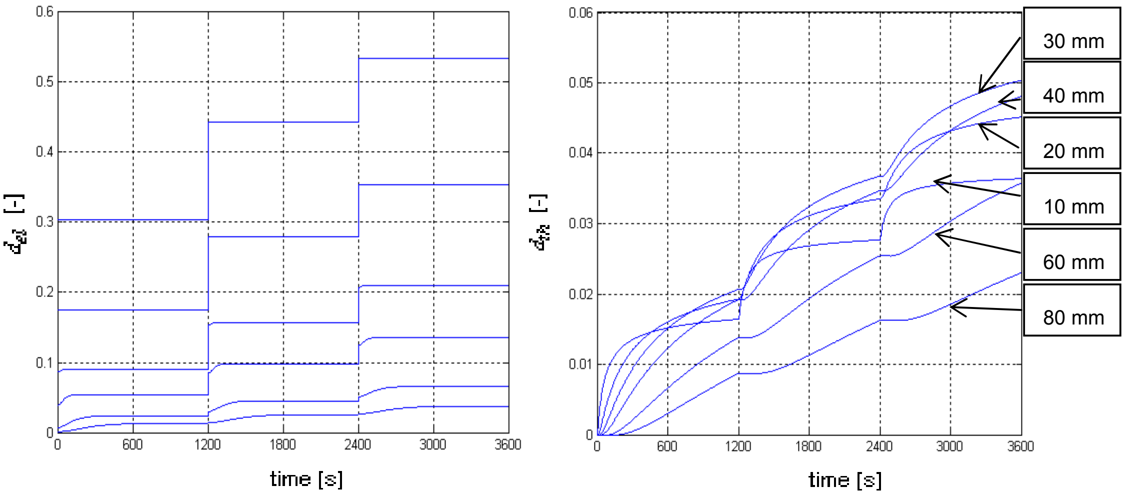

Fig. 4.8. Elastic and thermal damage at the transducer locations, the curves from top to bottom in the left figure represent the 10, 20, 30, 40, 60 and 80 mm Y-coordinate respectively

The local and non-local equivalent strains on the vertical sample axis, at the vertical transducer positions 20 and 80 mm as a function of time are presented in Figs. 4.9 and 4.10, respectively. Only the results during the first thermal shock cycle are shown. The high starting value of the non-local equivalent strain at the 20 mm transducer position is due the corresponding high local equivalent strain rate induced by the thermal expansion at the thermally shocked sample side. The incremental start of the non-local equivalent strain (and elasticity-based damage) at the 80 mm Y-coordinate evolution is also due to the elastic wave induced by the described instantaneous thermal expansion. At both the 20 mm and 80 mm Y-coordinate the non-locality remains important over the entire time-frame. The macroscopic and microscopic contributions to the elasticity-based damage, represented by respectively the equivalent strain ε_{eq} and the term $c_{ths}\left|\dot{T}\right|/\alpha_{dif}$ in Eq. (4.7), are of the same order.

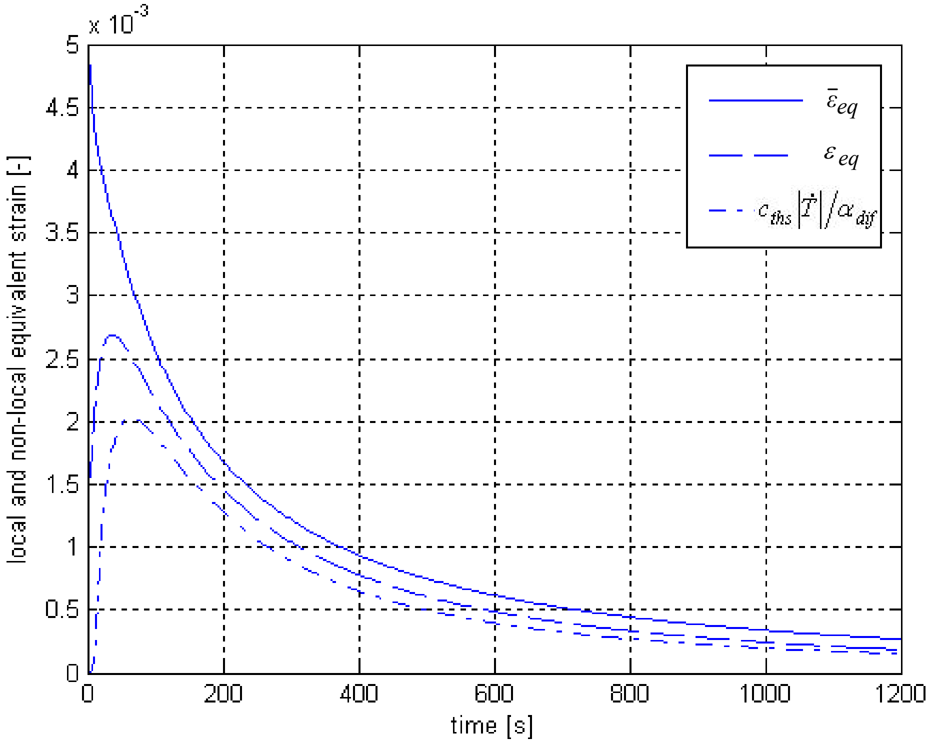

Fig. 4.9. Equivalent strains at the 20 mm Y-coordinate

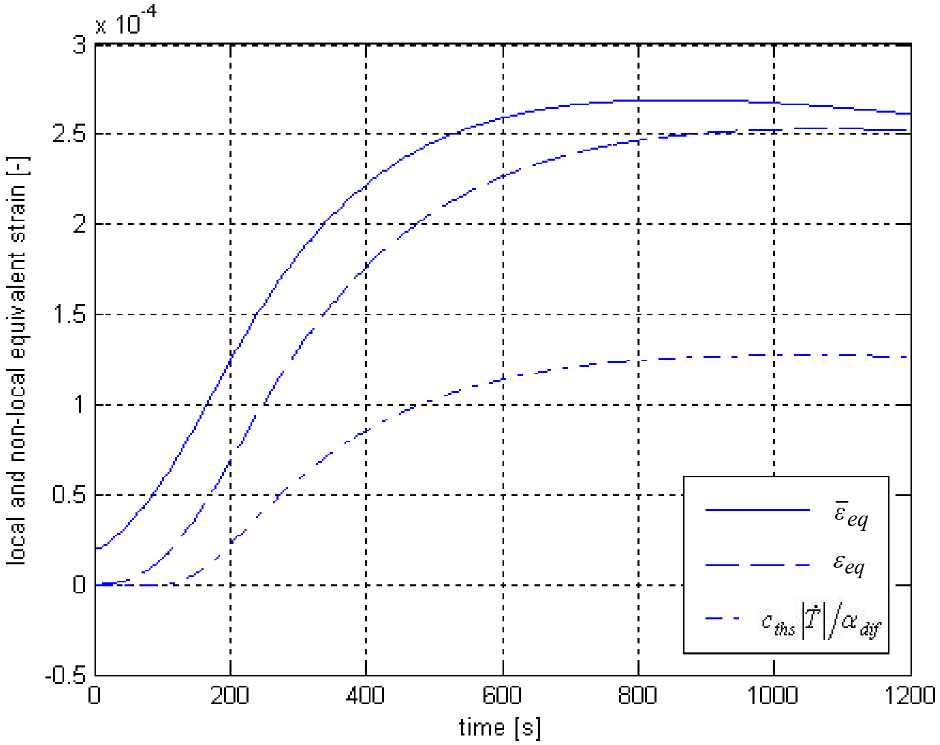

Fig. 4.10. Equivalent strains at the 80 mm Y-coordinate

4.5 Discussion

The discrepancy between model and experiments at the higher transducer locations for the third cycle may be attributed to limitations in accuracy, but possibly also model shortcomings (e.g. degradation processes not fully incorporated in the material model). Thermal conduction for example may be affected by the present micro-cracks induced by thermal shock in a coarse grain refractory material [2], [26]. Locally, this may lead to higher temperature gradients and a correspondingly higher damage. Relations between the thermal conductivity and the damage as proposed by Tzou [29], [30] may be used to incorporate this effect in the present constitutive framework. When the damage is considered as a form of porosity [31] conductivity-porosity relations as introduced in [32-35] can be applied for this purpose. The accuracy of the parameter identification procedure may be further enhanced by the determination of the thermal moduli by inverse modelling of the thermal shock experiments.

The mechanical parameters of the sample material used are independent of the temperature. Refractory materials applied at thermal shock sensitive locations sometimes exhibit a distinctive temperature-dependent (post-)elastic behaviour. Additional experiments are then required to quantify all the corresponding material parameters, required to capture this temperature dependency. Thermal shock experiments could be performed with molten aluminium heated to a range of temperatures combined with thermal damage experiments involving the repeated quasi-stationary heating and cooling of test samples. The independent quantification of all the model parameters by inverse modelling may be facilitated by the incorporation of a second order sensitivity matrix into the identification algorithm. This so-called Hessian matrix is usually approximated using methods as the BFGS algorithm [36]. Additionally the parameter identifiability may benefit from the use of enhanced measurement grids as discussed in Section 4.4.2.

The sensitivity analysis of the thermal shock experiments revealed that the propagation of the elastic shock wave into the sample is caused predominantly by the instantaneous thermal expansion induced by the contact with the molten aluminium. In refractory bricks used in the lining of steelmaking installations, the response to thermal shock may be different due to the constraints imposed by neighbouring bricks. The damage furthermore will depend on the geometry of the brick and the transient thermal boundary conditions (process cycles) acting upon it. The present model can be well used to this purpose, which is the subject of future work.

4.6 Conclusions

The damage in a coarse grain refractory material subject to consecutive thermal shock cycles is analyzed, using a model based on two distinct damage mechanisms and their mutual interaction. The first damage mechanism (elasticity-based damage) originates from internally and externally constrained thermal expansion induced by temperature gradients and is driven by a positive rate of the non-local equivalent strain. The second damage mechanism (thermal damage) is due to a temperature increase and is induced by thermal expansion mismatches at the micro scale. The presented constitutive damage model is implemented into a non-local thermo-mechanical finite element code.

The model parameters have been identified using the results of earlier reported experiments [2], which involved the quasi-stationary heating and cooling of refractory samples (thermal damage) as well as new experiments, involving the repeated contact of ambient temperature refractory samples with molten aluminium followed by passive air-cooling (thermal shock damage). In both experiments the damage was determined from transit time measurements.

The constitutive damage framework presented in this paper, and the presented parameter identification analyses reveal the following original contributions and insights:

- A rate dependent evolution law has been proposed for the elastic and thermal damage. The evolution laws incorporate saturation of the damage with an increasing number of thermal shock cycles as well as shielding of the thermal damage by elasticity-based damage.
- In line with the elasticity-based damage the thermal damage evolution is controlled by a positive temperature rate. The governing material parameters could be identified using the results of thermal damage experiments only.
- The remaining damage material parameters were identified by inverse modelling of the thermal shock experiments. To this end, longitudinal

wave propagation properties through damaged material have been extracted from the numerical results, which enabled the comparison with the measured transit times. The use of a Gauss-Newton minimization procedure enriched with numerical damping resulted in an adequately converging identification process.

- All model parameters could be determined with a reasonable accuracy. Particularly the non-local length scale is triggered by the information contained in the experimental data set. Its identification from transient experiments has not been reported before.
- Parameter identifiability analyses have been used to improve the experimental set-up by extending the currently used measurement grid to the level where the inverse problem becomes well-posed.

The identification process resulted in a satisfactory experimental-numerical comparison of the results for the first and second thermal shock cycle. The third thermal shock cycle was used to validate the obtained parameter set for which some deviations from the experiments could be observed at the transducer locations further away from the shock front. Nonetheless, the observed prediction of the experimental trends quantitatively validates the proposed constitutive damage framework.

Additional results obtained with the quantified model revealed that the elastic (thermal) shock wave propagates nearly instantaneously over a considerable distance into the sample. Temperature gradients influence the elasticity-based damage distribution only at the higher sample locations where macroscopic and microscopic contributions remain of the same order. In spite of considerable shielding by elasticity-based damage the contribution of the thermal damage to the total damage is significant.

4.7 References

[1] Damhof F., Brekelmans W.A.M., Geers M.G.D., *Non-local modelling of thermal shock damage in refractory materials*, Engng. Fract. Mech., 2008, Vol. 75, pp. 4706-4720

[2] Damhof F., Brekelmans W.A.M., Geers M.G.D., *Experimental analysis of the evolution of thermal shock damage using transit time measurement of ultrasonic waves*, J. Eur. Cer. Soc*.,* 2009, Vol. 20, pp. 1159-1167

[3] Tenchev R., Purnell P., *An application of a damage constitutive model to concrete at high temperature and prediction of spalling*, Int. J. Solids Struct*.,* 2005, Vol. 42, pp. 6550-6565

[4] Nentech W., Meftah F., Reynouard J. M., *An elasto-plastic damage model for plain concrete subjected to high temperatures,* Engng. Struct., 2002, Vol. 24, pp. 597–611

[5] Pearce C.J., Nielsen C.V., Bicanic N., *Gradient-enhanced thermo-mechanical damage for concrete at high temperatures including transient thermal creep*, Int. J. Numer. Anal. Methods Geomech., 2004, Vol. 28, pp. 715–735

[6] Fu Y.F., Wong Y.L., Poon C.S., Tang C.A., *Numerical tests of thermal cracking induced by temperature gradient in cement-based composits under thermal loads*, Cement Concr. Comp*.,* 2007, Vol. 29, pp. 103-116

[7] Bary B., Ranc G., Durand S., Carpentier O., *A coupled thermo-hydro-mechanical-damage model for concrete subjected to moderate temperatures*, Int. J. Heat Mass Transfer, 2008, Vol. 51, pp. 2847-2862

[8] Gawin D., Majorana C.E., Schrefler B.A., *Numerical analysis of hygro-thermal behaviour and damage of concrete at high temperature*, Mech. Cohes. Frict. Mater*.,* 1999, Vol. 4, pp. 37–44

[9] Bazant Z.P., Pijaudier-Cabot G., *Measurement of characteristic length of nonlocal continuum*, J. Engng. Mech., ASCE*,* 1989, Vol. 115, pp. 755-767

[10] Geers M.G.D., De Borst R., Peijs T., *Mixed numerical-experimental identification of non-local characteristics of random-fibre-reinforced composites*, Comp. Science Techn., 1999, Vol. 59, pp. 1569-1578

[11] Iacono C., Sluys L.J., Van Mier J.G.M., *Estimation of model parameters in nonlocal damage theories by inverse analysis techniques,* Comput. Methods Appl. Mech. Engng., 2006, Vol. 195, pp. 7211-7222

[12] Geers M.G.D., De Borst R., Brekelmans W.A.M., Peerlings R.H.J., *Validation and internal length scale determination for a gradient damage model: application to short glass-fibre reinforced polypropylene*, Int. J. Solids Struct*.,* 1999, Vol. 36, pp. 2557-2583

[13] Le Bellégo C., Dubé J.F., Pijaudier-Cabot G., Gérard B., *Calibration of nonlocal damage model from size effect tests*, Eur. J. Mech. Solids, 2003, Vol. 22, pp. 33-46

[14] Carmeliet J., *Optimal estimation of gradient damage parameters from localization phenomena in quasi-brittle materials,* Mech. Cohes. Frict. Mater*.,* 1999, Vol. 4, pp. 1–16

[15] Scotta R., Vitaliani R., Saette A., Onate E., Hanganu A., *A scalar damage model with a shear retention factor for the analysis of reinforced concrete structures: theory and validation*, Computers Struct., 2001, Vol. 79, pp. 737-755

[16] Nguyen G.D., Houlsby G.T., *Non-local damage modelling of concrete: a procedure for the determination of model parameters*, Int. J. Numer. Anal. Methods Geomech., 2007, Vol. 31, pp. 867-891

[17] Lemaitre J., Desmorat R., *Engineering Damage Mechanics*, Springer Berlin Heidelberg New York, p. 18, 2005

[18] Damhof F., Tesselaar W., Van den Eynden J.C., *A novel experimental approach to investigate thermal shock damage in refractory materials*, Cer. Forum Int., 2007, Vol. 84, pp. 75-79

[19] Lee W.J., Case E.D., *Comparison of saturation behavior of thermal shock damage in a variety of brittle materials*, Mat. Science Engng., 1992, Vol. A154, pp. 1-9

[20] Willam K., Rhee I., Xi Y., *Thermal degradation of heterogeneous concrete materials*, J. Mat. Civil Engng., 2005, Vol. 17(3), pp. 276-285

[21] Peerlings R.H.J., Brekelmans W.A.M., De Borst R., Geers M.G.D., *Gradient enhanced modelling of high cycle fatigue*, Int. J. Numer. Methods Engng., 2000, Vol. 49, pp. 1547–1569

[22] Peerlings R.H.J., De Borst R., Brekelmans W.A.M., De Vree J.H.P., *Gradient enhanced damage for quasi-brittle materials,* Int. J. Numer. Methods Engng., 1996, Vol. 39, pp. 3391–3403

[23] Beck. J.V., Arnold K.J., *Parameter Estimation in Engineering and Science*, Wiley, New York, 1977

[24] Meuwissen M.H.H., *An inverse method for the mechanical characterization of metals,* Ph.D. Thesis, Eindhoven University of Technology, Eindhoven, The Netherlands, 1998

[25] Geers M.G.D., Baaijens F.P.T., Oomens C.W.J., *Optimization of experiments for the identification of material parameters in computational models.* In Carlomagno G.M., Brebbia C.A., eds., Computational Methods and Experimental Measurements IX, WIT Press, Southampton, Great Britain, 1999

[26] Özdemir I., Brekelmans, W.A.M., Geers M.G.D., *Modelling thermal shock damage in refractory materials via direct numerical simulations,* J. Eur. Cer. Soc., 2010, Vol. 30, pp. 1585-1597

[27] Peyrot I., Bouchard P.O., Bay F., Bernard F., Garcia-Diaz E., *Numerical aspects of a problem with damage to simulate mechanical behavior of a quasi-brittle material*, Comput. Mat. Sci., 2007, Vol. 40, pp. 327-340

[28] Nguyen G.D., *A thermodynamic approach to non-local damage modelling of concrete*, Int. J. Solids Struct., 2008, Vol. 45, pp. 1918-1934

[29] Tzou D.Y., Chen E.P., *Overall degradation of conductive solids with mesocracks*, Int. J. Heat Mass Trans*.,* 1990, Vol. 33(10), pp. 2173-2182

[30] Tzou D.Y., Li J., *The overall thermal conductivity in a straining body with microcrack evolution*, Int. J. Heat Mass Trans., 1993, Vol. 36(16), pp. 3887-3895

[31] Kachanov L.M., *Introduction to Continuum Damage Mechanics,* Martinus Nijhoff Publishers, Dordrecht, The Netherlands, 1986

[32] Loeb A.L., *Thermal conductivity: VIII, A theory of thermal conductivity of porous materials*, J. Am. Cer. Soc., 1954, Vol. 37, pp. 96-99

[33] Dos Santos W.N*., Effect of moisture and porosity on the thermal properties of a conventional refractory concrete*, J. Am. Cer. Soc., 2003, Vol. 23, pp. 745-755

[34] Dos Santos W.N., *Effect of porosity on the thermal conductivity of alumina,* High Temperatures-High Pressures, 1993, Vol. 25, pp. 89-98

[35] Zivcova Z., Gregorova E., Pabst W., Smith D.S., Michot A., Poulier C., *Thermal conductivity of porous alumina ceramics*, J. Eur. Cer. Soc., 2009, Vol. 29, pp. 347-353

[36] Gill P.E., Leonard M.W., *Reduced-Hessian quasi-Newton methods for unconstrained optimization*, SIAM J. Optim., 2001, Vol. 12(1), pp. 209-237

5. Predictive analysis of thermal shock damage in steelmaking installations

A temperature-dependent constitutive damage framework is coupled incrementally with a thermo-elastic FE package to model transient thermo-mechanical damage and thermal shock in the refractory lining of steelmaking installations. Both non-local elasticity-based damage induced by temperature gradients and thermal damage induced by a uniform temperature increase contribute to the total damage. The non-locality is spatially discretized using a Galerkin approach within a finite element context. A backward-Euler scheme is used for time integration of the non-locality as well as the rate-dependent damage evolution laws. The proposed operator-split strategy enables the modelling of thermal shock damage in high temperature installations subject to process conditions. The computational platform is demonstrated with numerical examples involving thermal shock in a snorkel of a steel degassing installation and in the refractory lining of a steel ladle.

5.1 Introduction

The refractory lining of installations for steelmaking is subject to wear due to thermal shock. This occurs for example when molten steel is introduced into a cold ladle or when the doors of an operating furnace are suddenly opened and the hot refractory material becomes exposed to cold air. Severe thermal gradients and stresses are thus induced, possibly resulting in the loss of the structural integrity of the refractory lining which compromises the exploitation of the high temperature installation. Computer models can be used for a predictive assessment of this material failure, in the design phase as well as afterwards in a post-failure analysis. The complex geometry of the refractory structure as well as the transient process conditions need to be incorporated in such numerical models together with an appropriate constitutive framework to realistically predict the material degradation.

Thermal shock in refractory materials has been accounted for in the past using e.g. the thermal shock resistance parameters defined by Hasselman [1-3] as well as analytical models based on fracture mechanics [4-6]. Multi-scale models of refractory materials [7-10] have been developed more

Based on: Damhof F., Brekelmans W.A.M., Geers M.G.D., *Predictive analysis of thermal shock damage in steelmaking installations*, to be submitted

recently and are particularly useful in materials development. In previous work [11], a continuum damage framework has been proposed to model thermal shock in coarse grain refractory materials. The damage description includes non-local elasticity-based damage due to constrained thermal expansion induced by temperature gradients at the continuum scale and due to fine scale deformations induced by thermal transients at the micro-scale. Thermal damage due to local mismatches at the micro-level, experiencing temperature increase is also included in the constitutive damage framework. The phenomenological relevance of the model was assessed by the numerical simulation of a thermal shock experiment involving the contact of ambient temperature refractory samples with molten aluminium followed by a down quench in ambient air. The experimental damage was characterized by location-dependent acoustic measurements. The evolution of thermal shock damage in a consecutive series of these experiments is described in [12], including quasi-stationary thermal tests to trigger the thermal damage. It appeared that the micro-crack growth induced by the thermal damage growth was obstructed by the elasticity-based damage. Rate-dependent equations of damage evolution were proposed in [13] to model the damage evolution observed in the performed experiments. The damage framework was validated quantitatively by inverse modelling of the cyclic thermal shock experiments described in [12].

In refractory engineering, thermal shock has been analyzed elastically by considering either installation parts of [14-16] or entire high temperature installations [17], [18]. Models incorporating plasticity [19-22], discrete fracture mechanics [23-25] as well as smeared cracking [26], [27] have also been proposed for this purpose. In the literature the modelling of thermo-mechanical damage in engineering applications is mostly limited to simplified geometries [28-30] with [31] as an exception. Non-local damage approaches to account for the coarse nature of the refractory micro-structure have only been used in [30] to model the damage in a single refractory material.

An operator-split strategy is proposed in this paper to model transient thermo-mechanical damage and in particular thermal shock in the refractory lining of steelmaking installations. The non-local temperature-dependent damage framework described in [13] is coupled incrementally with a thermo-mechanic FE package, enabling the analysis of thermally loaded structures with transient thermal boundary conditions. The extended non-locality equation is discretized using a Galerkin approach within a finite element context. A backward-Euler scheme is used for time integration of the non-locality as well as the rate-dependent damage evolution laws. The use of a non-local thermo-mechanical damage model for high temperature installations has not been reported before. The operator-split approach is demonstrated with numerical examples. First, the thermal shock damage in the snorkel of a steel degassing installation is analyzed and the effect of a modification in the process conditions is investigated. A second numerical example deals with the thermal shock damage in the refractory lining of a steel ladle.

5.2 Computational aspects

The constitutive damage model is described here briefly. Details can be found in previous work [13].

5.2.1 Constitutive damage model

In thermo-mechanically loaded refractory material both the elastic strain tensor $\boldsymbol{\varepsilon}_{el}$ and thermal strain tensor $\boldsymbol{\varepsilon}_{th}$ contribute to the total strain tensor $\boldsymbol{\varepsilon}$ according to:

$$\boldsymbol{\varepsilon} = \boldsymbol{\varepsilon}_{th} + \boldsymbol{\varepsilon}_{el} \tag{5.1}$$

The thermal strain is induced by uniform thermal expansion due to a temperature increase with respect to a reference state. The elastic strain is due to non-uniform or internally constrained thermal expansion induced by internal temperature gradients or by neighbouring bricks. Elastic behaviour affected by isotropic damage is defined as follows:

$$\boldsymbol{\sigma} = (1 - D)\,{}^{4}\boldsymbol{C} : (\boldsymbol{\varepsilon} - \boldsymbol{\varepsilon}_{th}) \tag{5.2}$$

where the damage variable D incorporates both elasticity-based damage d_{el} and thermal damage d_{th}. The fourth-order tensor ${}^{4}\boldsymbol{C}$ contains the temperature-dependent elastic moduli of the undamaged material. The expression for the total damage D accounts for the interaction of the elasticity-based and the thermal damage [32]:

$$D = 1 - (1 - d_{el})(1 - d_{th}) \tag{5.3}$$

The evolution law for the elasticity-based damage reads:

$$\begin{aligned} \dot{d}_{el} &= A\left\langle \dot{\bar{\varepsilon}}_{eq} \right\rangle \exp\left(-\beta d_{el}\right) && \text{if } \bar{\varepsilon}_{eq} > \kappa_0 \text{ and } d_{el} < 1 \\ \dot{d}_{el} &= 0 && \text{else} \end{aligned} \tag{5.4}$$

where A and β are material parameters and κ_0 denotes the threshold value for the non-local equivalent strain $\bar{\varepsilon}_{eq}$ implicitly defined by:

$$\bar{\varepsilon}_{eq} - l_c^2 \nabla^2 \bar{\varepsilon}_{eq} = \varepsilon_{eq} + \frac{c_{ths}}{\alpha_{dif}} \left| \dot{T} \right| \tag{5.5}$$

where l_c is an internal length scale that is closely related to the dimensions of the micro-structure of the material. The coefficients c_{ths} and α_{dif} denote a material constant and the thermal diffusivity respectively. The second term on the right-hand side represents fine scale damage due to transient temperature gradients at the micro-scale. The extension of the non-locality equation as used in [33] with this transient microscopic damage is described in detail in [11]. The local equivalent strain is denoted by ε_{eq} and calculated with the modified Von Mises definition [33]:

$$\varepsilon_{eq} = \frac{\eta - 1}{2\eta(1 - 2\nu)} J_1 + \frac{1}{2\eta} \sqrt{\left(\frac{\eta - 1}{1 - 2\nu}\right)^2 J_1^2 + \frac{6\eta}{(1 + \nu)^2} J_2} \tag{5.6}$$

where η is the ratio of the compressive and tensile strength, ν denotes Poisson's ratio and J_1 and J_2 are invariants of the elastic strain tensor $\boldsymbol{\varepsilon}_{el}$ defined by:

$$J_1 = \mathrm{tr}\left(\boldsymbol{\varepsilon}_{el}\right), \; J_2 = \mathrm{tr}\left(\boldsymbol{\varepsilon}_{el} \cdot \boldsymbol{\varepsilon}_{el}\right) - \frac{1}{3} \mathrm{tr}^2\left(\boldsymbol{\varepsilon}_{el}\right) \tag{5.7}$$

The evolution law for the thermal damage includes a term to account for the shielding by elasticity-based damage and is defined as follows:

$$\begin{aligned} \dot{d}_{th} &= B\left\langle \dot{T} \right\rangle \exp\left(-\gamma d_{th}\right)\left(1 - d_{el}^{\phi}\right) && \text{if } T > T_0 \text{ and } d_{th} < 1 \\ \dot{d}_{th} &= 0 && \text{else} \end{aligned} \tag{5.8}$$

where B and γ are material parameters and T_0 denotes the threshold value for the temperature T. The level of shielding by elasticity-based damage is controlled by the parameter $\phi > 0$.

5.2.2 Operator split strategy

A commercial FE package is used to perform the thermo-mechanical analysis in a staggered mode. First the transient temperature field is calculated for the entire time frame considered. During the subsequent mechanical analysis the damage is calculated in a dedicated (development) FE code at every time step, using Eqs. (5.3) to (5.8). To this end the governing temperatures and elastic strains, calculated incrementally in the commercial FE-code, are imported into the user code as well as the corresponding finite element mesh. Young's modulus affected by damage is averaged per element and returned to the commercial FE code, enabling the mechanical calculation in the subsequent time step.

To calculate the non-local equivalent strain, Eq. (5.5) is rewritten into its weak form and the boundary condition $\vec{\nabla}\bar{\varepsilon}_{eq} \cdot \vec{n} = 0$ is applied, where $\vec{n}$ denotes the normal at the outward boundary of the domain Ω considered [11]. Subsequent spatial discretization of the result using a Galerkin scheme yields:

$$\int_{\Omega} \left(\underline{N}_e^T \underline{N}_e + \underline{B}_e^{\,T} l_c^2 \underline{B}_e \right) d\Omega \, \underset{\sim eq}{\bar{\varepsilon}} = \int_{\Omega} \underline{N}_e^T \varepsilon_{eq} \, d\Omega + \int_{\Omega} \underline{N}_e^T \frac{c_{ths}}{\alpha_{dif}} \underline{N}_T \, d\Omega \left| \underset{\sim}{\dot{T}} \right| \qquad (5.9)$$

where $\underset{\sim eq}{\bar{\varepsilon}}$ denotes a column with the nodal values of the non-local equivalent strain, where the matrices $\underline{N}_T$ and $\underline{N}_e$ contain the interpolation functions for the temperature and the non-local equivalent strain, respectively, and where the matrix $\underline{B}_e$ contains the spatial derivatives of $\underline{N}_e$. A backward-Euler scheme is used for the time integration of Eq. (5.9) and of the damage evolution laws given by Eqs. (5.4) and (5.8). The resulting discretized damage equations are non-linear and solved in a standard manner using a Newton-Raphson method. Quadratic finite elements (with eight nodes for two-dimensional applications and twenty nodes for three-dimensional applications) have been used to perform the thermal and mechanical calculations in Ansys. Only the incremental solution variables calculated at the corner nodes are presently available for post-processing. This necessitates a linear interpolation of the temperature and the non-local equivalent strain in Eq. (5.9).

5.3 Snorkel of a steel degassing installation

The damage evolution in consecutive process cycles of a steel degassing installation is analyzed. The effect of a down time reduction is investigated.

5.3.1 Introduction

During production, the quality of steel is enhanced in the liquid phase by the removal of CO gas using the so-called Rheinstahl-Heraus-Oxygen-Blowing (RHOB) process. A schematic representation of a RHOB installation is shown in the left part of Fig.5.1. After immersion of the snorkels into the liquid steel, the pressure in the upper barrel is reduced to vacuum. Consequently, the bath level rises and CO gas escapes from the liquid steel. The degassing of the entire ladle content is achieved by circulation of the liquid steel through the inlet and outlet snorkel.

Prior to its use, the RHOB installation including the snorkels is preheated with burners to minimize the temperature differences occurring in the refractory lining. Preheating is also applied before every degassing cycle. In spite of these precautions, damage has been observed to occur in the refractory lining of the snorkels as illustrated in the right part of Fig. 5.1. The location of the depicted damage is indicated in the left part of Fig. 5.1 by the dashed lines. Horizontal and vertical cracks can be observed as well as the loss of structural integrity in the lower parts of the refractory lining. The damage may have been caused by thermal shock induced during immersion of the snorkels into the liquid steel or during the extraction from the liquid steel when the hot refractory lining becomes exposed to ambient air. Moreover the temperature increase of the snorkels during their use is accompanied with thermal deformation and a compressive stress in the interior lining. Correspondingly, a tensile stress state exists in the refractory lining on the snorkel outside, which is therefore sensitive to thermal shock damage.

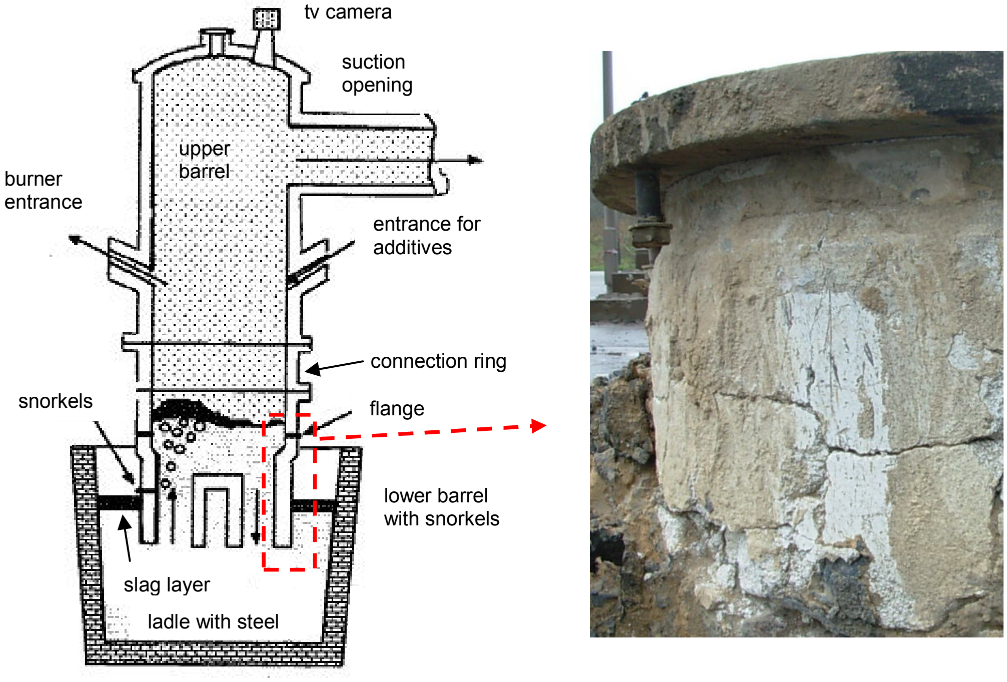
tv camera
suction opening
upper barrel
burner entrance
entrance for additives
connection ring
snorkels
flange
lower barrel with snorkels
slag layer
ladle with steel

Fig. 5.1. Schematic view of an RHOB installation (left), the dashed lines show the location of the model, and picture of the indicated damaged snorkel lining including the lower flange (right)

5.3.2 Geometry, boundary conditions and discretization

The lower part of the snorkel is modelled in an axi-symmetric configuration as presented in Fig. 5.2. At the flange, the snorkel is connected to the main body of the RHOB with screws (left out of consideration). The refractory concrete type 1, commonly used in constructive applications, is reinforced with small anchors and is therefore modelled as rigidly connected to the shell. The anchors are not taken into account. The refractory concrete type 2 is used as a filling material between the wear lining and the shell. The three parallel, horizontal lines depicted in the wear lining indicate expansion joints applied to lower the stresses in the bricks, which have not been modelled individually. The damage evolution in refractory concrete type 1 is investigated numerically. The possible development of damage in the other materials (wear lining, refractory concrete type 2 and steel) is left out of consideration. The two rectangular openings in the flange represent cooling canals.

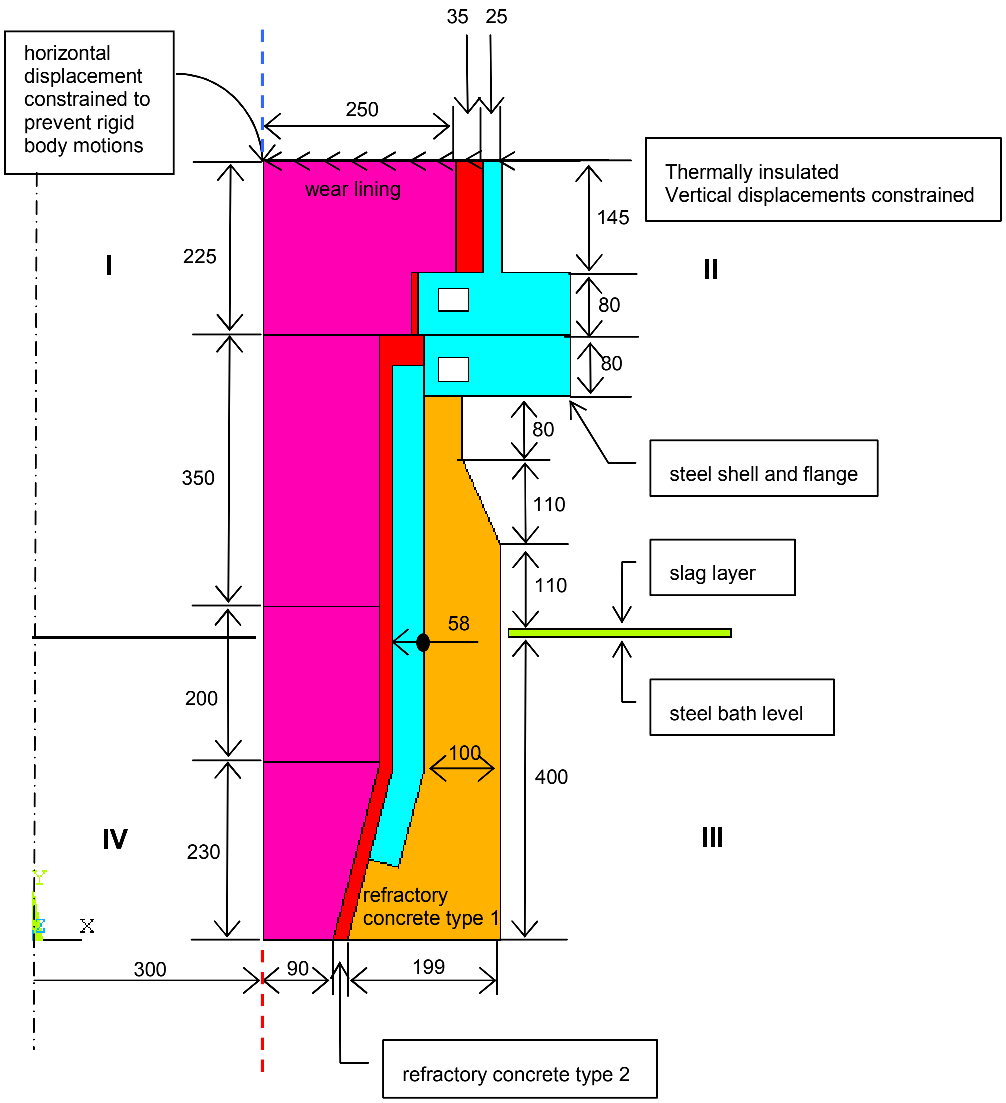
35
25
horizontal displacement constrained to prevent rigid body motions
250
Thermally insulated
Vertical displacements constrained
wear lining
145
I
225
II
80
80
80
steel shell and flange
350
110
110
slag layer
58
200
steel bath level
100
400
IV
III
230
refractory concrete type 1
Y
Z
X
300
90
199
refractory concrete type 2

Fig. 5.2. Snorkel geometry and static boundary conditions (only main dimensions are presented), the transient thermal boundary conditions are prescribed per area (I to IV), areas I and IV are separated by the depicted steel bath level, areas III and IV are separated by the dashed red line, areas II and III are separated by the slag layer, areas I and II are separated by the dashed blue line

The thermo-elastic properties of refractory concrete type 1 are listed in Table 5.1. Young's modulus was determined from three-point bending tests. The estimated values for Poisson's ratio and the thermal capacity are typical for refractory concretes. The coefficient of thermal expansion was determined from dilatation tests. The density and thermal conductivity are obtained from standard measurements. The thermal conductivity and Young's modulus are measured and specified as a function of the temperature T in °C in the temperature regime of interest.

Type	Quantity	Value	Unit	Source
Elastic material parameters	Young's modulus	$E(T)=2.6\cdot 10^{4}+46T-0.1T^{2}-4\cdot 10^{-5}T^{3}$	MPa	Measured
	Poisson's ratio	$v=0.2$	[-]	Estimate
Thermo-elastic material parameter	Thermal expansion	$\alpha_{th}=7.7\cdot 10^{-6}$	°C^{-1}	Measured
Thermal material parameters	Density	$\rho=2860$	kg m^{-3}	
	Conductivity	$\lambda(T)=4.32-4\cdot 10^{-3}T+3\cdot 10^{-6}T^{2}-7\cdot 10^{-10}T^{3}$	W m^{-1} °C^{-1}	
	Capacity	$C_p(T)=1250$	J kg^{-1} °C^{-1}	Estimate

Table 5.1. Thermo-elastic material parameters of refractory concrete type 1

Table 5.2 contains the damage material parameters of refractory concrete type 1. The compressive and tensile strength, defining the ratio η, were determined from uni-axial compressive and three-point bending tests respectively. The elastic damage threshold κ_0 was also obtained from three-point bending tests. The estimated length scale l_c reflects the coarseness of the refractory material [13]. The thermal damage parameters T_0, γ and ϕ have been quantified in [13] describing the numerical-experimental parameter identification for a refractory material of similar heterogeneity as presently considered. Accordingly the values of the other damage parameters A, β, C_{ths} and B have been estimated based on the values identified in [13] and the reported qualitative damage patterns observed for this problem. The properties of the other materials are presented in Section 5.7.

The interface of the considered snorkel geometry with the other part of the RHOB is considered as thermally insulated, as indicated in Fig. 5.2. The governing displacements are constrained in the vertical direction. To prevent rigid body motions the horizontal displacement is supressed in the node located in the upper left corner of the discretized model geometry. The air flow through the cooling canals is represented by forced convection using a heat transfer coefficient of 50 W/m^2°C and an ambient temperature of 20 °C. The mechanisms of heat transfer in areas I to IV depend on the process conditions summarized in Table 5.3, as described in detail in the following paragraph.

Type	Quantity	Value	Unit	Source
Elastic damage parameters	Damage evolution parameters	$A = 80$	[-]	Estimate ~[13]
		$\beta = 3.5$	[-]	
	Damage threshold value	$\kappa_0(T) = 5 \cdot 10^{-4} + 2 \cdot 10^{-6} T - 8 \cdot 10^{-9} T^2 + 6 \cdot 10^{-12} T^3$	[-]	Measured
Thermal damage parameters	Damage evolution parameters	$B = 1.2 \cdot 10^{-4}$	°C^{-1}	Estimate ~[13]
		$\gamma = 0.4$	[-]	Identified in [13]
	Shielding constant	$\phi = 0.075$	[-]	
	Damage threshold value	$T_0 = 21$	°C	
Non-local material parameters	Length scale	$l_c = 10$	mm	
	Thermal shock constant	$C_{ths} = 5 \cdot 10^{-11}$	m^2 °C^{-1}	Estimate ~[13]
Equivalent strain parameter	Compressive/ tensile strength	$\eta(T) = 4.57 - 5.8 \cdot 10^{-3} T + 1 \cdot 10^{-5} T^2 - 3 \cdot 10^{-9} T^3$	[-]	Measured

Table 5.2. Damage material parameters of refractory concrete type 1

Process condition	Description	I	II	III	IV
Preheating	Burner positioned inside snorkel	Forced convection and radiation between burner and wear lining	Natural convection and radiation to ambient surroundings	Natural convection and radiation to ambient surroundings	Forced convection and radiation between burner and wear lining
Immersion	Liquid steel present in areas III and IV	Radiation between steel bath and wear lining. Natural convection.	Radiation between slag layer, refractory concrete type 1 and flange. Natural convection.	Forced convection	Forced convection
Degassing	Liquid steel present in areas I, III and IV	Forced convection	Radiation between slag layer, refractory concrete type 1 and flange. Natural convection.	Forced convection	Forced convection
Degassed	Liquid steel present in areas III and IV	Radiation between steel bath and wear lining. Natural convection.	Radiation between slag layer, refractory concrete type 1 and flange. Natural convection.	Forced convection	Forced convection
Extraction Down time	Entire snorkel lifted out of steel bath	Natural convection and radiation to ambient surroundings	Natural convection and radiation to ambient surroundings	Natural convection and radiation to ambient surroundings	Natural convection and radiation to ambient surroundings

Table 5.3. Process dependent heat transfer conditions per area, as indicated in Fig. 5.2

Preheating is applied before the first use of the RHOB and at the beginning of every degassing cycle. The governing burner action in areas I and IV is considered as forced convection using a heat transfer coefficient of

900 W/m^2°C and an ambient temperature of 900 °C. The radiation between the burner and the wear lining has been accounted for as well using a value of 0.9 for the emissivity coefficient of wear lining material. This value is also used to represent the emissivity of the radiating surfaces of refractory concrete types 1 and 2 and of the steel flange and shell. The thermal transport in areas II and III during the preheating stage is due to radiation and natural convection to the ambient surroundings. The used heat transfer coefficients for natural convection depend on the heat flow directed upwards or downwards from a horizontal surface or from a vertical surface. These heat transfer coefficients are denoted by respectively h_{hor-up}, $h_{hor-down}$ and h_{vert} [14]:

$$h_{hor-up} = 2.38\left(T_{surf} - T_{amb}\right)^{0.3} \tag{5.10}$$

$$h_{hor-down} = 1.21\left(T_{surf} - T_{amb}\right)^{0.3} \tag{5.11}$$

$$h_{vert} = 1.63\left(T_{surf} - T_{amb}\right)^{0.3} \tag{5.12}$$

where T_{surf} and T_{amb} denote the surface and ambient temperature (20 °C), respectively. The heat transfer in areas III and IV during immersion of the snorkels into the liquid steel due to forced convection are characterized by a heat transfer coefficient of 3000 W/m^2°C and an ambient steel temperature of 1540 °C. The governing thermal transport in area I is governed by natural convection from the wear lining to the ambient surroundings combined with radiation between the wear lining and the liquid steel. Similar thermal boundary conditions are imposed in area II during the immersion stage except that the irradiative heat transfer now takes place between the snorkel outside and the modelled layer of liquid slag of 600 °C. In the consecutive degassing stage the snorkel is entirely filled with (flowing) liquid steel. The mechanism of thermal transport in area I is now equal to that in area IV. In the 'degassed' stage following the degassing treatment, the steel level has dropped back to that in the immersion stage with its corresponding heat transfer conditions. Subsequently the snorkels are extracted from the liquid steel. The governing thermal transport in all areas is accounted for by radiation and natural convection to the ambient surroundings. The process cycle is concluded with a period of down time. The heat transfer conditions of the extraction stage apply.

Table 5.4 specifies the applied time discretization of the degassing process based on the realistic operation of the RHOB installation. Small time steps have been applied in the immersion, degassed and extraction stage to deal with large temperature rates. Accordingly the non-cylic preheating stage is subdivided into ‘preheating 1’ and ‘preheating 2’. The cyclic preheating stage applied before every degassing treatment is denoted by ‘preheating 3’.

Process condition	**Time step number**	**Time step size [s]**	**Elapsed time [s]**
Preheating 1	1-10	10	100
Preheating 2	11-34	1200	28800
Preheating 3	N*(25-64)	10	300
Immersion	N*(65-88)	5	120
Degassing	N*(89-108)	60	1200
Degassed	N*(109-114)	5	30
Extraction	N*(115-138)	5	120
Down time	N*(139-153)	60	900

Table 5.4. Time discretization of the RHOB process conditions, the number of the simulated treatment cycle is specified by N

The discretization of the snorkel model is depicted in Fig. 5.3. Elements with 8 nodes have been used. The corresponding quadratic interpolation functions are evaluated at 3 x 3 integration points. Expansion joints are applied at certain locations in the wear lining to lower the stresses. Dedicated contact elements were used to model these joints as well as the contact between the upper and lower flange. The top layer of the steel and slag bath is discretized to account for the irradiative thermal transport using the so-called radiation matrix method [37]. In this method the matrix is established containing the generated view factors between the radiating surfaces. The matrix is introduced as a super element in the thermal analysis.

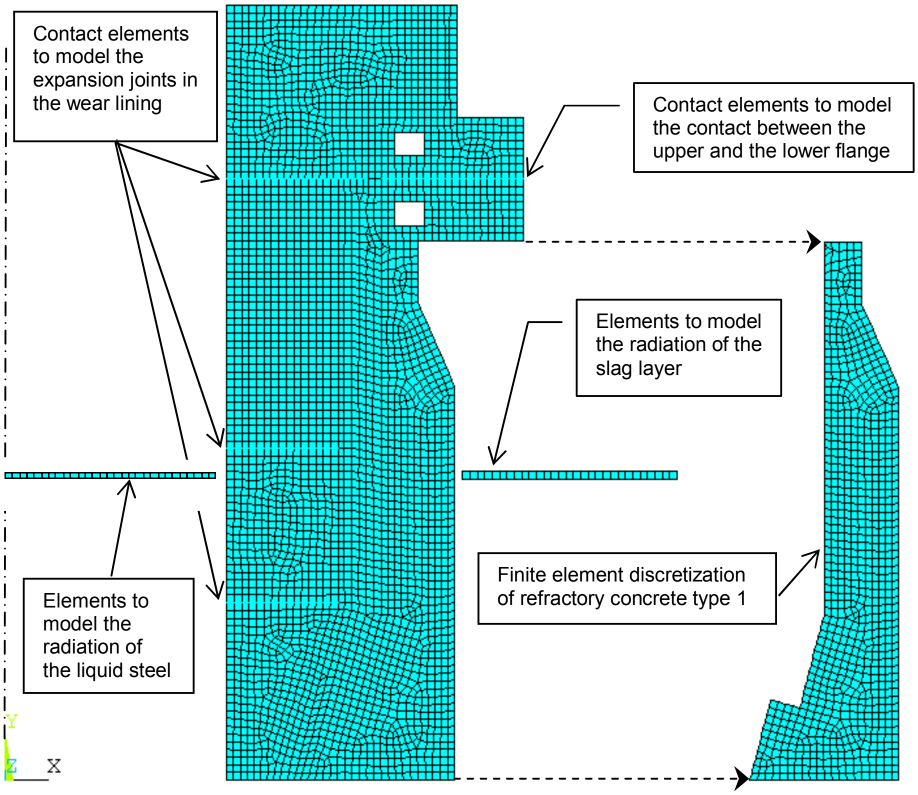
Contact elements to model the expansion joints in the wear lining
Contact elements to model the contact between the upper and the lower flange
Elements to model the radiation of the slag layer
Finite element discretization of refractory concrete type 1
Elements to model the radiation of the liquid steel
Y
Z
X

Fig. 5.3. Finite element discretization of the complete snorkel model (left) and of the refractory concrete type 1 only (right)

5.3.3 Analysis results

The damage evolution in the refractory concrete type 1 during four consecutive degassing cycles is analyzed. This is referred to as the ‘actual’ situation. In an additional numerical investigation the effect of a reduction in down time is demonstrated. The results achieved are discussed at the end of this subsection.

Figs. 5.4 and 5.5 present, respectively, the temperature and damage distribution at various stages of the first degassing cycle. Evidently, the highest temperatures in the refractory concrete, after the preheating are obtained in the vicinity of the snorkel interior. At the beginning of the immersion stage the existing temperature distribution is only affected in the area of contact with the liquid steel. The propagation of the elastic shock wave induced by the nearly instantaneous thermal expansion [13] already resulted in damage evolution over a considerable distance into the refractory concrete lining. Up to the end of the degassed stage, the overall refractory concrete temperature has increased considerably. The temperature in the upper part of the concrete refractory lining remains relatively low due to the internal flange cooling. In addition to the damage present at the contact surface with the liquid steel, a diagonally orientated damage pattern has developed. Based on the results of the second numerical analysis, discussed in the next paragraph, it is concluded that this damage pattern is due to the up quench thermal shock induced in the immersion stage. It appears furthermore that the strain rates induced during extraction do not exceed those induced during the immersion stage. Only in the down-right corner area relatively high temperature gradients can be observed at the beginning of the extraction stage. Consequently the damage has only grown in that corner area. Note that the entire submerged part of the refractory concrete has been subject to thermal deformation, resulting in a corresponding damage pattern.

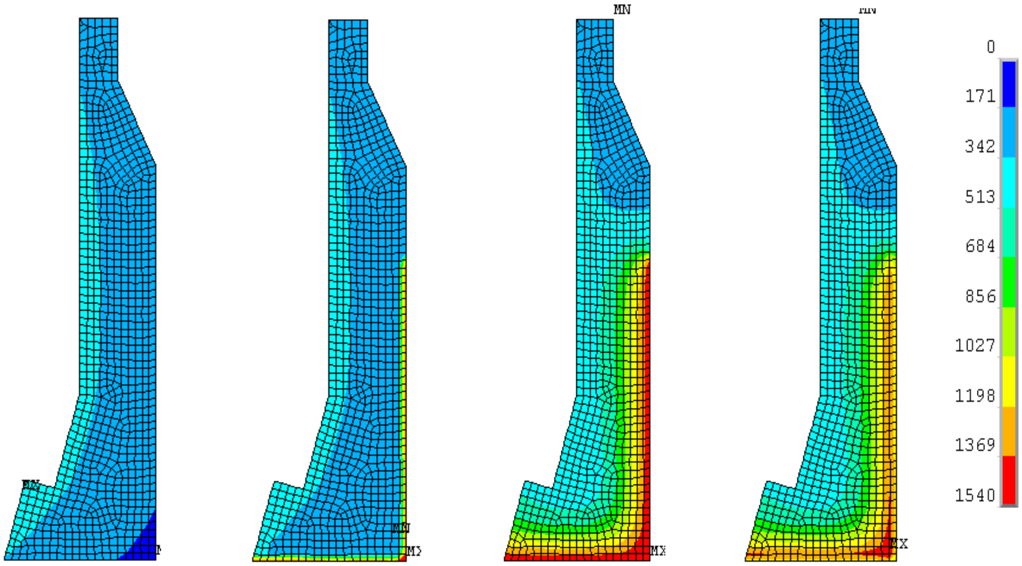

Fig. 5.4. Temperature distribution (°C) in the first processing cycle, from left to right: at the end of the preheating stage (time step 64, Table 5.4), at the beginning of the immersion stage (time step 65), at the end of the degassed stage (time step 114) and at the beginning of the extraction stage (time step 115)

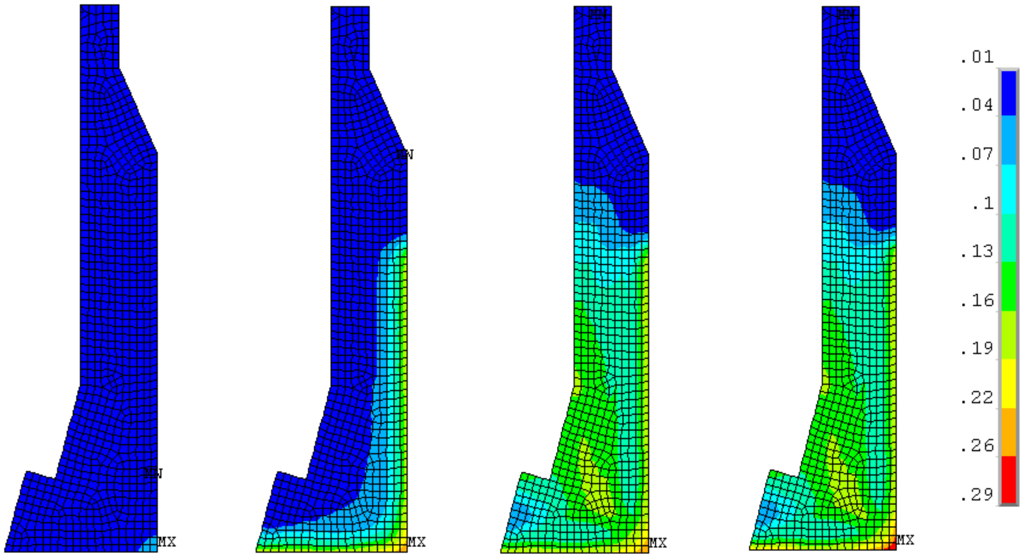

Fig. 5.5. Damage distribution in the first processing cycle, from left to right: at the end of the preheating stage (time step 64, Table 4), at the beginning of the immersion stage (time step 65), at the end of the degassed stage (time step 114) and at the beginning of the extraction stage (time step 115)

Figs. 5.6 and 5.7 visualize the damage distribution after four consecutive processing cycles with down time periods of respectively 15 and 2 min. The damage patterns distinguished in the previous paragraph continue to evolve during the modelled process cycles. The damage evolution in particularly the actual case may ultimately result in macro-cracks propagating diagonally in the direction of the down-right corner area of the refractory concrete lining. It appeared that a reduction of the down time has resulted in a lower damage level, especially after the third and fourth processing cycle due to the lower temperature and consequently strain rates. The previously described damage patterns are all less pronounced. Moreover, the direction of the damage development in the centre of the refractory concrete lining changes from diagonal into downward vertical. The simulation results show that down time reduction can be an effective method to lower the damage in the refractory concrete lining, thereby increasing its lifetime.

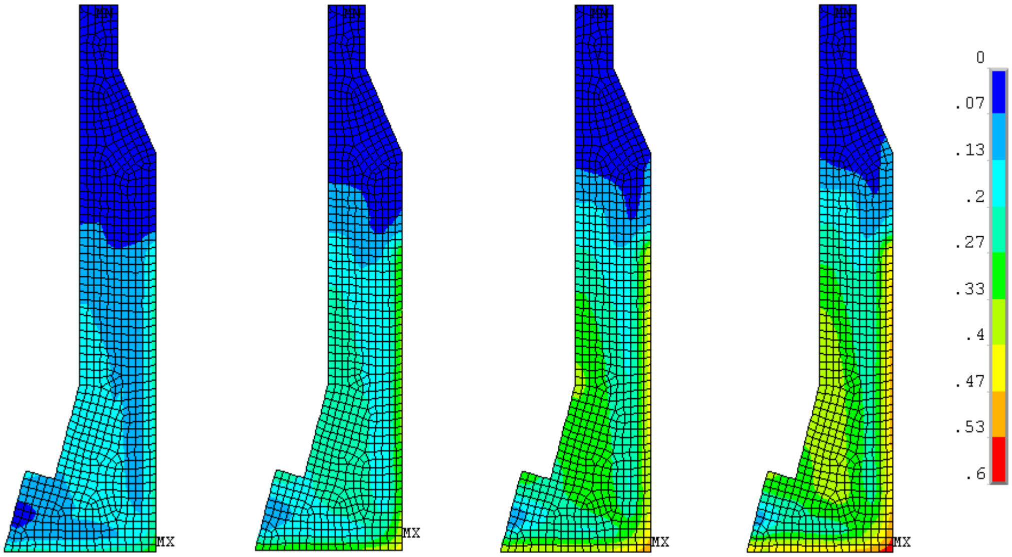
MN
MN
MN
MN
MX
MX
MX
MX
0
.07
.13
.2
.27
.33
.4
.47
.53
.6

Fig. 5.6. Damage distribution at the end of four consecutive treatment cycles (down time period of 15 min.)

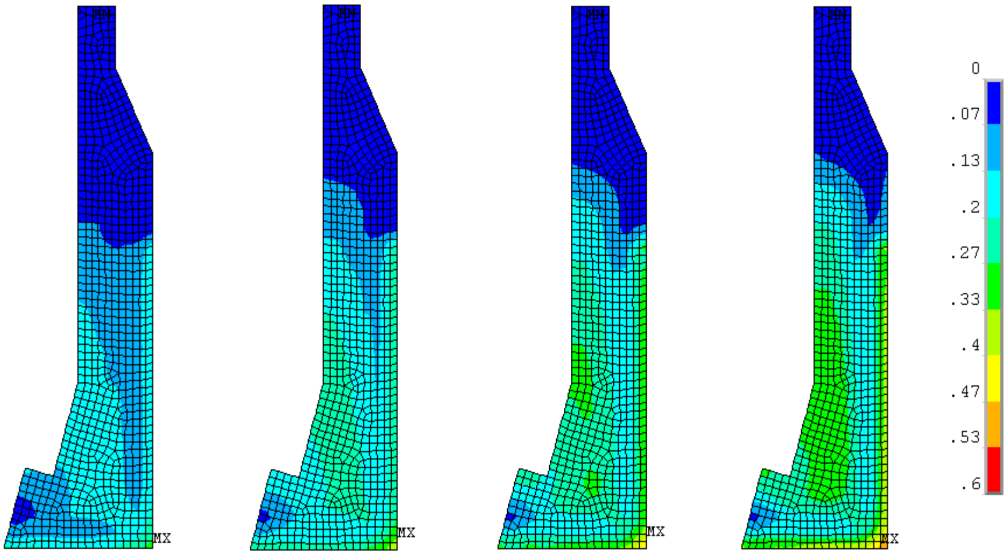
MN
MN
MN
MN
MX
MX
MX
MX
0
.07
.13
.2
.27
.33
.4
.47
.53
.6

Fig. 5.7. Damage distribution at the end of four consecutive treatment cycles (down time period of 2 min.)

5.4 Slag ring of a steel ladle

The thermal shock damage in the refractory lining of a steel ladle is next investigated. To this end, a single brick of the slag ring lining is modelled with appropriate boundary conditions. The mechanical ability of the refractory material to withstand the thermal expansion induced by thermal shock is investigated in a sensitivity analysis.

5.4.1 Introduction

In and between treatments as discussed in section 5.3 liquid steel is contained in a ladle. Large temperature gradients are induced in the refractory lining during the filling and emptying of the ladle. The bricks of a slag ring refractory lining, indicated in a schematic view of a ladle in Fig. 5.8, are alternatingly subject to sudden contact with liquid steel and ambient air. A damaged slag ring lining is shown in Fig. 5.9. The horizontal cracks at half the brick height occurred during the emptying of the ladle. The subsequent exposure of the hot refractory lining to ambient air induces a contraction of the thermally expanded brick material. Consequently, tensile stresses and cracks develop at the hot face of the bricks. The material loss at the vertical corners of the bricks is due to the contact with liquid steel. The resulting temperature increase causes (a sudden) thermal expansion at the brick hot face constrained by neighbouring bricks. A compressive stress state results, at some distance equilibrated by a tensile stress state. A layered-wise spalling of refractory material from the hot face is induced, resulting in the depicted rounded-off brick ends.

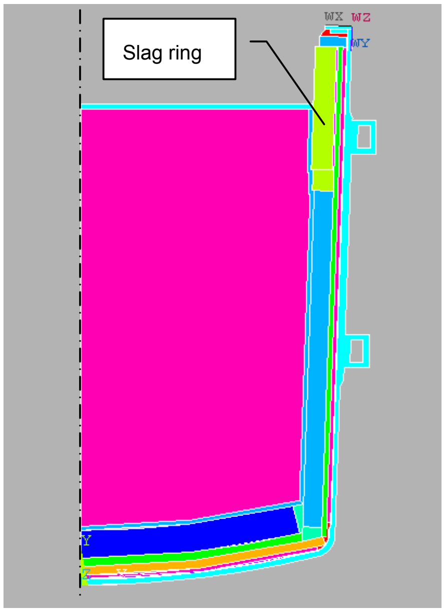

Fig. 5.8. Schematic view of a steel ladle (axi-symmetric cross-section)

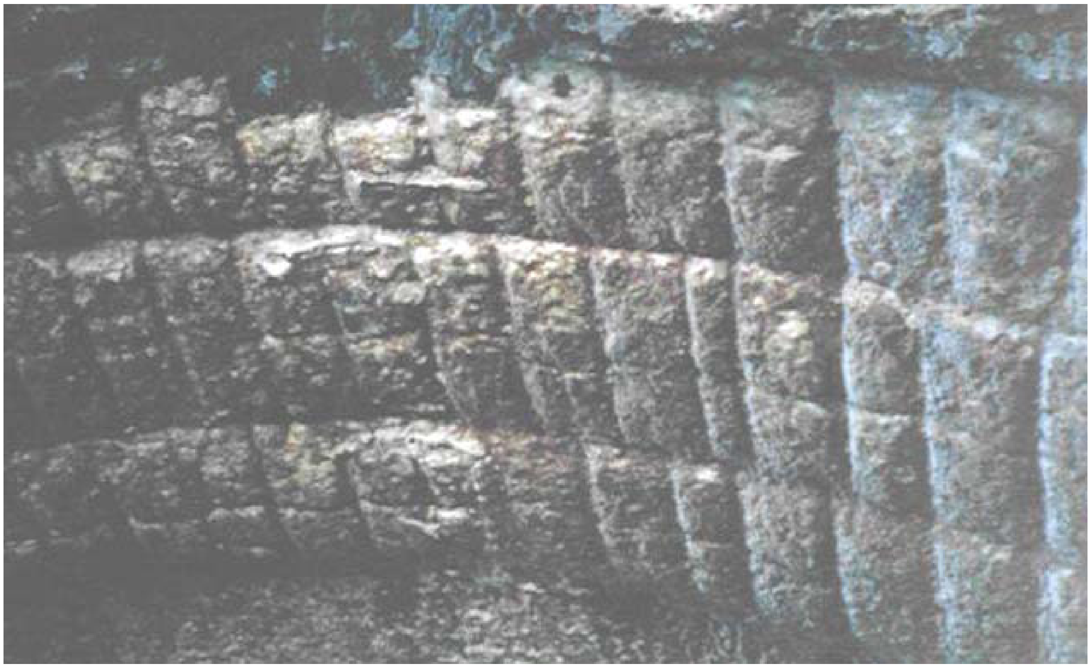

Fig. 5.9. Damaged slag ring with rounded-off brick ends due to (sudden) thermal expansion after filling of the ladle; the horizontal surface cracks at the brick ends are induced by sudden contraction due to the contact with ambient air after emptying of the ladle [35]

5.4.2 Geometry, boundary conditions and discretization

A quarter brick of the slag ring refractory lining is studied. To this purpose, other parts of the lining, including the steel shell are modelled as well. Fig. 5.10 shows the geometry of the model as well as the boundary conditions. The permanent lining is designed to last the entire ladle life as opposed to the wear lining. The insulation lining and the micro-porous layer are installed to keep the temperatures of the liquid steel and the shell at acceptable and safe levels, respectively.

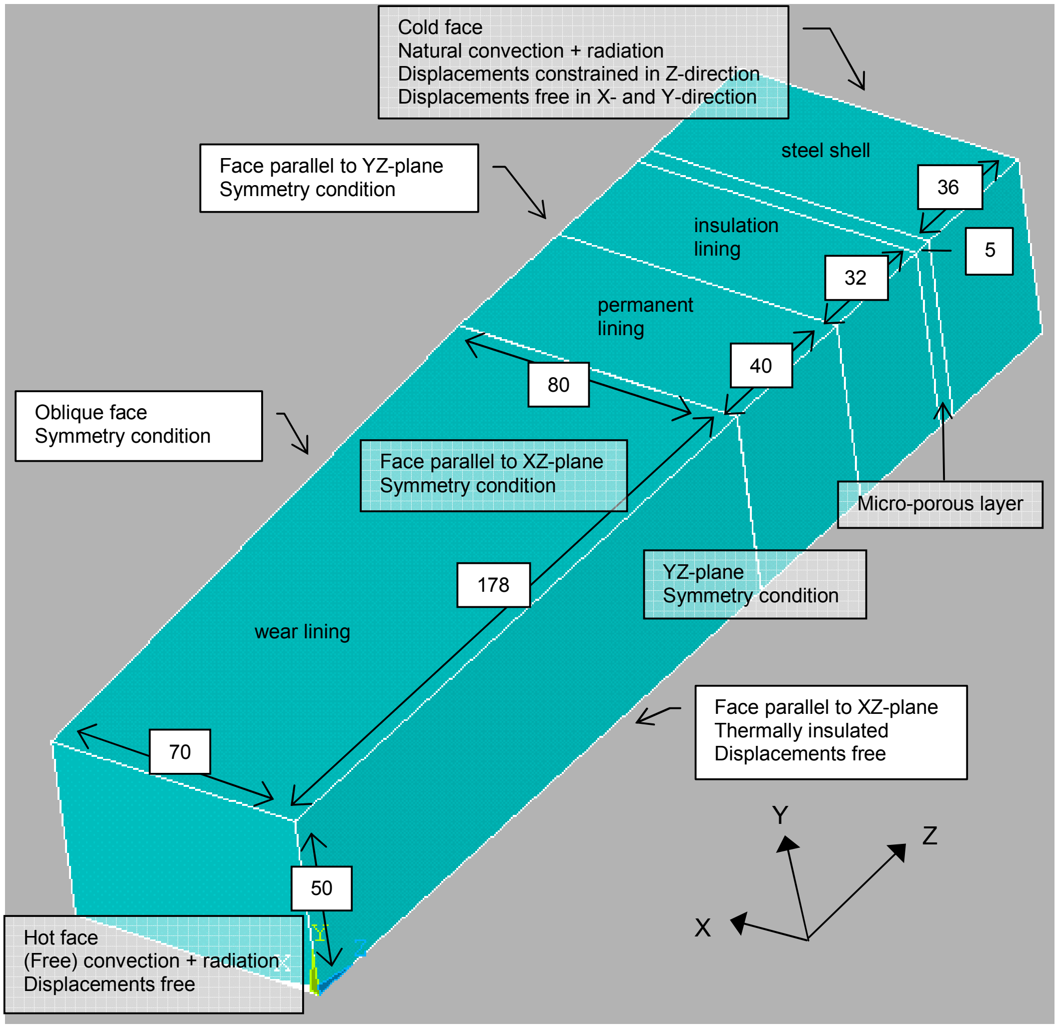
Cold face
Natural convection + radiation
Displacements constrained in Z-direction
Displacements free in X- and Y-direction
Face parallel to YZ-plane
Symmetry condition
steel shell
36
insulation lining
5
32
permanent lining
40
80
Oblique face
Symmetry condition
Face parallel to XZ-plane
Symmetry condition
Micro-porous layer
178
YZ-plane
Symmetry condition
wear lining
Face parallel to XZ-plane
Thermally insulated
Displacements free
70
Y
Z
X
50
Hot face
(Free) convection + radiation
Displacements free

Fig. 5.10. Model of the slag ring lining, specification of the boundary conditions

The thermo-elastic material parameters of the wear lining, specified in Table 5.5, have all been obtained from standard measurements as described in Section 5.3.2. Table 5.6 contains the damage material parameters of the wear lining which have been obtained for a similar procedure as for the refractory concrete type 1 material of the RHOB installation. Note that the damage parameters A, β, c_{ths} and B are again estimated on the basis of the values identified in [13] for a refractory material of similar heterogeneity and the qualitative damage distributions observed in the engineering practice for the problem of interest here. The properties of the other materials are presented in Section 5.8.

Type	Quantity	Value	Unit	Source
Elastic material parameters	Young's modulus	$E(T)=48\cdot 10^3-6.39T-0.011T^2-7\cdot 10^{-6}T^3$	MPa	Measured
	Poisson's ratio	$\nu=0.22$	[-]	Estimate
Thermo-elastic material parameter	Thermal expansion	$\alpha_{th}=3\cdot 10^{-6}+1\cdot 10^{-8}T$	°C^{-1}	Measured
Thermal material parameters	Density	$\rho=3023$	kg m^{-3}	
	Conductivity	$\lambda(T)=9.8-3.3\cdot 10^{-3}\,T-3\cdot 10^{-7}T^2$	W m^{-1} °C^{-1}	
	Capacity	$C_p(T)=748+0.18\,T+4\cdot 10^{-4}T^2$	J kg^{-1} °C^{-1}	

Table 5.5. Thermo-elastic material parameters of the wear lining

Type	Quantity	Value	Unit	Source
Elastic damage parameters	Damage evolution parameters	$A=90$	[-]	Estimate ~[13]
		$\beta=2.8$	[-]	
	Damage threshold value	$\kappa_0(T)=0.0008-8\cdot 10^{-8}\,T+10^{-10}\,T^2$	[-]	Measured
Thermal damage parameters	Damage evolution parameters	$B=1\cdot 10^{-4}$	°C^{-1}	Estimate ~[13]
		$\gamma=0.4$	[-]	Identified in [13]
	Shielding constant	$\phi=0.075$	[-]	
	Damage threshold value	$T_0=21$	°C	
Non-local material parameters	Length scale	$l_c=11$	mm	
	Thermal shock constant	$C_{ths}=1\cdot 10^{-11}$	m^2 °C^{-1}	Estimate ~[13]
Equivalent strain parameter	Compressive/ tensile strength	$\eta(T)=10.26-9.9\cdot 10^{-3}\,T+\ldots$ $\ldots+2\cdot 10^{-5}T^2-2\cdot 10^{-8}T^3+9\cdot 10^{-12}T^4$	[-]	Measured

Table 5.6. Damage material parameters of the wear lining

As indicated in Fig. 5.10, symmetry conditions are prescribed on the model faces parallel to and coinciding with respectively the XZ- and YZ-plane. Symmetry conditions are also applied on the oblique side of the wear lining section to represent the neighbouring brick and on the side of the slag ring lining parallel to the YZ plane to represent the ladle lining in circumferential direction. The model side coinciding with the XZ-plane is represented as adiabatic whereas the displacements are unconstrained to account for the free expansion of the slag ring lining in the positive Y-direction, see Fig. 5.8. At the hot and cold face of the lining the displacements are respectively unconstrained and constrained in the Z-direction. The thermal transport at the cold face is governed by radiation and natural convection. The irradiative heat transfer is simulated as convection characterized by the heat transfer coefficient α_{rad} defined as:

$$\alpha_{rad} = C_e \, k \, \frac{T_{cf}^{4} - T_{amb}^{4}}{T_{cf} - T_{amb}} \tag{5.13}$$

where T_{cf} represents the cold face temperature and T_{amb} is the ambient temperature (20 °C). The coefficient of emissivity and Boltzmann's constant are denoted by C_e and k respectively. The thermal boundary conditions imposed on the brick hot face depend on the loading condition of the ladle and are described in the next paragraph.

The ladle is first preheated by a burner, represented by convection with a heat transfer coefficient of 1000 W/m^2°C and an ambient flame temperature of 1100 °C. Consecutively liquid steel is poured into the ladle. The governing thermal transport is simulated by convection with a heat transfer coefficient of 3000 W/m^2°C and an ambient steel temperature of 1540 °C. After a hold time representing processing of the liquid steel as described in Section 5.3, the ladle is emptied. The cooling mechanism comprises natural convection and radiation using Eqs. (5.12) and (5.13) respectively. The ambient temperature of the air around the cooling ladle is set to 100 °C. Thereafter, in the down time period the ladle remains empty.

The applied time discretization during loading, specified in Table 5.7, is based on actual process data. Small time steps are used in the filling and emptying stage to deal with the large temperature rates. Accordingly, the preheating phase is split into 'preheating 1' and 'preheating 2'. The numerical analysis is performed for four consecutive cycles of filling, processing, emptying and down time.

Loading condition	**Time step number**	**Time step size [s]**	**Elapsed time [s]**
Preheating 1	1-10	10	100
Preheating 2	11-30	1200	24000
Filling	M*(31-54)	5	120
Processing	M*(55-72)	60	1080
Emptying	M*(73-96)	5	120
Down time	M*(97-108)	60	720

Table 5.7. Time discretization of the ladle loading conditions, the number of loading cycles is specified by M.

The finite element discretization of the slag ring model is shown in Fig. 5.11. Brick elements with 20 nodes are used. The nodal displacements and temperatures are interpolated using the corresponding quadratic interpolation functions evaluated at 14 integration points. The thermal contact between the wear lining and the permanent lining is modelled with nodal constraints enforcing equal temperatures at the contact surfaces. The corresponding mechanical, sliding contact is described with contact elements using a (Coulomb) friction coefficient of 0.15. The contact surfaces of the wear and permanent lining are modelled as deformable and rigid respectively.

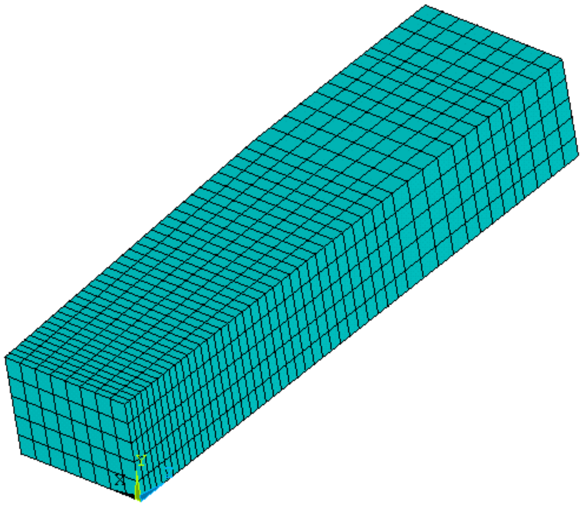

Fig. 5.11. Finite element discretization of slag ring model

5.4.3 Analysis results

Figs. 5.12 and 5.13 depict the temperature distribution at consecutive stages during the first loading cycle of the ladle. The corresponding damage distribution is shown in Figs. 5.14 and 5.15. It can be observed that at the end of the preheating stage the minimum temperature of the brick exceeds 850 °C. This implies that thermal and elasticity-based damage will already be present. Moreover, the constrained thermal expansion induced during the preheating phase has resulted in a concentration of the damage at some distance from the hot face. At the beginning of the filling stage, the temperature distribution is only affected in the contact zone with the liquid steel. The damage induced by the corresponding (instantaneous) thermal expansion increases over a considerable distance from the shock front. At the hot face the damage growth is inhibited by the compressive stress state. Note that this might not be the case for higher values of the thermal shock constant c_{ths} that controls the contribution of fine scale damage; see also Eq. (5.5). Until the end of the processing stage, the brick temperature increases continuously. The resulting thermal expansion causes a further increase of the damage. Finally it can be observed that the down quench thermal shock induced during the emptying of the ladle only causes a damage increase at the brick hot face.

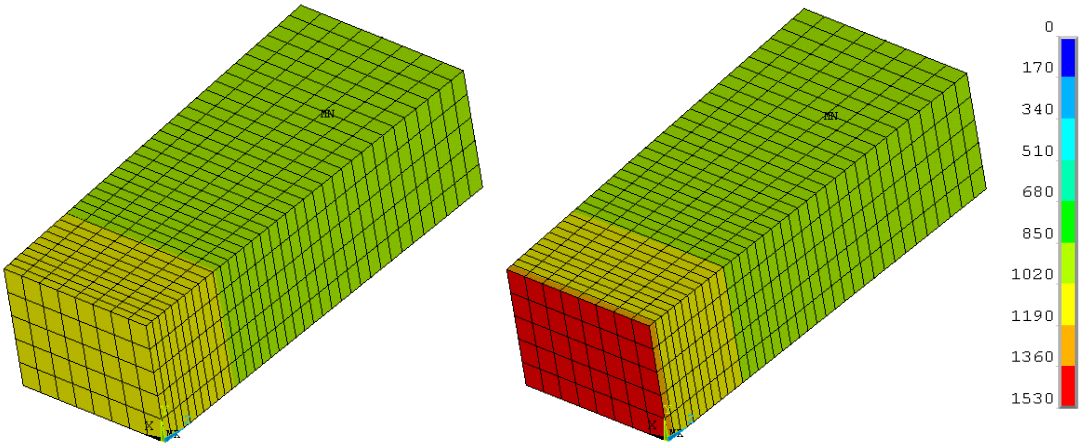

Fig. 5.12. Temperature distribution (°C) in the first loading cycle, at the end of the preheating stage (left, time step 30, Table 5.7) and at the beginning of the filling stage (right, time step 31)

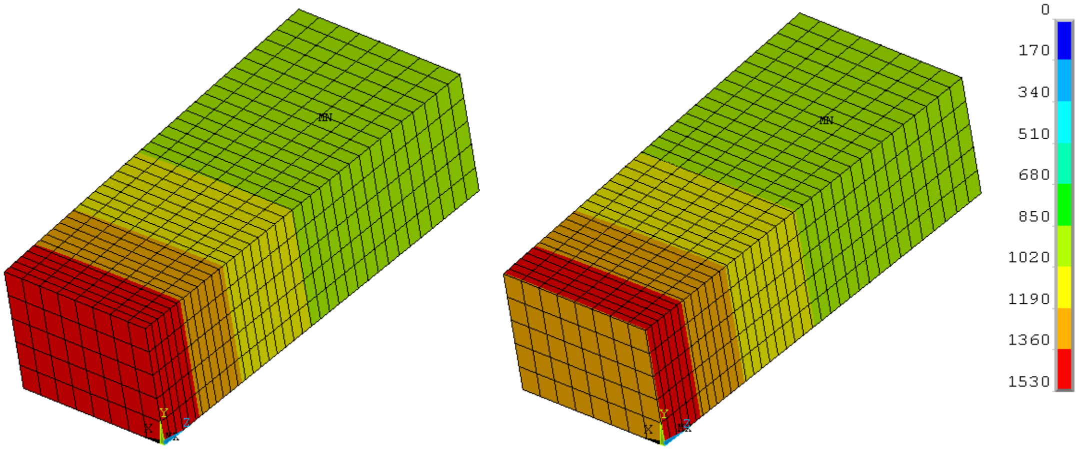
MN
MN
0
170
340
510
680
850
1020
1190
1360
1530

Fig. 5.13. Temperature distribution (°C) in the first loading cycle, at the end of the processing stage (left, time step 72) and at the beginning of the emptying stage (right, time step 73)

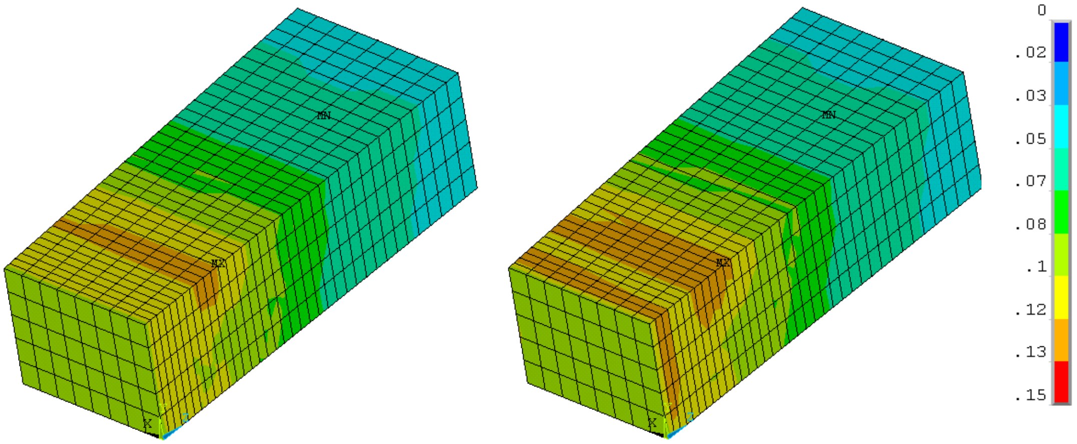
MN
MX
MN
MX
0
.02
.03
.05
.07
.08
.1
.12
.13
.15

Fig. 5.14. Damage distribution in the first loading cycle, at the end of the preheating stage (left, time step 30, Table 7) and at the beginning of the filling stage (right, time step 31)

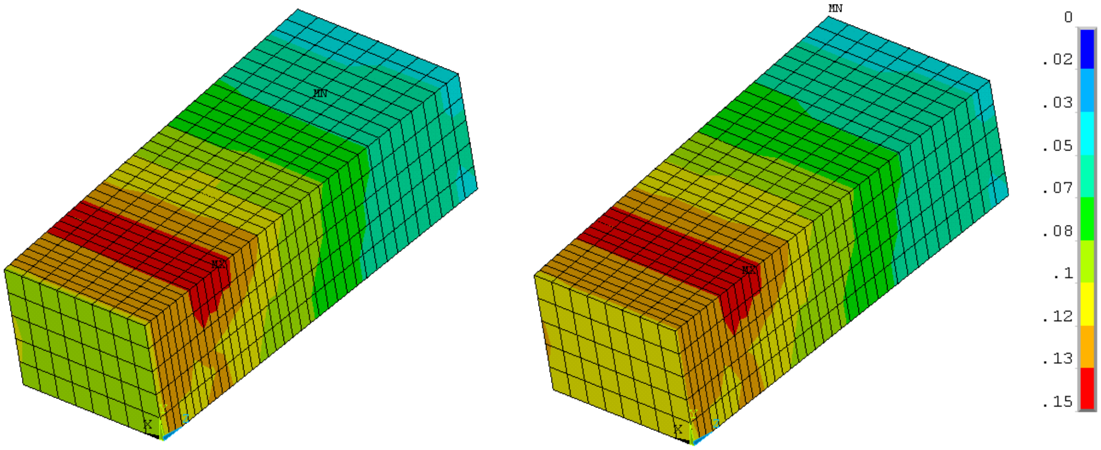

Fig. 5.15. Damage distribution in the first loading cycle, at the end of the processing stage (left, time step 72) and at the beginning of the emptying stage (right, time step 73)

The damage distribution after loading cycles 1 and 2 is presented in Fig. 5.16. The damage distribution after loading cycles 3 and 4 is presented in Fig. 5.17. Distinct patterns of damage can be observed for the consecutive loading cycles. The damage at the hot face due to the ladle emptying may result in surface cracks as depicted in Fig. 5.9. The development of damage behind the hot face and at some distance thereof (due to long range elastic deformation) and the resulting constrained thermal expansion may ultimately result in spalling as shown in Fig. 5.9. In order to reduce the stresses and damage in the hot face area of the brick, expansion joints filled with mortar are sometimes used. Another way to limit the damage is to select a brick material with more favorable thermo-elastic properties. This is investigated in the last part of this subsection.

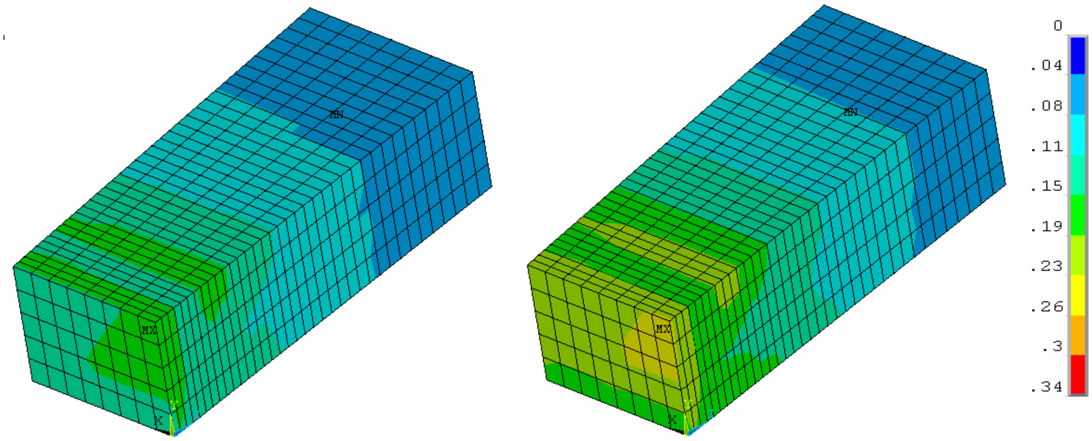

Fig. 5.16. Damage distribution after loading cycles 1 (left) and 2 (right)

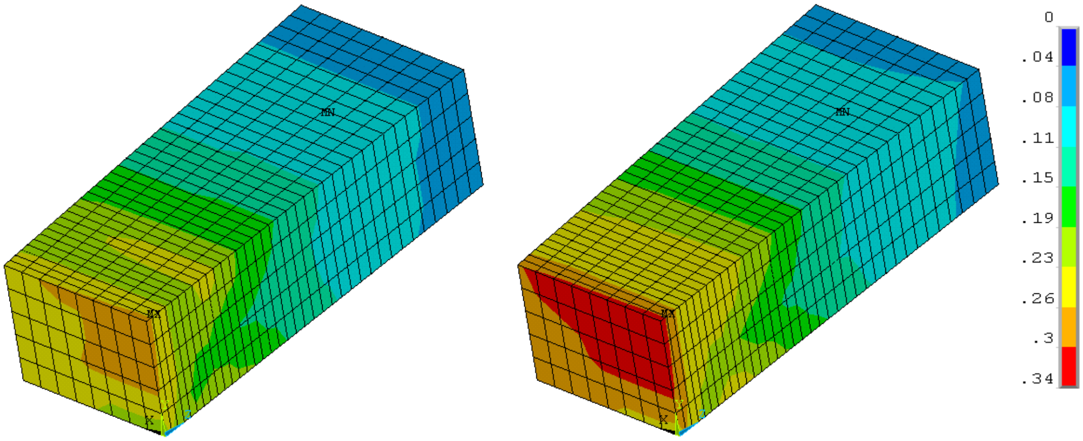

Fig. 5.17. Damage distribution after loading cycles 3 (left) and 4 (right)

The resistance of a refractory material against the initiation of thermal shock fracture is often represented by the Hasselman parameter R defined as [1]:

$$R = \frac{\sigma(1-\nu)}{\alpha_{th} E} \tag{5.14}$$

with σ the tensile strength. The parameter R defines the maximum allowable temperature difference in refractory material subject to infinitely fast heating-up. It is commonly used for the comparative ranking of materials. As the value of Poisson’s ratio is of the same order for certain classes of coarse grain refractory materials, an alternative thermal shock resistance parameter may be defined according to:

$$S = \frac{\kappa_0}{\alpha_{th}} \tag{5.15}$$

with κ_0 the threshold for elasticity-based damage. The parameter S represents the mechanical ability of a refractory material to withstand thermal expansion induced by up quench thermal shock without damage.

This point of departure is further investigated in three cases where both the elastic damage threshold and the thermal expansion coefficient are decreased or increased with 50 %. The damage evolution is again determined during four loading cycles. Fig. 5.18 presents the damage distribution after the fourth loading cycle. It can be observed that the active damage mechanisms are the same, but the overall level of damage increases with higher values of both the thermal expansion coefficient and the elasticity-based damage threshold. It appears that the increase of the elastic strain (resulting from the higher thermal strain, induced by the higher thermal expansion coefficient) is more pronounced than the increase of the elasticity-based damage threshold. Consequently these results indicate that the Hasselman parameter R (in reduced form the parameter S) may not be a suitable indicator for the resistance against thermal shock.

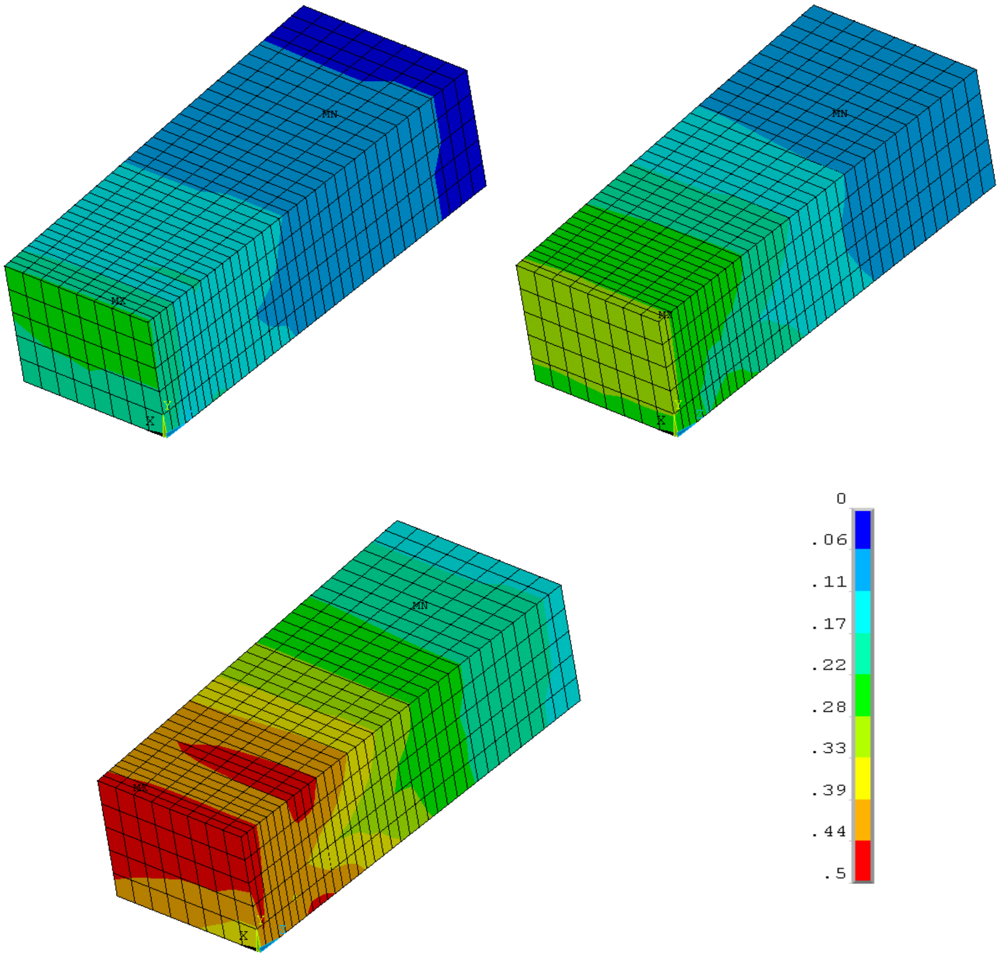

Fig. 5.18. Damage after four loading cycles with 50 % decreased (top, left), unchanged values (top, right) and 50 % increased values (bottom) of both the thermal expansion coefficient and elasticity-based damage threshold.

5.5 Conclusions

In this paper, a recently developed model is used to determine transient thermo-mechanical damage for thermal shock conditions in coarse grain refractory linings of steelmaking installations. To this end, a temperature-dependent non-local damage framework is coupled incrementally with a thermo-mechanical FE package using an operator-split strategy. The constitutive model used, incorporates both non-local elasticity-based damage (due to constrained thermal expansion and fine scale thermal transients) as well as thermal damage (induced by uniform thermal expansion). The modelling of transient thermo-mechanical degradation in high temperature installations using a non-local damage framework has not been reported before in the literature.

To assess the predictive capability of the computational framework, the thermal shock damage in a snorkel of a steel degassing installation was simulated for different cyclic process conditions. Distinct zones of damage development could be observed in the refractory concrete located on the outside of the snorkel, predominantly induced by the (sudden) contact with the liquid steel. It was furthermore shown that a reduction in the cyclic down time of the degassing installation reduces the damage and consequently increases the lifetime of the refractory concrete lining.

In a second industrial example, the thermal shock damage in the slag ring of a steel ladle was numerically investigated as a function of the cyclic loading conditions. To this end a single wear lining brick was modelled using appropriate mechanical and thermal boundary conditions. The consecutive stages of filling, processing, emptying and down time resulted in distinctive zones of damage development, which are consistent with the zones of material failure observed in practice. In a sensitivity analysis it appeared furthermore that the elastic strain induced by a higher thermal expansion coefficient exceeded the elasticity-based damage threshold, increased simultaneously with the same percentage, resulting in a higher level of the damage.

5.6 References

[1] D.P.H. Hasselman, *Thermal stress resistance parameters for brittle refractory ceramics: a compendium,* Ceramic Bulletin, 1970, Vol. 49, pp. 1033-1037

[2] D.P.H. Hasselman, *Figures-of-merit for the thermal stress resistance of high-temperature brittle materials : a review,* Ceramurgia International, 1978, Vol. 4, pp. 147-150

[3] D.P.H. Hasselman, *Unified theory of thermal shock fracture initiation and crack propagation in brittle ceramics,* J. Am. Cer. Soc., 1969, Vol. 52, pp. 600-604

[4] T.J. Lu and N.A. Fleck, *The thermal shock resistance of solids,* Acta Metall. Mater. 1998, Vol. 46, pp. 4744-4768

[5] H.A. Bahr, H. Balke, M. Kuna, H. Lieske, *Fracture analysis of a single edged cracked strip under thermal shock,* Theoretical and applied fracture mechanics, 1987, Vol. 8, pp. 33-39

[6] H.A. Bahr, T. Fett, I. Hahn, D. Munz, I. Pflugbeil, *Fracture mechanics treatment of thermal shock and the effect of bridging stresses,* Thermal shock and thermal fatigue behaviour of advanced ceramics, Kluwer Academic Publishers, pp. 105-117, 1993

[7] N. Schmitt, A. Burr, Y. Berthaud, J. Poirier, *Micro mechanics applied to the thermal shock behavior of refractory ceramics,* Mechanics of Materials, 2002, Vol. 34, pp. 725-747

[8] A. Gasser, K. Terny-Rebeyrotte, P. Boisse, J. Poirier, *A multi-scale approach for refractory structure modelling,* Proceedings of the Unified International Technical Conference on Refractories, Nov. 8-11 2005, The Am. Cer. Soc., pp. 998-1002, Ed. J.D. Smith, 2005

[9] I. Özdemir, W.A.M., Brekelmans, M.G.D. Geers, *Computational homogenization for heat conduction in heterogenous solids,* Int. J. Num. Meth. Eng., 2008, Vol. 73(2), pp. 185-204

[10] I. Özdemir, W.A.M., Brekelmans, M.G.D. Geers, *FE^2 computational homogenization for the thermo-mechanical analysis of heterogeneous solids,* Comp. Meth. Appl. Mech. Eng., 2008, Vol. 198(3-4), pp. 602-613

[11] F. Damhof, W.A.M. Brekelmans, M.G.D. Geers, *Non-local modelling of thermal shock damage in refractory materials,* Engng. Fract. Mech., 2008, Vol. 75, pp. 4706-4720

[12] F. Damhof, W.A.M. Brekelmans, M.G.D. Geers, *Experimental analysis of the evolution of thermal shock damage using transit time measurement of ultrasonic waves*, J. Eur. Cer. Soc., 2009, Vol. 20, pp. 1159-1167

[13] F. Damhof, W.A.M. Brekelmans, M.G.D. Geers, *Non-local modelling of cyclic thermal shock damage including parameter estimation*, to be submitted

[14]. D. Rubesa, *Thermal stress fracture and spalling of well blocks in steel ladles – modelling and numerical simulation,* Veitsch-Radex Rundschau, 1999, Vol. 2, pp. 3-24

[15] J. Knauder, R. Rathner, *Thermo-mechanical analysis of basic refractories*, Radex-Rundschau, 1990, Heft 4

[16] J. Knauder, R. Rathner, *Improved design of a BOF-lining based on thermo-mechanical analysis,* Radex-Rundschau, 1990, Heft 1

[17] S. Yilmaz, *Thermo-mechanical modelling for refractory lining of a steel ladle lifted by crane,* Steel Research, 2003, Vol. 74(8), pp. 485-490

[18] R. Rathner, *Lining design and behavior of BOF's,* Radex-Rundschau, 1990, Heft 4

[19] M. Huger, J.C. Glandus, C. Gault, *Thermo-mechanical modelling of aluminium-graphite ladle shrouds used in continuous casting,* Proceedings of the Unified International Technical Conference on Refractories, Sep. 6-9, The Am. Cer. Soc., pp. 128-132, 1999
[20] N. Schmitt, F. Hild, E. Blond, *Thermal stresses in the working lining of a ladle during the steel refining process,* Advances in refractories for the metallurgical industries IV, 2004, pp. 39-51, Eds. M. Rigaud, C. Allaire
[21] H. Kamio, M. Sugawara, K. Asano, S. Hagihara, *Nonlinear finite element analysis of nozzles for continuous casting,* Refractories (Tokyo), 2004, Vol. 56(3), pp. 133
[22] O. Buyukozturk, T.M. Tseng, *Thermomechanical behaviour of refractory concrete linings,* J. Am. Cer. Soc., 1982, Vol. 65(6), pp. 301-307
[23] J.P. Schneider, B. Coste, *Thermo-mechanical modelling of thermal shock in anodes,* Conf. Proceedings, Light Metals 1993, The Minerals, Metals & Materials Society, 1993
[24] D. Gruber, T. Auer, *FEM based thermo-mechanical investigations of RH-snorkels,* Proceedings of the Unified International Technical Conference on Refractories, Nov. 8-11 2005, The Am. Cer. Soc., Ed. J.D. Smith, 2005
[25] K. Andreev, H. Harmuth, D. Gruber, H. Presslinger, *Thermo-mechanical behaviour of the refractory lining of a BOF converter – a numerical study,* Proceedings of the Unified International Technical Conference on Refractories, 19-22 Oct 2003, Osaka, Japan
[26] A. Gasser, P. Boisse, J. Rousseau, Y. Dutheillet, *Thermo mechanical behaviour analysis and simulation of steel/refractory composite linings,* Composites Science and Technology, 2001, Vol. 61, pp. 2095-2100
[27] P. Boisse, A. Gasser, J. Poirier, J. Rousseau, *Simulations of thermomechanical behaviour of composite refractory linings,* Composites, 2001, Part B 32, pp. 461-474
[28] X. Liang, W.L. Headrick, L.R. Dharani, S. Zhao, J. Wei, *Failure analysis of refractory cup under thermal loading and chemical attack using continuum damage mechanics,* Proceedings of the Unified International Technical Conference on Refractories, Nov. 8-11 2005, The Am. Cer. Soc., pp. 980-984, Ed. J.D. Smith, 2005
[29] B.M. Luccioni, M.I. Figueroa, R.F. Danesi, *Thermo-mechanic model for concrete exposed to elevated temperatures*, Engineering Structures, 2003, Vol. 25, pp. 729-742
[30]. F. Nazaret, O. Barrau, *Damage modelling in a fiber reinforced refractory castable,* Proceedings of the Unified International Technical Conference on Refractories, 13-16 Oct 2009, Salvador, Brazil

[31] X. Liang, W.L. Headrick, L. R. Dharani, S. Zhao, *Modelling of failure in a high temperature black liquor gasifier refractory lining,* Engng. Failure Analysis, 2007, Vol. 14, pp. 1233-1244

[32] K. Willam, I. Rhee, Y. Xi, *Thermal degradation of heterogeneous concrete materials*, J. Mat. Civil Engng., 2005, Vol. 17(3), pp. 276-285

[33] R.H.J. Peerlings, R. De Borst, W.A.M. Brekelmans, J.H.P. de Vree, *Gradient enhanced damage for quasi-brittle materials*, Int. J. Numer. Methods Engng., 1996, Vol. 39, pp. 3391–3403

[34] R.H. Perry, D.W. Green, J.O. Maloney, *Perry's chemical engineers' handbook,* 6th ed., Mc-Graw-Hill Book Company, New York, 1984

[35] K. Andreev, H. Harmuth, *"Numerische Simulation des mechanischen und thermo- mechanischen Verhaltens der Feuerfestzustellungen von Stahlpfannen"*, In: Proc. of Gesteinshüttenkolloquium 2001, Leoben, Österreich, pp. 91-99, 2001

[36] K.S. Al-Jabri, I.W. Burgess, R.J. Plank, *Prediction of the degradation of connection characteristics at elevated temperature,* J. Constr. Steel Res., 2004, Vol. 60(3-5), pp. 771-781

[37] *Ansys Theory manual*, 2009

5.7 Material properties of RHOB snorkel

Type	Quantity	Value	Unit	Source
Elastic material parameters	Young's modulus	$E(T)=9800-2.13T-2.2\cdot 10^{-3}\,T^{2}$	MPa	Measured
	Poisson's ratio	$v=0.22$	[-]	Estimate
Thermo-elastic material parameter	Thermal expansion	$\alpha_{th}=10.2\cdot 10^{-6}$	°C^{-1}	Measured
Thermal material parameters	Density	$\rho=3878$	kg m^{-3}	
	Conductivity	$\lambda(T)=8.88-3.1\cdot 10^{-3}\,T-4\cdot 10^{-7}\,T^{2}$	W m^{-1} °C^{-1}	
	Capacity	$C_p(T)=991+0.33T-8\cdot 10^{-5}\,T^{2}$	J kg^{-1} °C^{-1}	

Table 5.8. Wear lining

Type	Quantity	Value	Unit	Source
Elastic material parameters	Young's modulus	$E(T) = 1870 + 0.70\,T - 2 \cdot 10^{-3}\,T^2 + 5 \cdot 10^{-7}\,T^3$	MPa	Measured
	Poisson's ratio	$v = 0.2$	[-]	Estimate
Thermo-elastic material parameter	Thermal expansion	$\alpha_{th} = 8 \cdot 10^{-6}$	°C^{-1}	Measured
Thermal material parameters	Density	$\rho = 2695$	kg m^{-3}	
	Conductivity	$\lambda = 1.4$	W m^{-1} °C^{-1}	Estimate
	Capacity	$C_p = 1250$	J kg^{-1} °C^{-1}	

Table 5.9. Refractory concrete type 2

Type	Quantity	Value	Unit	Source
Elastic material parameters	Young's modulus	$E(T) = 20 \cdot 10^4 + 145T - 0.99T^2 + 6 \cdot 10^{-4}T^3$	MPa	[36]
	Poisson's ratio	$v = 0.3$	[-]	Estimate
Thermo-elastic material parameter	Thermal expansion	$\alpha_{th} = 11.5 \cdot 10^{-6}$	°C^{-1}	[34]
Thermal material parameters	Density	$\rho = 7850$	kg m^{-3}	Estimate
	Conductivity	$\lambda(T) = 47.2 - 0.04\,T + 1 \cdot 10^{-5}\,T^2 - 2 \cdot 10^{-9}\,T^3$	W m^{-1} °C^{-1}	Measured
	Capacity	$C_p = 447$	J kg^{-1} °C^{-1}	[34]

Table 5.10. Solid steel

5.8 Material properties of slag ring lining

Type	Quantity	Value	Unit	Source
Elastic material parameters	Young's modulus	$E(T)=39\cdot10^{3}+28.7T-0.19T^{2}+\ldots$ $\ldots+2\cdot10^{-4}T^{3}-5\cdot10^{-8}T^{4}$	MPa	Measured
	Poisson's ratio	$\nu=0.2$	[-]	Estimate
Thermo-elastic material parameter	Thermal expansion	$\alpha_{th}=7.6\cdot10^{-6}$	°C^{-1}	Measured
Thermal material parameters	Density	$\rho=2690$	kg m^{-3}	
	Conductivity	$\lambda(T)=1.55+1\cdot10^{-3}\,T-4\cdot10^{-7}\,T^{2}$	W m^{-1} °C^{-1}	
	Capacity	$C_p(T)=503+0.89T-5\cdot10^{-4}T^{2}+1\cdot10^{-7}T^{3}$	J kg^{-1} °C^{-1}	

Table 5.11. Permanent lining

Type	Quantity	Value	Unit	Source
Elastic material parameters	Young's modulus	$E=1000$	MPa	Estimate
	Poisson's ratio	$\nu=0.2$	[-]	Estimate
Thermo-elastic material parameter	Thermal expansion	$\alpha_{th}=6.12\cdot10^{-6}$	°C^{-1}	Measured
Thermal material parameters	Density	$\rho=1157$	kg m^{-3}	
	Conductivity	$\lambda(T)=1.14+7\cdot10^{-4}\,T-3\cdot10^{-7}T^{2}$	W m^{-1} °C^{-1}	
	Capacity	$C_p(T)=652+0.72T-2\cdot10^{-4}T^{2}$	J kg^{-1} °C^{-1}	

Table 5.12. Insulation lining

Type	Quantity	Value	Unit	Source
Elastic material parameters	Young's modulus	$E=1000$	MPa	Estimate
	Poisson's ratio	$\nu=0.2$	[-]	Estimate
Thermo-elastic material parameter	Thermal expansion	$\alpha_{th}=0.5\cdot10^{-6}$	°C^{-1}	Measured
Thermal material parameters	Density	$\rho=250$	kg m^{-3}	
	Conductivity	$\lambda(T)=0.04+2\cdot10^{-5}\,T-3\cdot10^{-8}T^{2}+4\cdot10^{-11}T^{3}$	W m^{-1} °C^{-1}	
	Capacity	$C_p(T)=801+0.17T+6\cdot10^{-4}T^{2}-5\cdot10^{-7}T^{3}$	J kg^{-1} °C^{-1}	

Table 5.13. Micro-porous insulation

6. Conclusions

The interior of high temperature steelmaking installations is furnished with coarse grain refractory materials used to withstand the harsh thermal environment and the chemical interaction with the contained atmosphere. Coarse grain refractory materials are sensitive to thermal shock damage due to the distinctive heterogeneous granular structure exhibiting property mismatches at the micro-scale. Thermal shock is induced for example when liquid steel is poured into a cold ladle or when an operating furnace is suddenly opened and the hot refractory lining becomes exposed to ambient air. Catastrophic material failure may occur when the resulting thermal stresses exceed material limits. The possibility to numerically predict this thermo-mechanical degradation process may improve the operational planning for using the thermally loaded structures. To this end a constitutive damage description has been proposed and first validated qualitatively by modelling a dedicated thermal shock experiment. The constitutive description was enhanced in order to describe the degradation phenomena observed in a consecutive series of thermal shock experiments. Inverse modelling of these experiments and the results of quasi-stationary thermal tests enabled the full identification of the governing damage material parameters. The quantified damage framework was coupled to a commercially available thermo-mechanical FE package enabling the analysis of engineering applications. The following conclusions are drawn:

- The degradation of coarse grain refractory materials by (cyclic) thermal shock can be adequately predicted using a (rate-dependent) non-local continuum damage framework dealing with two distinctive mechanisms of damage: elasticity-based damage originating from constrained thermal expansion induced by temperature gradients or boundary effects and thermal damage induced by isotropic thermal expansion (even for a uniform temperature). The contribution of fine scale damage induced by thermal transients, as accounted for by an extended non-locality equation, is considerable.

- Thermal shock damage tests representative for steelmaking processes can be reproducibly applied to coarse grain refractory materials by the repeated surface contact of test samples with molten aluminium followed by a down quench in ambient air. The location-dependent measurement of the transit times of ultrasonic longitudinal waves is a practical and reproducible method to characterize the spatially distributed damage in test samples. Moreover, it appeared from independent thermal shock experiments that the acoustic damage, defined by the relative deterioration of the dynamic Young’s modulus is compatible with the mechanical damage, defined by the relative deterioration of Young’s modulus obtained from mechanical tests.

- It was shown in dedicated quasi-stationary thermal tests that a uniform temperature increase can induce considerable damage in a coarse grain refractory material resulting from CTE mismatches at the micro-scale. The results of these experiments can be used to identify the governing material parameters. When subject to upward thermal shock, the propagation of micro-cracks induced by thermal damage is confined by the already developed elasticity-based damage. Nonetheless, the contribution of the thermal damage to the total thermal shock damage remains significant.

- A mixed numerical-experimental approach involving the inverse modelling of cyclic thermal shock experiments can be used to identify material damage parameters with a sufficient accuracy, applying a first order minimization procedure enriched with numerical damping and optimized for the condition number. Exploiting the analogy between acoustic and mechanical damage, longitudinal wave propagation characteristics can be extracted from the numerical results to enable the comparison with measured results. It is furthermore possible to optimize the present experimental set-up using parameter identifiability analyses up to the level where the inverse problem becomes well-posed.

- The propagation of elasticity-based damage into a coarse grain refractory material subject to a severe up quench thermal shock is fast and governed by thermal expansion at the continuum scale. Temperature gradients influence the damage only further away from the thermal shock front.

- The incremental coupling of the constitutive damage framework with a thermo-mechanical FE code enables the modelling of thermal shock damage in complex high temperature installations subject to cyclic process conditions.

The original contributions and insights revealed in this thesis research can be summarized as follows:

- The non-locality equation to determine the non-local equivalent strain is extended with fine scale damage effects induced by thermal transients; also the identification of the governing model parameter is included.

- The non-local length scale parameter is clearly sensitive to the information contained in the data set of cyclic thermal shock experiments. Its identification from transient experiments has not been reported before.

- Interaction of elasticity-based and thermal damage is revealed by the complementary results of thermal shock and quasi-stationary thermal tests.

- Thermal damage is modelled in a rate-dependent format including a term representing the confinement by elasticity-based damage; the model parameter controlling the confinement has been identified.

- Model parameters were identified by the inverse modelling of a developed experimental set-up to simulate thermal shock at process conditions and involving the location-dependent, non-destructive characterization of damage evolution (which has not been reported before apart from the application of laborious tomographic methods). Based on parameter identifiability analyses improvements to the experimental set-up could be made towards the well-posed identification of the parameters within non-locality, elasticity-based damage and shielding of thermal damage.

- The numerical simulation of thermal shock damage in complex high temperature installations has been performed using a temperature-dependent non-local constitutive damage framework coupled with a thermo-mechanical FE package using an operator-split approach.

Based on the results achieved in the present research the following suggestions for future work can be made:

- The presented constitutive damage framework has been quantified for a refractory material with temperature-independent damage evolution parameters. However, certain classes of refractory material exhibit a distinctive temperature-dependent mechanical behaviour requiring a constitutive description with material damage parameters being a function of the temperature. To successfully identify an associated extended parameter set additional experiments need to be performed. The non-local length scale may be eliminated from this parameter set by determination from mechanical tests involving the size effect. Additional experimental data may be obtained from thermal shock experiments with molten metal heated to a range of temperatures and thermal damage experiments involving the repeated quasi-stationary heating and cooling of test samples. Nonetheless, the independent quantification of all the model parameters is a challenging task possibly mitigated by the use of higher order minimization algorithms and an extension of the presently used acoustic measurement grid.

- The deviation between quantified model and experiments further away from the thermal shock front may be resolved by the incorporation of material degradation processes currently not captured in the model. Thermal conduction for example may be affected by the present micro-cracks induced by thermal shock in a coarse grain refractory material. Higher temperature gradients may thus be induced locally accompanied with a correspondingly higher damage. To incorporate this effect in the present constitutive framework, well known conductivity-porosity relations may be used assuming that damage can be considered as a form of porosity. As a start the degradation of heat transport may be assessed experimentally by measuring the thermal conductivity of test samples previously subject to thermal damage tests.

- In a coarse grain refractory material subject to a non-uniform temperature increase (i.e. thermal shock) the interaction of elasticity-based damage and thermal damage may be of great importance. The observed interdependency of both damage mechanisms may be further investigated with additional experiments. For example, test samples previously subjected to quasi-stationary thermal tests can be subjected to thermal shock experiments and vice versa.

- The description of micro-structural material degradation within the present constitutive damage framework may be enhanced by a coupling with micro-structural models as for example recently developed thermo-mechanical multi-scale descriptions. Models incorporating the heterogeneous micro-structure of refractory materials explicitely may also be used for the identification of the threshold values of elasticity-based and thermal damage.

Samenvatting

Grofkorrelige vuurvaste materialen worden gebruikt in installaties voor de produktie van ijzer en staal waarbij temperaturen tot 1800 °C worden bereikt. Een van de belangrijkste oorzaken van het vroegtijdig falen van dergelijke installaties is de slijtage van het vuurvast door fatale thermische spanningen. Deze worden bijvoorbeeld veroorzaakt door het gieten van vloeibaar staal in een relatief koude pan of door het plotseling openen van een werkende oven waarbij het hete vuurvaste materiaal aan de koude lucht wordt blootgesteld. Thermo-mechanische schade in de vuurvaste voering brengt de levensduur en de beschikbaarheid van de hoge-temperatuur installaties in gevaar wat de kostenefficiënte produktie van staal negatief beïnvloedt. Daarom is het voorspellen van thermoshock schade, hetzij van tevoren in de ontwerpfase van installaties evenals in post-bezwijk analyses belangrijk.

In eerste instantie is thermoshock schade in grofkorrelige vuurvaste materialen aanwezig als een diffuse zone van micro-scheuren en uiteindelijk als macro-scheuren afhankelijk van het aantal en de zwaarte van de thermische belastingscycli. De materiaaldegradatie is overeenkomstig gemodelleerd met een continuüm schade aanpak verrijkt met termen om de micro-schade in rekening te brengen en gevalideerd met data van representatieve thermoshock experimenten. Er is gebruik gemaakt van plaatsafhankelijke akoestische metingen om de schade te karakteriseren. Onbekende model parameters zijn geïdentificeerd door middel van een inverse analyse waarbij het numerieke model is aangepast om de vergelijking met experimenten mogelijk te maken. Een operator-split strategie is toegepast om thermoshock te modelleren in complexe hoge-temperatuur installaties onderhevig aan cyclische procescondities.

Een niet-lokaal schade raamwerk is gekoppeld met warmtetransport en mechanische balans vergelijkingen om de tijdsafhankelijke thermo-mechanische schade en in het bijzonder thermoshock te modelleren in grofkorrelig vuurvast. Niet-uniforme mechanische en uniforme thermische schade zijn gecombineerd in één variabele voor de totale schade. De temperatuursafhankelijke mechanische schade ontstaat ten gevolge van thermische expansie die wordt geïnduceerd door thermische gradiënten en die inwendig wordt beperkt door het materiaal zelf en uitwendig door bijvoorbeeld buurstenen. Thermische schade is het gevolg van temperatuurstijging door verschillen in thermische expansie op micro-schaal. De mechanische schade wordt gestuurd door een niet-lokale equivalente rek. De onderhavige niet-

lokaliteitsvergelijking is uitgebreid met termen om de micro-schade, veroorzaakt door plotselinge temperatuurveranderingen, in rekening te brengen in combinatie met de bijdragen van elastische rekvelden op de continuüm schaal. De invloed van de niet-lokaliteit inclusief de (micro-structurele rekgradiënt) uitbreiding is onderzocht in een parameterstudie. De fenomenologische relevantie van het schade raamwerk is vastgesteld door het modelleren van thermoshock experimenten waarbij chamotte vuurvast monsters in oppervlakte-contact zijn gebracht met gesmolten aluminium gevolgd door afkoelen aan de buitenlucht.

In een literatuur overzicht zijn diverse opstellingen besproken om thermoshock experimenteel te onderzoeken. Met de in dit proefschift voorgestelde testmethode wordt thermoshock in grofkorrelig vuurvast opgewekt met reproduceerbare en realistische warmte transportcondities representatief voor het staalproduktie bedrijf. Een serie thermoshock proeven op corund materiaal en meting van de doorlooptijd van ultrasone longitudinale golven op diverse lokaties op hetzelfde monster gaf een beeld van de ruimtelijke schadeverdeling. De compatibiliteit van akoestische en mechanische schade werd bevestigd in onafhankelijke experimenten, uitgevoerd om de schade karakterisatie methode mechanisch te valideren. Akoestische schade is hier gedefinieerd als de afname van de dynamische elasticiteitsmodulus in relatie tot die in de onbeschadigde toestand. Hiermee in overeenstemming is de mechanische schade gedefinieerd als de afname van de elasticiteitsmodulus verkregen uit mechanische testen in relatie tot die in de onbeschadigde toestand. Uit een vergelijking van de schade gemeten na opeenvolgende thermoshock experimenten en quasi-stationaire thermische testen volgde de interactie tussen mechanische en thermische schade. Bovendien bleek dat de propagatie van micro-scheuren veroorzaakt door thermische schade wordt tegengewerkt door de reeds aanwezige mechanische schade.

Om de schade in vuurvast materiaal, blootgesteld aan meerdere opeenvolgende thermoshock cycli, correct te modelleren is een raamwerk voorgesteld waarbij de schadegroei per tijdseenheid wordt gekoppeld aan de relevant procesgrootheden. Mechanische en thermische schade worden op een zodanige manier gecombineerd dat de experimenteel waargenomen interactie wordt beschreven, met daarin meegenomen termen om de belemmering van thermische schade groei door aanwezige mechanische schade te beschrijven. Het schade raamwerk is geïmplementeerd in een niet-lokaal thermo-mechanisch eindige elementen programma. De waarden van de parameters in de evolutiewet voor ‘onbelemmerde’ thermische schade konden na integratie worden bepaald met de resultaten van de quasi-stationaire thermische experimenten. De waarden van de andere schade materiaalparameters konden worden bepaald door middel van invers modelleren van de cyclische thermoshock experimenten daarbij gebruikmakend van een Gauss-Newton minimalisatie algorithme dat werd verbeterd door numerieke demping en geoptimaliseerd met betrekking tot de parameter identificeerbaarheid. Om de vergelijking met experimenten mogelijk te maken zijn longitudinale golfvoortplantingseigenschappen berekend op basis van de numerieke resultaten daarbij gebruikmakend van de analogie tussen akoestische en mechanische schade. Alle modelparameters konden worden bepaald met een redelijke nauwkeurigheid. Vooral de niet-lokale lengteschaal bleek gevoelig voor de informatie in de dataset verkregen uit de tijdsafhankelijke experimenten. Een redelijke overeenstemming werd verkregen tussen de experimentele en numerieke resultaten van de eerste en de tweede thermoshock cyclus. Om de geoptimaliseerde parameterset te valideren werd een derde thermoshock cyclus gemodelleerd waarbij op zekere afstand van het shockfront enige afwijking met de experimentele resultaten werd geconstateerd. Op deze lokatie benadert de waarde van de doorlooptijden die in de onbeschadigde toestand en het kan zijn dat het model niet nauwkeurig genoeg is om deze verschillen te voorspellen. Op basis van een zogenaamde parameter identificeerbaarheidsanalyse konden verbeteringen aan de meetopstelling worden aangegeven door uitbreiding van het akoestische meetgrid tot op het niveau dat het inverse probleem goed gesteld wordt. Uit resultaten van modellering met de gekwantificeerde parameters bleek verder dat de elastische golf zich nagenoeg instantaan voortplant in het monster. Temperatuursgradiënten beïnvloeden de mechanische schade alleen op zekere afstand van het shock-front. Het is verder gebleken dat thermoshock een gebeurtenis is die zich afspeelt op twee schalen met daarin macroscopische en microscopische bijdragen van dezelfde orde van grootte. De bijdrage van de thermische schade aan de totale schade is aanzienlijk ondanks de afscherming door mechanische schade.

Het gebruik van het ontwikkelde en gekwantificeerde schade raamwerk voor technische toepassingen werd mogelijk door toepassing van een zogenaamde operator-split strategie. Niet-lokale schade-evolutie is incrementeel gekoppeld aan een thermo-mechanisch eindige elementen methode (EEM) pakket dat wordt gebruikt om hoge-temperatuur installaties onderworpen aan cyclische proces condities te bestuderen. De niet-lokaliteit wordt verdisconteerd op incrementeel niveau door middel van ruimtelijke EEM discretisatie en backward-Euler tijdintegratie. De numerieke oplossingsstrategie werd gedemonstreerd door thermoshock schade in de inlaat van een staal ontgassingsinstallatie te bestuderen. Het effekt van een wijziging in de proces-condities is onderzocht. In een tweede rekenvoorbeeld wordt de thermoshock schade in de vuurvast voering van een staalpan onderzocht.

Acknowledgements

First of all I would like thank my promotor Marc Geers and copromotor Marcel Brekelmans for their guidance, patience and many hours of fruitful discussions. The concise reviewing of my work, sometimes even at overtime during the finalization of my PhD thesis, is highly appreciated.

I would also like to express my gratitude to profs. Allix, Perego, De With, Boom and Schmitt for taking place in the defence committee and for their constructive criticism.

This thesis work has been fulfilled within the framework of the Seedcorn programme of Corus Research Development and Technology. I am in particular debt to Rene Duursma and Rob Boom, managers of the Seedcorn programme as well as to Henny Schram and Carel Kleemans, former and present head of the Ceramics Research Centre respectively, for allowing me to perform the doctoral research. The useful discussions I had with Sido Sinnema, my supervisor at Corus, are highly appreciated as well as his 'non-local actions' to safeguard the continuity of the PhD project.

The present doctoral work was part of the Senter BTW (Betere Temperatuur Wisselbestendigheid) project. I would like to express my gratitude to the project partners for the pleasant cooperation and useful discussions during the progress meetings. Special thanks to Marcel Franken and Johannes Boersma for generously providing test refractory material and to Harrie Gorter for his input in conceiving the thermal shock test set-up.

The experimental part of this PhD work could not have been done without the help of several people. I would like to acknowledge the contribution of the internees Jeroen van de Ende, Warbout Tesselaar, Vincent Galante and last but not least Johan van den Eynden who also made a start with the Operator Split programme. Also thanks to Sjaak Metselaar, Jan Bakker, Aad Compier and Marcel Peekel of '3J21' for the concise preparation of test samples and helping out the internees when required. The pleasant co-operation with Kees van der Zwet Slotenmaker and Piet Commadeur and later with Hans Feenstra and Bastiaan de Bruijn during the thermal shock experiments is thankfully remembered.

I also wish to acknowledge the colleagues of the Ceramics Research Centre and in particular my roommates of the numerical modelling group Kirill Andreev, Pieter Put and Paul van Beurden for the pleasant working atmosphere and fruitful discussions in particular on the Ansys models.

I would also like to thank my family and friends for their understanding and patience. The final expression of gratitude is reserved for the most important person in my life. Thank you Petra, without your loving and caring support in difficult times this thesis would be non-existent

Curriculum vitae

1969	Born in Delfzijl, the Netherlands
1989 - 1997	MSc. Mechanical Engineering at the University of Twente
1997 - 2000	Research Drilling Engineer, Shell International exploration and Produktion
2000 - 2002	Design Engineer, IHC Gusto Engineering
2002 - 2004	Researcher, Corus Ceramics Research Centre
2004 - present	Senior Researcher, Corus Ceramics Research Centre
2005 - 2010	Ph.D., Section Mechanics of Materials, Department of Mechanical Engineering, Eindhoven University of Technology, The Netherlands